Towards the Development of Pseudoductile FRP Rebar

By

Marcus Alexander Ivey

A thesis submitted in partial fulfillment of the requirements for the degree of

Master of Science

Department of Mechanical Engineering

University of Alberta

ABSTRACT

Steel has traditionally been used as the material of choice for concrete reinforcement, due in part to its combination of high strength, stiffness, and ductility. However, steel rebar is susceptible to corrosion when exposed to moisture and salts, which can lead to delamination between the steel and concrete, requiring costly repairs to prevent premature failure of reinforced structures. In order to solve this problem, non-corrosive fiber reinforced polymer (FRP) rebar can be used in the place of steel. Apart from being inherently corrosion resistant, FRP rebar has high specific stiffness and strength, and is non-magnetic. The primary limiting factor of conventional FRP rebars is that they are linear elastic to failure, at low ultimate strains. As a result, higher safety factors must be used when designing structures reinforced with these materials, as they are unable to exhibit significant visual warning before ultimate failure. Improving the ductility of FRP rebar could allow for less conservative design practices to be used, resulting in material and cost savings.

In this thesis, FRP rebar was developed to fail in a pseudoductile manner, meaning that ductility is achieved based on the composite architecture, rather than the inherent properties of its constituent fibers and matrix. The development process included rebar design, manufacturing, structural characterization, and mechanical testing. Pseudoductility was achieved by a combination of material and structural hybridization, with the final rebar consisting of a unidirectional carbon fiber core encased in a braided aramid fiber overwrap. The rebar used a thermosetting matrix material, and was manufactured by a dieless braidtrusion method, which combined aspects of pultrusion and braiding into a single continuous process. The rebar was characterized by various methods, including optical microscopy, scanning electron microscopy

(SEM), and differential scanning calorimety (DSC), to determine constituent volume fractions, degree of cure, and rebar geometry, and also to assess manufacturing quality and consistency. Equations were presented that were successful in predicting braid angle and rebar dimensions based on manufacturing parameters.

Tensile testing was conducted, which showed that the rebar design was successful in achieving the desired pseudoductile failure behavior. Analytical models were developed to predict the tensile behavior of the rebar, and were in good agreement with experimental findings. The models allowed the mechanical properties of the rebar to be predicted based on material properties and manufacturing parameters.

An alternative method was presented to extend the pseudoductility of the FRP rebar by introducing discontinuities into the braided overwrap. The discontinuities were used to initiate pullout of the rebar prior to ultimate tensile failure, taking advantage of interfacial sliding between composite layers. Tensile testing was conducted on discontinuous rebar specimens to assess the viability of the proposed failure mechanism, and the design showed promise as a potential method for increased pseudoductility in FRP rebars.

ACKNOWLEDGEMENTS

The completion of this thesis could not have been done without the help and support of many people around me. First, I would like to thank my supervisor Dr. Cagri Ayranci for his guidance and mentorship through my project, as well as for trusting in my abilities and helping to keep me focused throughout my research. I would also like to thank Dr. Jason Carey for all his support and for challenging my ideas, helping me to improve in the process.

I would like to thank Garrett Melenka for all his help in the lab, and for always being there to offer me advice (whether I asked for it or not). He was a huge part of my success as a student, and always up for a joke or to listen to one of my rants. I would like to thank Benjamin Cheung for all his help setting up the braidline, and being there to bounce ideas off, both work-related and otherwise. I would also like to thank Daniel Aldrich for his excellent work developing the OSM code used in this thesis. For everyone else in the lab, I would like to thank them for making the last two years a lot of fun. I had a great time getting to know everyone and I could not have asked for a better group of lab mates and friends.

I would like to thank the staff of the Mechanical Engineering machine shop, most notably Bernie Faulkner for his help with my mechanical testing and numerous technical questions I had during my research. Bernie was always available to offer help, or at the very least a good conversation.

Of course, I would also like to thank my parents Doug and Michelle Ivey, who helped me to become the man I am today. They have always been there to support me with sound guidance and a hot meal, and I truly could not have asked for a better set of parents.

Finally, I would like to thank my beautiful wife, Michelle Gagnon for her continued love and support that helps to get through anything life throws my way. She put up with me when I was busy or stressed, helped me to decompress, and always helped to put things in perspective.

TABLE OF CONTENTS

LIST OF TABLES

LIST OF FIGURES

1 INTRODUCTION

1.1 MOTIVATION

Steel rebar has long been the dominant reinforcing material for concrete structures. It is stiff, strong, and fails in a ductile manner, which allows for large deformations to occur prior to ultimate failure. When a steel reinforced structure is overloaded, depending on the design selected by the engineer, the ductility of steel can help to provide warning before ultimate failure occurs, allowing for preventive or corrective action to be taken [1, 2]. However, corrosion is a major issue in steel-reinforced structures, as steel corrodes readily when exposed to various environmental factors, such as moisture or salts [2, 3]. Corrosion of steel reinforcement can lead to delamination and spalling of the concrete, compromising its structural integrity [4]. This has led to the rapid deterioration of infrastructures across the globe, requiring costly repairs in many types of structures [4, 5]. To remedy this problem, a suitable alternative reinforcing solution is needed that performs equivalently to steel, while eliminating the problems associated with corrosion.

Recently, fiber reinforced polymer (FRP) rebar has gained popularity as an alternative to traditional steel rebar, mainly due to its inherent corrosion resistance. Though FRP materials are non-corrosive and possess numerous other advantages over steel as a reinforcing material for concrete, there are still important limitations that plague the majority of currently available products. Typical FRP rebars behave in a linear elastic manner to failure, and as a result, offer no visual warning signs before ultimate failure of the reinforced structure [2, 4, 6]. The majority of FRP rebar in the market also possesses relatively low stiffness compared to steel, which limits the design possibilities of these materials [5]. There is, therefore, a need for FRP rebar that behaves in a ductile manner while possessing a high elastic modulus.

1.2 THESIS OBJECTIVES

The primary objective of this thesis is to develop a new type of FRP rebar with a high elastic modulus and that fail in a pseudoductile manner. Pseudoductility entails that ductility is achieved by modifying the composite architecture rather than the inherent material properties of its constituents. The work includes rebar design and manufacturing, as well as physical and mechanical characterization. It is also desired to be able to accurately predict the important geometrical features of the rebar using equations based on user-defined manufacturing parameters. The last objective is to understand the tensile failure mechanism of the rebar and develop a model to predict its tensile response.

1.3 THESIS OUTLINE

The thesis is organized into seven chapters and appendices. In Chapter 2 the necessary background information regarding concrete reinforcement, previous work on ductile FRP reinforcement materials, and relevant manufacturing techniques are discussed. The basic rebar design and materials used, including rebar architecture, and material properties are detailed in Chapter 3. In Chapter 4, the manufacturing process used for producing the FRP rebar is presented. Each step of the process is described in detail and the resulting rebar is characterized in terms of macro and microstructural features. Equations are presented to predict certain geometrical features, and analytical predictions are compared to the measured values. In Chapter 5, the tensile properties of the rebar are examined. A model is presented to predict the pseudoductile tensile response, and model predictions are compared to experimental data. The model is reassessed based on the experimental results, and modifications are made to better reflect the real-world behavior of the rebar. An alternative approach to improve the pseudoductility of the rebar using the concept of short-fiber pullout is presented in Chapter 6. The proposed failure mechanism is detailed and preliminary tensile test results are discussed. Finally, in Chapter 7, conclusions from each section are summarized, and recommendations for future study and improvements to the rebar manufacturing, testing, and modeling approach are given. Additional information to support the main body of the thesis can be found in the appendices.

1.4 REFERENCES

[1] Subramanian, N., 2013, "Design of Reinforced Concrete Structures,"Oxford University Press, pp. 142-213, Chap. 5.

[2] ACI Committee Report, "ACI 440.1R-06, Guide for the Design and Construction of Structural Concrete Reinforced with FRP Bars," pp. 1-44.

[3] ACI Educational Bulletin, "E2-00 Reinforcement for Concrete - Materials and Applications," pp. 1-16.

[4] ISIS Canada, 2006, "ISIS Educational Module 3: An Introduction to FRP-Reinforced Concrete" pp.1-34.

[5] ISIS Canada, 2006, "ISIS Educational Module 2: An Introduction to FRP Composites for Construction" pp.1-25.

[6] Bank, L., 2013, "Progressive Failure and Ductility of FRP Composites for Construction: Review," Journal of Composites for Construction, **17**pp. 406-419.

2 BACKGROUND

2.1 TRADITIONAL CONCRETE REINFORCEMENT

Concrete is one of the most commonly used materials in structural engineering due to its low cost, availability, and formability. Plain structural concrete possesses good compressive strength, ranging from 20 to 100 MPa [1], making it highly resistant to crushing. However, its tensile strength is limited to about 10% of its compressive strength [2], and in many cases, is assumed to be negligible. Plain concrete also does not undergo much deformation before ultimate failure, and typically exhibits approximate ultimate strains of 0.0035 mm/mm (0.35%) [3]. Because of these poor tensile properties, reinforcement is often added to concrete structures to resist applied tensile loads, resulting in improved tensile and compressive strength of the structure [2]. Traditionally, the most common type of reinforcement is in the form of steel reinforcing bars, otherwise known as rebar.

Steel has a good combination of mechanical properties for use in concrete reinforcement. It is high strength, has a high elastic modulus, and similar thermal expansion and contraction properties as concrete. It also bonds well with concrete, allowing for effective load transfer, which allows both steel and concrete to act together during loading. Most steel rebar make use of deformations such as ribs on the surface, as shown for example in Figure 2.1 [2], that help improve bonding by mechanical keying. Steel rebar can also be easily cut, bent, and welded to suit a particular application [2].

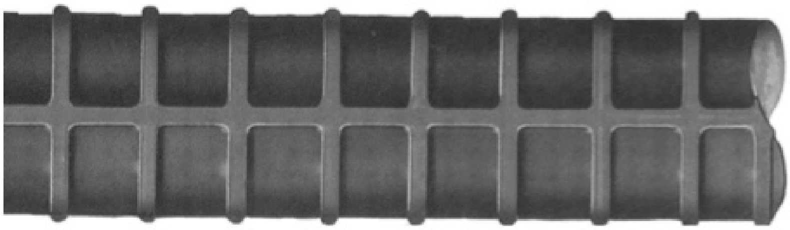

Figure 2.1: Typical ribbed reinforcing bar [2]

When designing concrete beams, reinforcement is usually required. When a beam is subjected to flexure, both tensile and compressive forces develop in the beam and reinforcement is typically used to resist the tensile forces in the beam. There are three main design classifications for steel reinforced structures, which correspond to the expected failure mode depending on the degree of reinforcement used. These are over-reinforced, balanced, and under-reinforced designs; schematic strain distributions for each design as applied to reinforced concrete beams loaded in bending are shown in Figure 2.2. In the over-reinforced case, crushing failure in the concrete will occur before tensile failure of the reinforcement [3]. This is the least desirable of the three failure types, as the concrete failure is brittle in nature, resulting in little to no warning before ultimate failure of the beam. The balanced case is when both the rebar and concrete fail simultaneously [3]. As for the over-reinforced case, this failure type also does not allow for proper warning prior to failure. Finally in the under-reinforced case, failure is initiated by the yielding of the steel rebar [3, 4]. This allows for a ductile failure mode, due to large inelastic deformations in the steel, which provides visual warning signs before ultimate failure. This is the most desirable of the possible failure modes. Because of its low ultimate strain, cracks form in the concrete prior to yielding of the steel, which causes a sudden transfer of loading to the rebar, resulting in increased rebar strain. The beam will experience large deflections, due to large strains in the rebar and wide cracks before ultimate failure, which allow for the opportunity for repairs to be made to the structure or for evacuation protocols to be taken before ultimate failure [3].

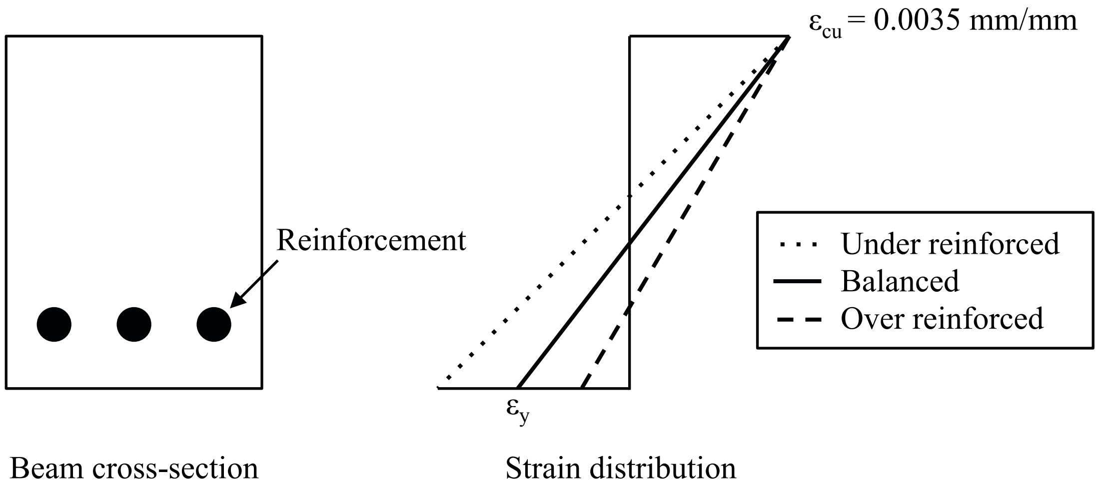

Figure 2.2: Comparison of strain distribution for over-reinforced, balanced, and under-reinforced sections, where ε_{cu} is the ultimate strain of concrete, and ε_y is the yield strain of the steel reinforcement [3, 5]

Corrosion can be a major concern when using steel rebar. In general, steels are susceptible to corrosion when exposed to moisture and air [2]. While the surrounding concrete does provide some degree of corrosion protection to the steel, this is often insufficient, especially in freeze-thaw conditions, wet environments, or when corrosion is chemically promoted. Common causes for corrosion in rebar include the use of deicing salts on roads and bridge decks, and prolonged exposure to seawater [2, 4]. Corrosion in steel reinforcement causes the reinforcement to expand, resulting in delamination or spalling of the surrounding concrete (Figure 2.3), loss of tensile reinforcement, and eventually, premature failure of the structure [5]. Decades of neglect and overuse, combined with these corrosion issues, have led to the extensive deterioration of public infrastructure in countries all around the world [5, 6]. Several different solutions exist to reduce the effects of this corrosion problem. These include stainless steel rebar, galvanizing treatments, chemical and mineral corrosion protection, and epoxy-coated rebar.

Figure 2.3: Corrosion of steel rebar in bridge column resulting in spalling of concrete [5]

In recent years, fiber reinforced polymer (FRP) composites have seen an increase in popularity as an alternative reinforcement material for concrete structures, particularly in applications where corrosion is an issue. FRP reinforcement exists in a wide variety of forms, including rebar, tapes, cables, grids, and sheets [2, 4, 6], and of these different methods, FRP rebar are the most commonly used.

2.2 FRP MATERIALS FOR CONCRETE REINFORCEMENT

FRP materials consist of high strength fibers embedded in a polymeric matrix. Fibers provide high strength and stiffness, while the matrix serves to hold the fibers together, protect the fibers from environmental factors, and transfer applied external loads within the composite material. The development of FRP rebar began in the 1960s, and products were first made available commercially in North America in the late 1970s [4]. Since that time, demand for FRP rebar has steadily increased as more industries begin to recognize the benefits of these materials. FRP rebar is now used in many countries across the globe As of 2012, the American Composites Manufacturing Association (ACMA) reported over 190 installations of FRP rebar in the United States across 15 states, and over 195 installations in Canada [7].

FRP rebar can be made using a variety of different fiber types including glass (GFRP), carbon (CFRP), aramid (AFRP) [4, 6, 8], as well as different matrix materials, including thermoplastics and thermosets [6]. Basalt fiber rebar also exists, and offer comparable performance to GFRP products. The vast majority of commercially available FRP rebar is made from unidirectional glass fibers in an epoxy matrix, and is produced using a process called pultrusion [5, 8]. Properties of FRP rebar can vary significantly, depending on the fiber types used. Table 2.1 shows a summary of typical properties of various types of FRP materials compared to conventional steel rebar.

GFRP rebars are the cheapest of the three major types, and are capable of reasonably high tensile strength in the axial direction. Their coefficient of thermal expansion (CTE) is also most compatible with that of concrete (CTE for concrete between 7.2 $\times 10^{-6}/^{\circ}C$ and 10.8 $\times 10^{-6}/^{\circ}C$) [4]. However, GFRP rebars have a relatively low elastic modulus, and therefore should not be used in stiffness-critical applications [6]. CFRP rebar is the most expensive, but is also the only fiber type that can meet or exceed the elastic modulus of steel, as shown in Table 2.1. AFRP offers intermediate performance, with high strengths and medium elastic modulus values. None of the composites show yielding behavior, and they are all linear elastic to failure with relatively low ultimate strains. Like all fiber composite materials, the final mechanical properties of FRP rebar are dependent on fiber orientation and relative proportions of fiber and matrix [6]. Due to their unidirectional nature, most FRP rebars are anisotropic, and possess relatively poor transverse mechanical properties.

Table 2.1: Comparison of material properties for steel and FRP rebars as provided in [4]

	Steel	GFRP	CFRP	AFRP
Elastic Modulus (GPa)	200	35 – 51	120 – 580	41 – 125
Yield Strength (MPa)	276 – 517	N/A	N/A	N/A
Yield Strain (%)	0.14 – 0.25	N/A	N/A	N/A
Tensile Strength (MPa)	483 – 690	483 – 1600	600 – 3690	1720 – 2540
Failure Strain (%)	6.0 – 12.0	1.2 – 3.1	0.5 – 1.7	1.9 – 4.4
Longitudinal CTE ($x10^{-6}$/°C)	11.7	6.0 – 10.0	-9.0 – 0.0	-6.0 – -2.0
Transverse CTE ($x10^{-6}$/°C)	11.7	21.0 – 23.0	74.0 – 104.0	60.0 – 80.0
Density (g/cm^3)	7.90	1.25 – 2.10	1.50 – 1.60	1.25 – 1.40

FRP rebars have a number of important advantages over conventional steel rebar that make them desirable as a reinforcing material. In general FRP rebar are very light, at less than 1/4 the density of steel [2, 4-6, 9], while still being capable of high tensile strengths in the axial direction [2, 4, 6, 9]. In general, they are also nonmagnetic, nonconductive, and, most importantly, resistant to corrosion [2, 4, 6, 9]. The light weight of FRP rebar helps to reduce transportation costs and improves the ease and speed of installation [2, 9]. Being nonmagnetic and nonconductive, FRP rebar is also ideally suited for use in structures containing highly sensitive electronic equipment, such as MRI facilities [4]. Inherent corrosion resistance means that FRP rebar is a good choice for use in marine structures, bridge decks, and structures exposed to deicing salts [4], or any other application where corrosion is a concern. FRP materials also possess good fatigue resistance and tailorable mechanical properties [4, 6, 9]. Bond performance with concrete is bar dependent, but in general, bonding properties comparable to steel can be achieved, especially when surface deformations are induced to provide mechanical interlock with the concrete [4, 5].

Despite its many advantages, conventional FRP rebar does possess a number of important limitations that must be considered when designing with these materials. Unidirectional FRP composites are linear elastic to failure, with the failure limited by the ultimate strain of the reinforcing fibers. When overloaded, these materials fail in a sudden, catastrophic manner, and do not offer any visual warning signs prior to failure [4, 5, 8]. This is contrary to steel rebar, which undergoes yielding and fails in a ductile manner at high ultimate strains. Other potential disadvantages include possible UV and moisture damage [4] depending on the matrix and fiber types used, as well as low stiffness when compared to steel, especially for GFRP and AFRP composites. Initial material cost is also relatively high, however, over the entire life-cycle of a structure, the cost of using FRP rebar is projected to be equivalent or less than that of traditional steel reinforcement [6, 7, 9]. This is largely because FRP rebar does not corrode, and therefore structures using these materials should require fewer repairs and last longer than their steel-reinforced counterparts.

Because of the lack of ductility, FRP reinforced concrete beams cannot be designed in the same way as those reinforced by steel. Since FRP rebar does not yield, under-reinforcement or balanced design would result in catastrophic failure when overloaded. Instead, FRP-reinforced structures are typically designed for failure by concrete crushing, as this is a slightly more progressive type of failure than brittle failure of the rebar [4, 5, 8]. This is analogous to over-reinforced design in a steel-reinforced structure. This type of design, combined with the brittle failure behavior of FRP rebar, requires higher safety factors to be used for FRP-reinforced structures [4], leading to higher material and construction costs.

Research towards improving the bonding and tensile properties of unidirectional FRP rebar is ongoing. You et al. [10] have explored adding a ribbed surface structure to GFRP rebar via a braiding process in order to improve bond performance by mechanical keying. Their test results showed an increase in bond strength of up to 23% over commercially available GFRP bars, while also exhibiting higher tensile strengths due to high fiber volume fractions and good fiber alignment in their specimens.

Another study conducted by You et al. [11] looked at maximizing tensile strength in their GFRP rebar by manipulating various materials and manufacturing parameters. They found that adding certain fillers to the matrix, and reducing yarn twist helped to improve tensile properties. They also found that pre-tensioning of the unidirectional fibers helped to reduce void content in the composite as well as improve tensile strength.

Another limitation of FRP rebars is that, unlike steel reinforcement, their tensile strengths vary with bar diameter [12]. In general, tensile strength of FRP bars decreases with increasing diameter due to shear lag occurring in the cross-section of the rebar, leading to inefficient load transfer from the outside of the bar to the inside. In an attempt to reduce the effect of inefficient fibers in the center of the rebar cross-section, FRP rebar with hollow cross-sections were studied by You et al. [12]. Rebar was manufactured at a fixed outer diameter and different hollowness ratios. It was found the tensile strength decreased linearly with increasing hollowness ratio, while elastic modulus decreased non-linearly. The rebar design was optimized according to production cost, and it was found that a hollowness ratio of 36% was the most efficient.

The majority of FRP rebars cannot be bent to shape post-production, as they are manufactured with thermosetting resins. Research was conducted by Hoa et al. [13] to remedy this problem by utilizing a thermoplastic matrix for CFRP rebar. Rebar was produced in a batch process using a heated die, and was manufactured with surface deformations in the form of ribs. The thermoplastic matrix allowed the rebar to be heated and bent post-production. Straight rebar showed comparable tensile properties to other unidirectional FRP rebar in literature and in the market, while the bent rebar showed tensile strengths of only 0.37 times the strength of the straight bars.

2.3 DUCTILITY IN FRP REBAR

As previously stated, poor ductility and a linear elastic failure mode are the main limitations facing conventional FRP rebar. Producing FRP rebar that behaves in a more ductile manner would allow for less conservative design of FRP reinforced concrete structures, leading to important savings in materials and cost. Ductility of the fibers themselves is extremely limited, and is not likely to see significant improvements in the near future; therefore alternative methods related to pseudoductility must be considered. Pseudoductility is the ability for a composite material to simulate a ductile failure behavior, and fail in a controlled, progressive manner, despite being made up of linear elastic constituents. This can be achieved by manipulating the composite architecture and constituents to produce a tensile response that resembles yielding following a linear-elastic response.

Bank [8] reviewed the developments in progressive failure and ductility of FRP composites in the context of civil engineering applications, including for FRP rebar. The major methods used to increase rebar ductility include fiber hybridization, incorporation of different manufacturing techniques such as braiding, and exploiting shear failure in the surface layer of the rebar. Methods utilizing progressive failure of the bond between the rebar and concrete have also been considered. Fiber hybridization is the primary approach used for creating pseudoductile composites. A hybrid composite contains two or more components with distinctly different failure strains. These composites can be used to cause progressive failure by causing multiple fractures in the composite. In a multi-component system, multiple fracture occurs when the low-strain component breaks, and there is a sufficient amount of the high-strain component to take the load [14], thus preventing catastrophic failure at the first cracking strain.

Bunsell and Harris [15] studied the hybrid effect in glass-carbon hybrid laminates, and their findings may be useful in guiding the development of hybrid FRP rebar. Two types of hybrids where made, one where alternate layers were bonded together, and the other where layers were unbonded. Samples were tested in tension, and it was found that the unbonded samples exhibited a large load drop at failure of the low-strain carbon plies, followed by linear reloading and final failure at the failure strain of the high elongation glass plies, resulting in a bilinear load-strain curve, as shown in Figure 2.4. For the bonded case, a series of small load drops and reloading was observed, beginning around the ultimate strain of the carbon plies, and continuing until a strain below the ultimate strain of the glass plies. This created a sort of “saw-tooth” pattern in the plot, as shown in Figure 2.5. By achieving good interlayer bonding, the carbon plies continued to share some of the load, even after initial failure, leading to a progressive failure type.

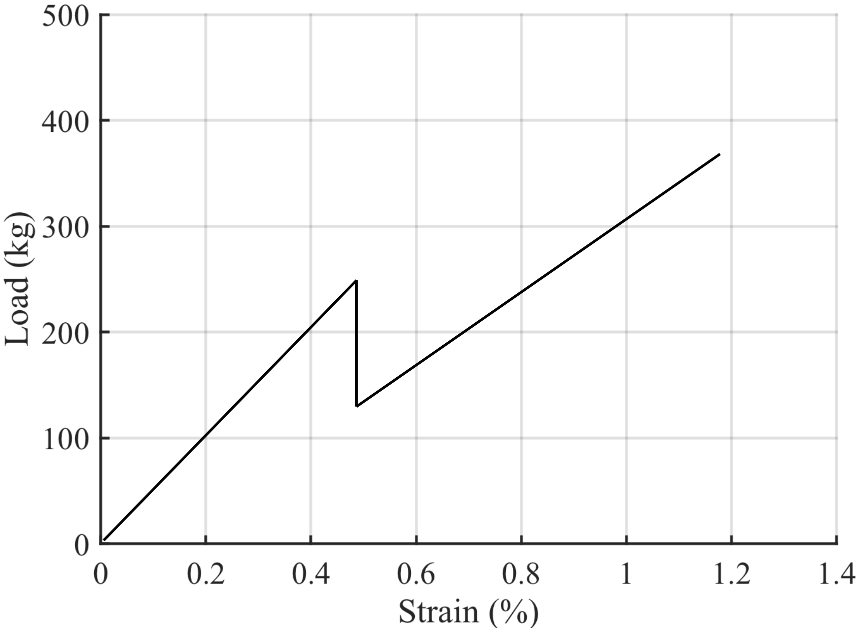

Figure 2.4: Load vs strain plot of unbonded hybrid laminate (adapted from [15])

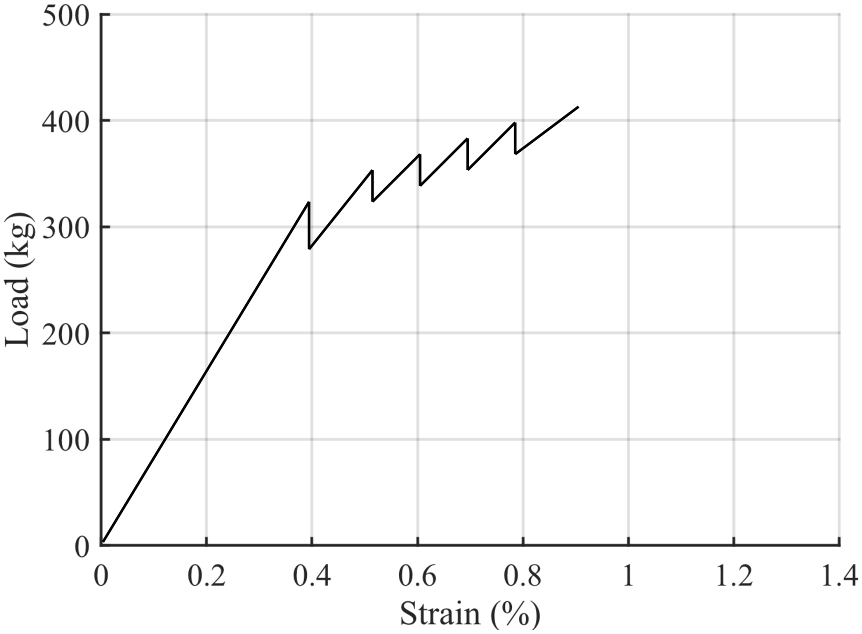

Figure 2.5: Load vs strain plot of bonded hybrid laminate (adapted from [15])

Bakis et al. [16] attempted to utilize material hybridization to create pseudoductile FRP rebar equipped with strain monitoring capabilities. Hybrid bars consisting of various combinations of carbon, glass, aramid, and polymer fibers were manufactured by pultrusion. Different fiber arrangements were produced, with varying distribution and dispersion of fiber types throughout the cross-sections in order to compare mechanical properties and strain sensing capabilities. Specimens showed the characteristic hybrid composite failure behavior consisting of linear elastic loading and abrupt load drops and reloading corresponding to the different fiber failure strains. The tensile behavior varied depending on the fiber arrangement used. The resistance in the carbon fibers was monitored in an attempt to monitor strain in the rebar, and showed changes in resistance upon initial failure of the low elongation fibers. The tensile response for bars consisting of a carbon fiber core concentrated surrounded by glass fibers was similar to that of hybrid laminates.

Somboonsong, Harris, and Ko [17, 18] developed a design methodology for the production of pseudoductile FRP rebar using a combination of material and structural hybridization. The design consisted of a unidirectional carbon fiber core wrapped in braided aramid fiber yarns. The carbon fiber core was intended to provide high stiffness, while the braid was there to achieve large elongations before failure. During the braiding process, ribs were introduced into the surface of the rebar to aid in bonding with concrete. The properties of the braided yarns were determined based on a structural hierarchy taking into account fiber drawing, yarn twist, yarn crimp, and braid angle, and a model was developed to predict the stress-strain behavior of the rebar. The model predicted a bilinear failure, similar to other hybrid composites, but with high failure strains due to the structure of the braid yarns. Tensile test results exhibited a saw-tooth type failure after initial breaking of the low elongation core fibers, as shown for example in Figure 2.6. The model predicted the initial elastic modulus well, but over predicted the ultimate failure strain in some cases. Failure strains were limited by the maximum strain of the braid yarns, resulting in observed ultimate strains up to 2.5%.

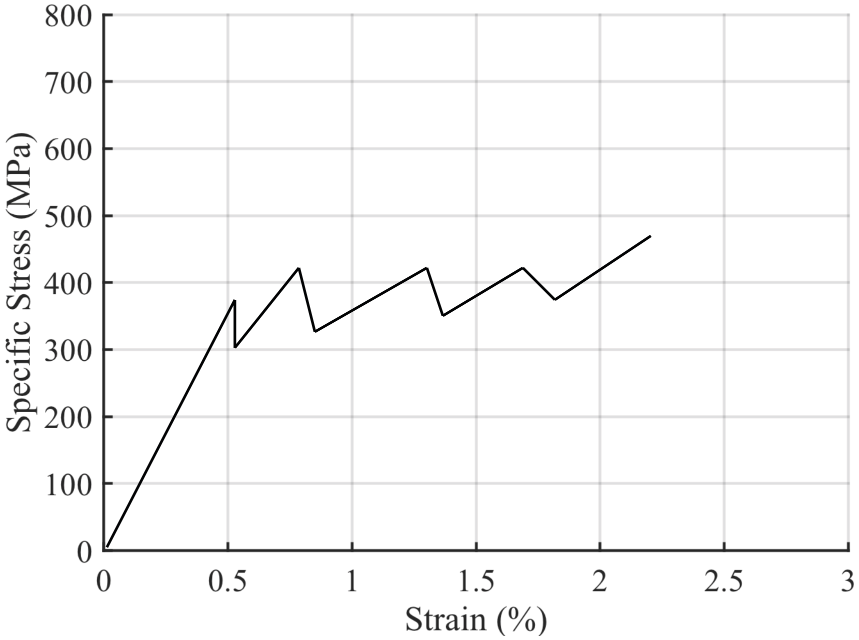

Figure 2.6: Stress-strain characteristics of hybrid FRP bars (adapted from [18])

A similar design methodology was used by Pastore et al. [19] to produce pseudoductile hybrid FRP rebar that consisted of a unidirectional carbon fiber core and ribbed braid structure made from aramid yarns. Tensile test results showed the same overall behavior as previous work by Somboonsong et al., resulting in failure strains between 2 and 3% and a saw-tooth type failure. A new modeling approach was implemented by Pastore considering the fibers as rods arranged in different orientations. The model did a good job of predicting the initial elastic modulus and initial failure point, but failed to capture the behavior past this point.

Hampton [20, 21] also based his work on a similar hybrid design incorporating a unidirectional carbon fiber core wrapped in braided aramid yarns. Different variations of fiber types and proportions of carbon and aramid were examined, as well as different types of surface deformations. Microscopy was used qualitatively as a quality control measure. In order to help tailor mechanical properties of the bars, a model was developed to predict geometric and mechanical properties of the rebar based on braid angle and fiber volume fractions. The model did a reasonably good job at predicting the stress-strain response, as shown in Figure 2.7. However, the model over-predicted the initial stress drop, and failed to capture the saw-tooth behavior after the initial failure point. The model also significantly over-predicted the ultimate strains in the rebar. The saw-tooth behavior was attributed to uneven tensioning of the unidirectional carbon yarns in the core caused by errors in manufacturing. The author expressed a need for a better understanding of the failure mechanism after the initial failure point, in order to improve analytical predictions.

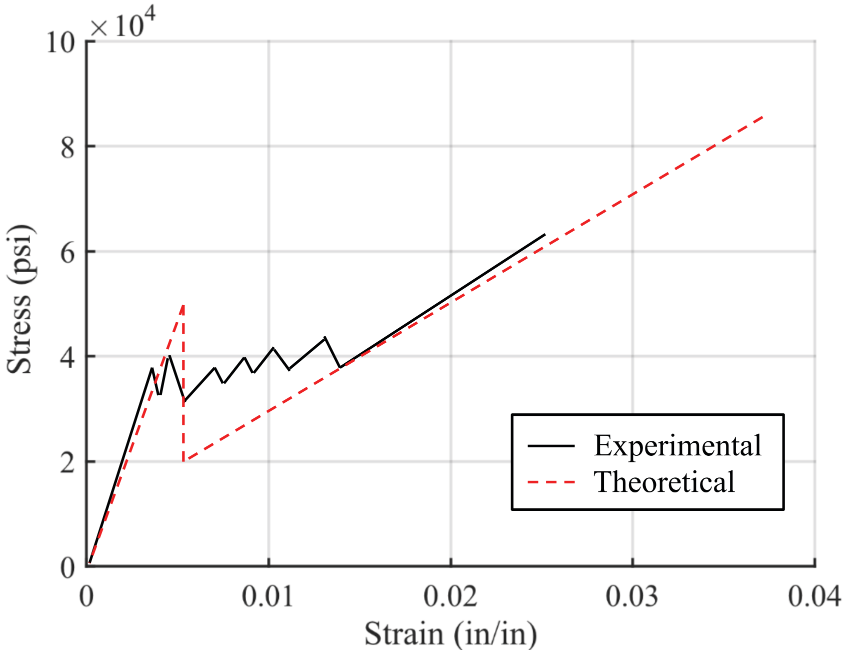

Figure 2.7: Comparison between model and experimental stress-strain results (adapted from [20])

Ewen [22] moved away from the hybrid composite approach, and instead considered using the principles of short fiber pullout to achieve pseudoductility. A design concept was developed consisting of a unidirectional carbon fiber bar wrapped in a discontinuous, thin braided aramid layer. The braid was cut at regular intervals, creating discontinuities intended to lead to pullout between the core and braid. The braided layer was not used for its mechanical properties, but instead provided an interface against which the carbon core could slide. It was theorized that as the rebar is loaded in tension, the core would debond from the braid and pull out, resulting in a controlled failure of the reinforced structure. This mechanism would allow for ductility of the overall reinforced structure, but not in the rebar itself. The results showed some promise, but the pullout behavior was unstable and exhibited large load drops during debonding. It was suggested that better control of the core-braid interface might help improve performance. A second design concept for rebar consisting of short rods embedded in an epoxy matrix was also developed. The design concept looked to take advantage of short fiber pullout theory to obtain large elongations of the rebar. Initial experiments used steel rods in an epoxy matrix and showed positive results as a proof of concept, but manufacturing of a single rebar specimen was labor intensive and not practical at scale. Due to the use of short rods in this method, the potential rebar stiffness and strength is relatively low, compared to a continuous composite material.

More recently, Czel et al. [23] looked at the effect of ply thickness in a hybrid composite laminate in an attempt to eliminate the load drop commonly observed at failure of the low elongation fibers. A laminate consisting of a thin carbon ply sandwiched between two glass plies was considered, and an approach based on strain energy was taken to determine the layer thickness required for stable pullout. In most hybrid composites, initial failure of the low strain component leads to delamination of the layers, which causes a drop in stress. By decreasing the thickness of the low elongation layer, multiple fractures occurred in this layer, leading to stable pullout rather than complete delamination. This resulted in the stress-strain behavior shown schematically in Figure 2.8. However, the reduction in carbon ply thickness significantly decreased the elastic modulus of the composite; furthermore, ultimate failure strains were still limited by the failure strain of the glass plies. A later study by the same group [24] used a discontinuous central carbon layer that was cut prior to loading to induce multiple crack initiations. This resulted in stable pullout, while allowing for a thicker central layer to be used, and thus increasing the elastic modulus of the composite. Though these studies dealt with laminated composites, these concepts may also be applicable to improving pseudoductility in FRP rebar.

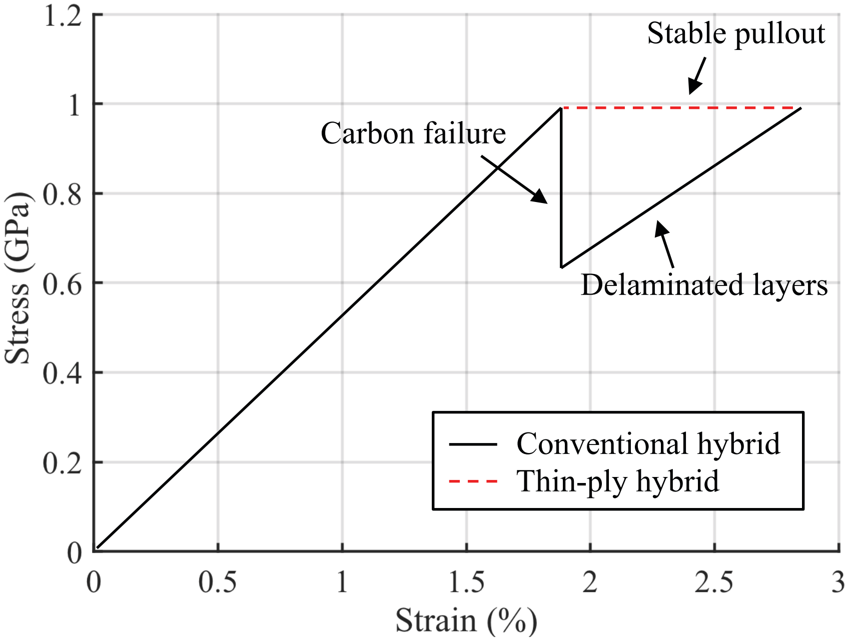

Figure 2.8: Schematic of stress-strain plot of a conventional and thin-ply hybrid composite laminate (adapted from [23])

2.4 MANUFACTURING BY BRAIDTRUSION PROCESS

Much of the research regarding pseudoductile FRP rebar has utilized a braidtrusion manufacturing process. Braidtrusion is a combination of two conventional composites manufacturing techniques, namely braiding and pultrusion. The combination of these methods facilitates the production of certain composite structures that would otherwise be difficult to manufacture by conventional methods. Braidtrusion is also known under different names such as “braiding pultrusion” [25] or “pullbraiding” [26]. It is a relatively new process first developed in the late 1990s and has since been used and modified by various researchers, as it continues to mature.

2.4.1 Pultrusion

Pultrusion is a composite manufacturing process that allows for rapid production of constant cross-section parts in a continuous fashion [27]. It is analogous to an extrusion process for metals and polymers, except that instead of pushing material through a die, the material is pulled. This process is widely used in industry, and is the primary method of manufacturing unidirectional FRP rebar. The pultrusion process was originally conceived following the Second World War, at the same time as many modern composites manufacturing techniques were developed [27].

A schematic representation of a typical pultrusion process using a thermoset matrix is shown in Figure 2.9. Spools of yarns made up of the desired reinforcing fiber are loaded onto a creel, from which they are pulled through a series of guides. The yarns then pass through a resin bath, where the fibers are impregnated by low viscosity, thermosetting resin. It is important that the resin viscosity is low and the pot life (time for initial mixed resin viscosity to double, or more if the initial viscosity is very low) is long, in order to facilitate complete fiber wetting [27, 28]. After leaving the resin bath, the impregnated tows are consolidated into a bundle and pass through a heated die where it is cured. Inside the die, pressure is applied, forcing the resin to flow through and completely wet the fibers [27, 28]. The cross-section of the die determines the final cross-sectional shape of the composite. A caterpillar-type puller consisting of synchronous belts on either side of the cross-section is typically used to advance the composite through the process. The cured composite can then be cut to the desired length at the end of the line.

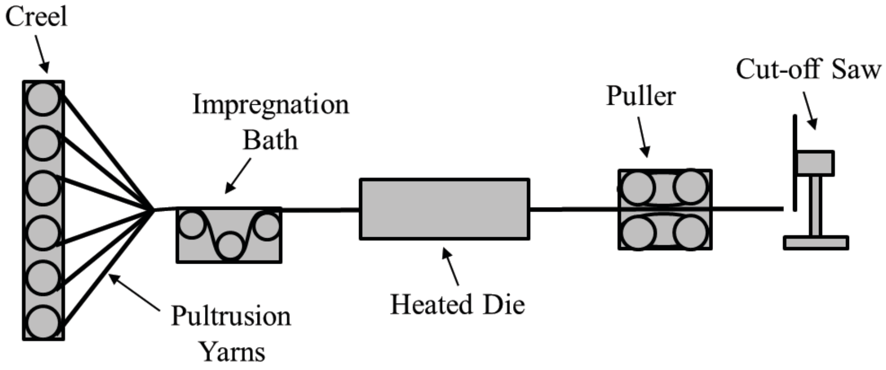

Figure 2.9: Schematic of pultrusion process

Pultrusion is a fully continuous process, and allows for very high production rates by composite standards, on the order of several meters per minute [27, 28]. This allows for composite parts to be produced at relatively low costs when compared to other composite manufacturing techniques [27, 28]. The process also allows for near-net shape production of components with a low scrap rate of less than 5% [27], and can produce composites with high fiber volume fractions, using all types of reinforcing fibers [27, 28].

The pultrusion process is only capable of producing constant cross-section parts [27, 28], such as rods, angles, I-beams, tubes, among others. It is best suited to produce unidirectional composites, where the fibers are aligned along the pulling axis. However, it is possible to add angled fibers to the composite structure by pulling prepreg mats of off-axis oriented fibers through the process instead of simply unidirectional yarns [27]. This can help to improve the off-axis properties of the composite.

2.4.2 Braiding

Two-dimensional braiding is a textile process where multiple yarns are intertwined to form an interlocking pattern. A typical braiding machine consists of fiber carriers moving around a circle in a serpentine path [29], as shown schematically in Figure 2.10. This type of braiding machine is referred to as a Maypole braider. In this process, half the carriers move in the clockwise direction, while the other half move counter clockwise, to produce the intertwined structure of yarns. There are three main structures of braids that can be produced, as shown schematically in Figure 2.11. These are referred to as diamond braids, regular braids, and Hercules braids, and they differ simply by the number of yarns that pass over and under each other [29, 30]. A diamond braid has one yarn passing over and under other yarns, a regular braid has two yarns passing over and under, and a Hercules braid has three yarns passing over and under.

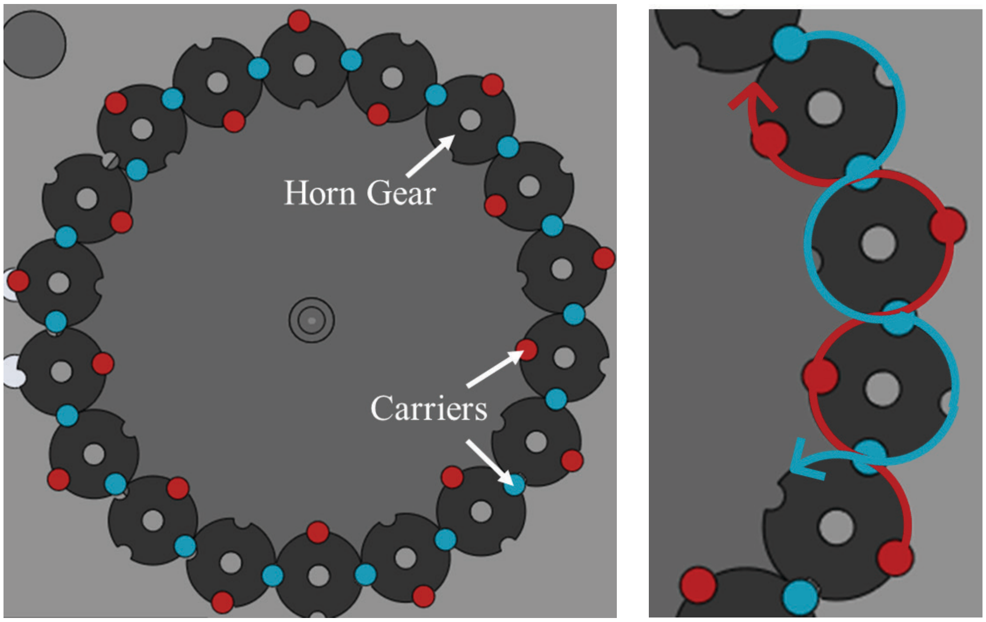

(a) (b)

Figure 2.10: Schematic of (a) carrier configuration for a regular braid, and (b) serpentine motion of the carriers, with clockwise motion shown in blue and counterclockwise motion shown in red

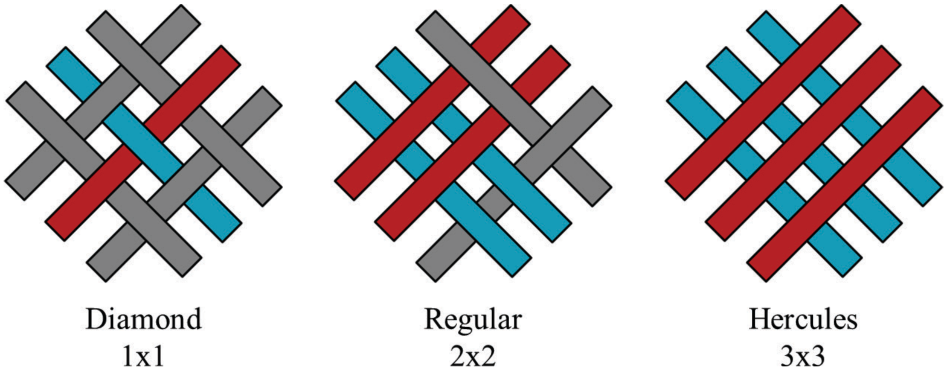

Figure 2.11: Diamond, regular, and Hercules braid architectures

A typical horizontal 2D braiding process is shown schematically in Figure 2.12. The orientation of the braiding yarns can be described by the braid angle, which is the angle between the longitudinal direction of the braided preform, and the deposited fiber [29-31], as shown in Figure 2.13. During the braiding process, the yarns are typically braided around a mandrel, which gives the braided preform its shape. Mandrels range from a simple uniform cross-section, to complex shapes, and can be either rigid or flexible. The mandrel is pulled forward while the braid is formed around it, and the relation of the rotational speed of the braid machine and the pulling speed, impacts the resulting braid angle that is produced [30]. As the braid yarns form around the mandrel, they are usually guided by a forming ring [30, 31], which helps set the convergence point of the braid yarns and ensure consistency of the braid structure. A typical braid produced using only braiding yarns is referred to as a biaxial braid. Triaxial braids can also be produced [29-31], where longitudinal yarns are inserted into the structure to improve axial properties to the composite.

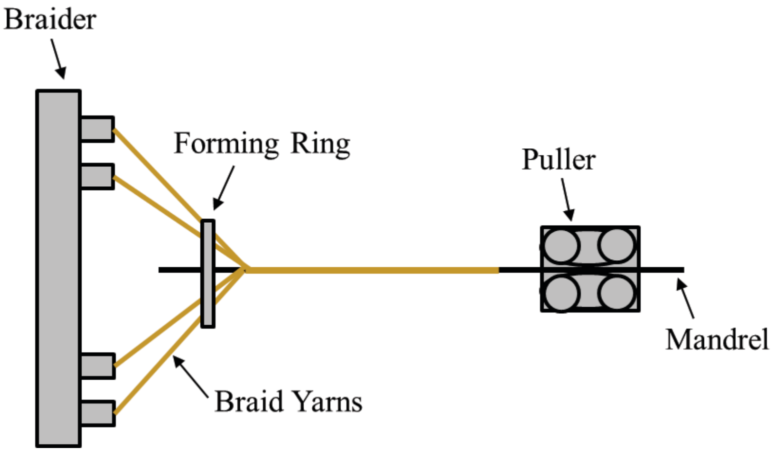

Figure 2.12: Schematic of braiding process

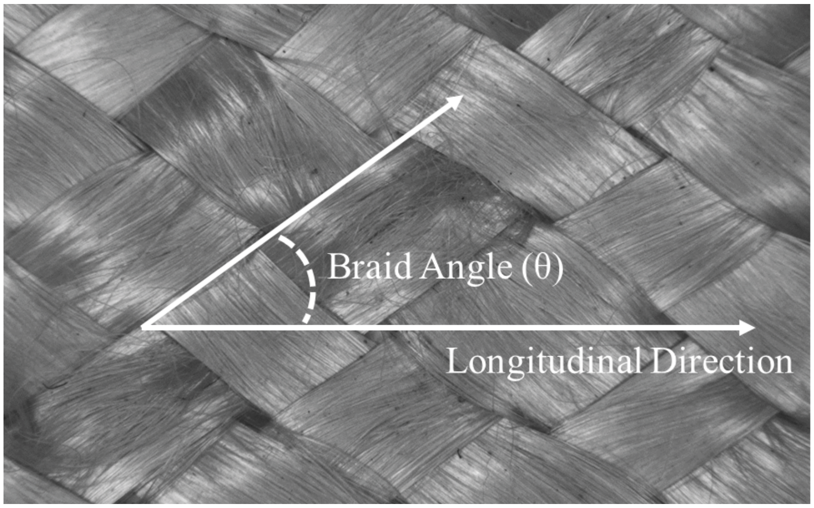

Figure 2.13: Definition of braid angle

Braiding allows for a high rate of strand deposition, and relatively low cost of production [29], as well as the production of near-net shape composites with a wide variety of cross-sections [31]. The main disadvantage of braiding is that it is difficult to produce preforms with very low braid angles, due in part to physical jamming of the braid yarns [29].

Due to the off axis orientation of the braid yarns, braided composites are often used in cases where high shear stiffness is desired, or when transverse elastic properties, damage tolerance and toughness are important [29]. They have been used in such applications as structural columns, rods, shafts, pressure vessels, and plates, as well as aircraft components, sporting equipment, and more [29].

2.4.3 Braidtrusion

As its name suggests, braidtrusion is a combination of braiding and pultrusion into a single manufacturing process. At its most basic, the braidtrusion process combines these methods by simply adding a circular braiding machine to a standard pultrusion line, prior to curing. This process was first developed at Drexel University by Ko and Pastore [32] for the production of hybrid composite bars. A general process schematic is shown in Figure 2.14; however, this process may vary depending on the impregnation and curing methods used. Impregnation methods can include a resin bath, impregnation ring, or resin infusion, and curing can be done by heated die, convective oven, induction, or a combination of these methods. When thermoplastic matrix materials are used, impregnation can be done by the inclusion of commingled yarns [33].

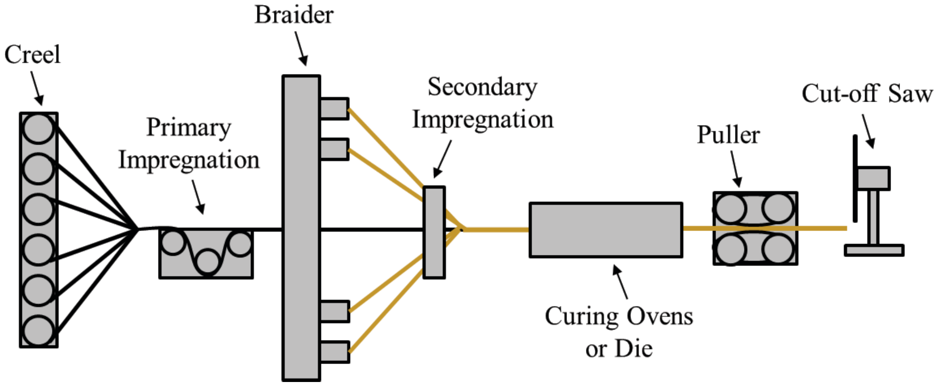

Figure 2.14: Schematic of the general braidtrusion process

The primary use for the braidtrusion process in literature has been in the production of hybrid composite rebar for concrete reinforcement. A number of researchers have explored the use of braidtrusion for this purpose, each with their own modifications to the basic manufacturing process. The production of pseudoductile rebar developed by Somboonsong, Ko, and Harris [17, 18] was one of the first applications of the braidtrusion process. The process allowed for the production of a unique hybrid composite structure consisting of a unidirectional core and braided overwrap. This structure was made possible by the braidtrusion process, and could not easily be produced by other composite manufacturing techniques. Impregnation was achieved by pouring resin onto the fibers prior to the braiding point, and curing was conducted by a combination of heated die and post-cure oven.

In his work on pseudoductile FRP rebar, Hampton [20, 21] also used a braidtrusion process. The original process was modified by introducing the concept of dieless curing. In this method, the impregnated rebar was allowed to cure under tension at room temperature for 24 hours, and then placed in a post-cure oven to attain maximum strength. To do this, the braidtrusion process had to be paused while the rebar cured, eliminating the ability for continuous production. By curing without a die, the natural shape produced by the braid was fully preserved, resulting in an improvement in the ribbed surface deformations. SEM analysis of the bars showed that the microstructural quality of rebar produced by this dieless curing method was comparable to those produced using a die. Pastore [19] used a similar braidtrusion process to produce pseudoductile FRP rebar as well, however rather than curing the rebar at room temperature, an in line oven was used to cure the composite in a continuous process.

Ewen [22] and Poisson et al. [34, 35] used the braidtrusion process to create rebar with a large diameter pultruded carbon fiber core, and a thin braided layer overtop. In this case, the braided layer was used to form the carbon core into a round shape without the use of a die. Impregnation in these studies was conducted using an impregnation ring prior to the braiding step; no secondary impregnation step was used. The work by Poisson focused on the control and automation of the braidtrusion line, which is needed in order to transition the process from the lab to an industrial scale.

Sandness et al. [36, 37] introduced a new method of curing using a combination of induction heating and in-line ovens. This method was further refined by Hajihosseini et al. [38, 39]. In this method, small metallic wires were proposed to be embedded longitudinally into the composite structure during the pultrusion step. After braiding and impregnation, the composite passes through an induction coil, which heats the wires, curing the composite from the inside. The composite then passes through in-line ovens for final curing. In theory, this process allows for rapid, uniform curing of large diameter bars, however, it has not been extensively tested and will require further refinement before being widely adopted.

The braidtrusion process has also been adopted to create surface deformations in more conventional linear elastic FRP rebar as well. Fangueiro et al. [40] added ribs to the surface of their GFRP rebar by using thicker braid yarns in select carriers. The focus of this work was on the bonding properties between the rebar and concrete and the subsequent properties of a reinforced concrete beam in bending. You et al. [10, 11] also studied the tensile and bonding characteristics of linear elastic FRP rebar made with glass fibers. The braidtrusion process was used to add a ribbed feature to the surface of the rebar, which improved bonding properties between the rebar and concrete. In this study, only a single impregnation step was used in the form of a resin bath prior to braiding, and curing was done using an in-line oven.

In addition to specific rebar applications, composites produced by braidtrusion have been examined for their energy absorption potential. Hamada et al. [25] conducted crushing tests on rods manufactured by braidtrusion, and found that the braidtruded rods performed favorably compared to unidirectional composite rods. In their process, rods were manufactured with a variety of braid angles and different amounts of pultruded fibers in order to vary the mechanical properties. The unidirectional pultruded fibers served to support the longitudinal compressive load during crushing, and the braided fibers helped to prevent crack formation and propagation in the unidirectional fiber bundles by applying radial compressive stresses on the core.

Ahmadi et al. [41] compared various mechanical properties of braidtruded rods to unidirectional composite rods. Glass fibers were used for unidirectional and braid yarns. They found that the braid helped to prevent axial splitting of the rods during crushing, and that torsional properties were also enhanced by the presence of the braid. The braidtruded rods showed improved shear modulus, elastic modulus and flexural rigidity over their unidirectional counterparts, with a braid angle of 45 degrees providing the best performance in shear.

A number of researchers [26, 42] have been successful in using thermoplastic matrix materials in a braidtrusion process, rather than the conventional thermosets. Michaeli et al. [33] conducted early work for the continuous production of braided thermoplastic composites. In this work, core yarns were not used, however the rest of the system resembled a braidtrusion process. The use of a thermoplastic matrix was favored for its ability to be re-formed or joined post-production, and commingled yarns were used in order to introduce the matrix material into the composite. In order to process the thermoplastic matrix, an additional preheating step was required, followed by a heated die to melt the matrix and force it through the yarns and fully wet the fibers. Finally a cooling step was needed to solidify the completed composite into its final shape. A similar method was applied by Lebel et al. [42], who used a braidtrusion process to successfully manufacture triaxial L-shaped thermoplastic composite beams in a continuous manner with production rates up to 105 mm/min. Carbon fiber yarns, with commingled thermoplastic fibers were used for the pultrusion and braiding yarns, and a heated die was used to form the preforms into the desired L-shaped cross-section. Milwich [26] modified the conventional braidtrusion process to produce curved profiles without the need for any post-forming operations.

The primary advantage of the braidtrusion process is that it allows for the automated production of composite parts with longitudinal and off-axis oriented fibers, producing a structure that has favorable mechanical properties under a variety of loading conditions. Like pultrusion, it also allows for continuous production, at relatively high production rates, and produces near-net shape parts. Because it is versatile in allowing for different fiber types to be incorporated into the composite structure over a variety of orientation angles, this process is conducive to tailoring composite properties. Since it has been primarily used in research applications, the production costs associated with the braidtrusion process have not been well established. However, it is reasonable to infer that costs would be relatively low (in line with pultruded parts), as the process does not require any special fiber or matrix materials, and is capable of rapid production rates.

The main limitations of the process change depending on the type of curing process used, but generally revolve around the cross-sectional geometry that can be achieved. If a heated die is used for curing, then only parts with a uniform cross-section may be produced. Alternatively, if a dieless approach is used, the surface of the part will maintain the natural shape of the braid, allowing for ribs or undulations to be present on the surface. The dieless approach, however, means that parts are limited to take on the cylindrical shape naturally produced by the braid, whereas a die allows for a wide variety of different cross-sectional shapes to be created. Dieless braidtrusion may also lead to slower production rates, and may even require batch production if curing ovens are omitted entirely.

2.5 CONCLUSION

In this chapter, traditional methods of concrete reinforcement using steel rebar were discussed and corrosion was highlighted as the main limitation of steel as a reinforcing material. Non-corrosive FRP rebar was identified as a solution to the corrosion problem, however these products were typically found to be linear elastic to failure with poor ductility. Past research on how to create pseudoductile FRP composites by material and structural hybridization was presented. Finally, manufacturing methods that have been used for the production of FRP rebar were outlined.

In the literature, pseudoductility has been achieved in hybrid FRP rebar, though ultimate failure strains were typically low (<3%), and were limited by the ultimate strain of the constituent fibers. Attempts to model the tensile response of these rebar often failed to accurately capture the rebar behavior after yielding, and over-predicted ultimate strain of the rebar. Utilizing a pullout mechanism between composite layers in FRP rebar has also been attempted as a means to obtain pseudoductility, but showed poor repeatability due to a lack of control of interfacial properties.

The main goal of this research is to develop FRP rebar that performs in a pseudoductile manner while maintaining a high initial elastic modulus. This includes design of the rebar to incorporate a suitable pseudoductile failure mechanism and the development of a suitable manufacturing process that allows for rapid, continuous production of the rebar. In order to understand the failure mechanism of the rebar and assess its pseudoductile characteristics, the resulting rebar will be characterized in terms of structural and mechanical properties, and an analytical model will be developed to predict the tensile response of the rebar.

2.6 REFERENCES

[1] Subramanian, N., 2013, "Design of Reinforced Concrete Structures,"Oxford University Press, pp. 1-44, Chap. 1.

[2] ACI Educational Bulletin, "E2-00 Reinforcement for Concrete - Materials and Applications," pp. 1-16.

[3] Subramanian, N., 2013, "Design of Reinforced Concrete Structures,"Oxford University Press, pp. 142-213, Chap. 5.

[4] ACI Committee Report, "ACI 440.1R-06, Guide for the Design and Construction of Structural Concrete Reinforced with FRP Bars," pp. 1-44.

[5] ISIS Canada, 2006, "ISIS Educational Module 3: An Introduction to FRP-Reinforced Concrete" pp.1-34.

[6] ISIS Canada, 2006, "ISIS Educational Module 2: An Introduction to FRP Composites for Construction" pp.1-25.

[7] Busel, J. P., 2012, "Fiber Reinforced Polymer (FRP) Composite Rebar," American Composites Manufacturers Association (ACMA).

[8] Bank, L., 2013, "Progressive Failure and Ductility of FRP Composites for Construction: Review," Journal of Composites for Construction, **17**pp. 406-419.

[9] Potyrala, P. B., 2011, "Use of Fibre Reinforced Polymer Composites in Bridge Construction. State of the Art in Hybrid and all-Composite Structures".

[10] You, Y., Park, Y., Park, J., 2007, "Development of FRP rebar for concrete structures in Korea," FRPRCS-8, pp.1-8.

[11] You, Y., Kim, J., Kim, S., 2015, "Methods to Enhance the Guaranteed Tensile Strength of GFRP Rebar to 900 MPa with General Fiber Volume Fraction," Construction and Building Materials, **75**pp. 54-62.

[12] You, Y., Park, K., Seo, D., 2015, "Tensile Strength of GFRP Reinforcing Bars with Hollow Section," Advances in Materials Science and Engineering, pp. 1-8.

[13] El-Tahan, M., Galal, K., and Hoa, V. S., 2013, "New Thermoplastic CFRP Bendable Rebars for Reinforcing Strutural Concrete Elements," Composites: Part B, **45**pp. 1207-1215.

[14] Aveston, J., and Kelly, A., 1980, "Tensile First Cracking Strain and Strength of Hybrid Composites and Laminates," Physical Sciences, **294**(1411) pp. 519-534.

[15] Bunsell, A. R., and Harris, B., 1974, "Hybrid Carbon and Glass Fibre Composites," Composites, pp. 157-164.

[16] Bakis, C. E., Nanni, A., Terosky, J. A., 2001, "Self-Monitoring, Pseudo-Ductile, Hybrid FRP Reinforcement Rods for Concrete Applications," Composites Science and Technology, **61**pp. 815-823.

[17] Somboonsong, W., Ko, F. K., and Harris, H. G., 1998, "Ductile Hybrid Fiber Reinforced Plastic Reinforcing Bar for Composite Structures: Design Methodology," ACI Materials Journal, **95**(6) pp. 655-666.

[18] Harris, H. G., Somboonsong, W., and Ko, F. K., 1998, "New Ductile Hybrid FRP Reinforcing Bar for Concrete Structures," Journal of Composites for Construction, **2**pp. 28-37.

[19] Pastore, C., Armstrong-Carroll, E., and Ko, F., 2012, "Effect of Yarn Size on the Performance of Hybrid Braided Composite Rebar," The Masterbuilder, pp. 234-244.

[20] Hampton, F., 2004, "Cyclic Behavior, Development, and Characteristics of a Ductile Hybrid Fiber Reinforced Polymer (DHFRP) for Reinforced Concrete Members," Drexel University. United States.

[21] Hampton, F. P., Ko, F. K., Doyle, C., 2009, "Development of ductile-hybrid composites (DHC) by the braidtrusion process," 17th International Conference on Composite Materials, Anonymous Edinburgh, UK.

[22] Ewen, K., 2005, "Ductility in FRP Rods for Concrete Reinforcement by Interfacial Shearing," University of Ottawa. Canada.

[23] Czel, G., and Wisnom, M., 2013, "Demonstration of Pseudo-Ductility in High Performance Glass/Epoxy Composites by Hybridisation with Thin-Ply Carbon Prepreg," Composites: Part A, **52**pp. 23-30.

[24] Czel, G., Jalalvand, M., and Wisnam, M. R., 2015, "Demonstration of Pseudo-Ductility in Unidirectional Hybrid Composites made of Discontinuous Carbon/Epoxy and Continuous Glass/Epoxy Plies," Composites: Part A, **72**pp. 75-84.

[25] Hamada, H., Kameo, K., Sakaguchi, M., 2000, "Energy-Absorption Properties of Braided Composite Rods," Composites Science and Technology, **60**pp. 723-729.

[26] Milwich, M., 2009, "Thermoplastic braid pultrusion," Proceedings of ICCM 17, Anonymous Edinburgh, UK.

[27] Strong, B.A., 2008, "Fundamentals of Composites Manufacturing - Materials, Methods, and Applications (2nd Edition),"Society of Manufacturing Engineers (SME), pp. 453-461, Chap. 18.

[28] Hoa, S.V., 2009, "Principles of the Manufacturing of Composite Materials,"DEStech Publications, pp. 233-245, Chap. 6.

[29] Ayranci, C., and Carey, J., 2008, "2D Braided Composites: A Review for Stiffness Critical Applications," Composite Structures, **85**pp. 43-58.

[30] Ko, F., Head, A., and Pastore, C., 1989, "Handbook of Industrial Braiding," Atkins and Pearce, Covington, Kentucky.

[31] Ko, F.K., 2001, "ASM Handbook, Volume 21: Composites,"ASM International, pp. 70-77, Chap. Braiding.

[32] Pastore, C.M., and Ko, F.K., 1999, "Braided Hybrid Composites for Bridge Repair," National Textile Annual Report, F98-P01.

[33] Michaeli, W., and Jurss, D., 1996, "Thermoplastic Pull-Braiding: Pultrusion of Profiles with Braided Fibre Lay-Up and Thermoplastic Matrix System (PP)," Composites: Part A, **27A**pp. 3-7.

[34] Poisson, E., Fahim, A., and Munro, M., 2008, "Automated pilot plant production of continuous fiber composite rods," Canadian Society for Mechanical Engineering Forum.

[35] Poisson, E., 2009, "Automation of Continuous Composite 2D Braiding Process," University of Ottawa. Canada.

[36] Sandess, J., Fahim, A., and Munro, M., 2008, "Rapid curing of 25 mm diameter continuous fibre composite rods," Canadian Society for Mechanical Engineering Forum.

[37] Sandness, J., 2008, "The Optimization of the Curing of Carbon Composite Rebar using Heat Transfer FEA Model," University of Ottawa. Canada.

[38] Hajihosseini, A., 2013, "Numerical Simulation of the Curing Process of Fiber Reinforced Polymer Composites," Blekinge Institute of Technology.

[39] Hajihosseini, A., Ayranci, C., and Carey, J. P. R., 2014, "Simulation of the rapid curing process for braid reinforced FRP rebar in braidtrusion process using a finite element analysis," SAMPE Conference Proceedings, Anonymous Seattle, WA.

[40] Fangueiro, R., Sousa, G., Soutinho, F., 2006, "Application of Braided Fibre Reinforced Composite Rods in Concrete Reinforcement," Materials Science Forum, **514-516**pp. 1556-1560.

[41] Ahmadi, M. S., Johari, M. S., Sadighi, M., 2009, "An Experimental Study on Mechanical Properties of GFRP Braid-Pultruded Composite Rods," Express Polymer Letters, **3**(9) pp. 560-568.

[42] Lebel, L. L., and Nakai, A., 2012, "Design and Manufacturing of an L-Shaped Thermoplastic Composite Beam by Braid-Trusion," Composites: Part A, **43**pp. 1717-1729.

3 PSEUDODUCTILE FRP REBAR DESIGN

3.1 INTRODUCTION

The majority of FRP rebars available today are made from unidirectional fibers and are linear elastic to failure. Improving the ductility of FRP rebar will help to reduce the need for overly conservative design and may lead to more widespread adoption of these products. While ductility in typical FRP rebar is limited by the low failure strains of the constituent fibers, pseudoductile rebar can be created by deliberate design of the composite architecture and material selection.

In this thesis, the primary goal was to develop a new type of FRP rebar that performs in a pseudoductile manner when loaded in tension. In this chapter, an overview of the basic rebar design concept is outlined, along with the materials used. The impact of important geometric factors on the rebar properties is also discussed. Detailed information on the manufacturing, characterization, and pseudoductile failure mechanisms are presented in later chapters.

3.2 DESIGN CONCEPT AND MATERIALS

Several important criteria were identified for the FRP rebar design, including a high elastic modulus, a ductile failure mode, and ease of manufacturing. To achieve these goals, a combination of material and structural hybridization was used, based on previous work by Somboonsong et al. [1], Hampton [2], and Ewen [3]. Material hybridization takes advantage of combining fibers with different elastic properties, while structural hybridization uses different geometrical factors to modify the composite properties.

The rebar structure was designed to consist of a unidirectional core made of high-modulus fibers, encased in an overwrap formed by lower modulus braided yarns. In this design, the rebar core serves to provide high stiffness to the rebar, due to the longitudinal orientation of the core fibers. The braid is used to form the cross-sectional shape of the rebar, and tailor the mechanical properties by modifying braid angle, while helping to provide the pseudoductile characteristics to the rebar. The rebar architecture is shown schematically in Figure 3.1, with the braid in grey and the core in black.

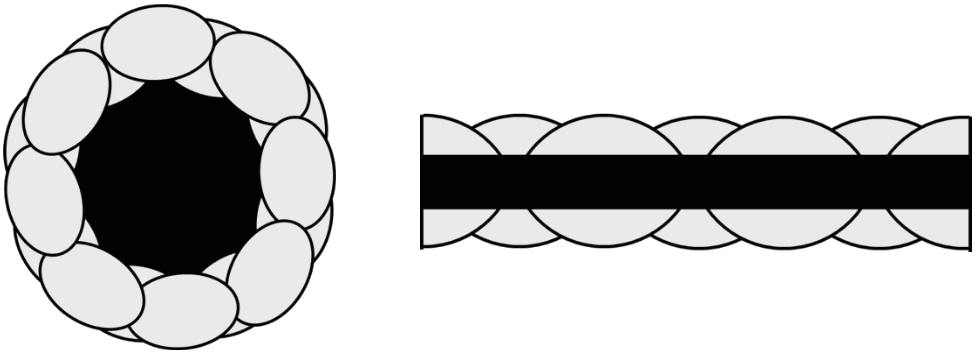
(a) (b)

Figure 3.1: Schematic of proposed rebar structure consisting of a unidirectional carbon fiber core (black), and braided aramid overwrap (grey). (a) Transverse cross-section, (b) longitudinal cross-section.

High modulus carbon fibers (Tenax® G50-500, Toho Tenax America Inc., USA) were used in the core, and lower modulus aramid fibers (Kevlar® 49, DuPont, USA) were used in the braid. The high elastic modulus of the carbon fibers helped to maximize the elastic modulus of the rebar, while the relatively high ultimate strain of the aramid fibers helped to add ductility to the rebar. This combination of fibers with low and high ultimate strains results in material hybridization in the rebar, which should allow for multiple stages of failure as different fibers fail at different strain values. A thermosetting polymer matrix was used, consisting of a combination of resin (EPON™ 826, Momentive, USA) and hardener (LS 81-K, Lindau Chemicals Inc., USA) mixed in a ratio of 1:0.94 by weight. The material properties of the fiber and matrix materials are summarized in Table 3.1 [4-7]. Apart from their mechanical properties, the specific materials used in this work were chosen due to availability, but using different material combinations is possible, and could help to tailor mechanical properties of the rebar to specific applications. Official material data was unavailable for the carbon fibers used in this work, therefore, elastic properties were found using single fiber tensile tests detailed in Appendix A.

Table 3.1: Summary of material properties of fibers and matrix used in the rebar [4-7]

Material	Toho Tenax G50-500	Kevlar 49	EPON 826/Lindau LS-81K
Elastic Modulus (GPa)	281.4	112.4	2.73
Tensile Strength (MPa)	2780	3000	73.8
Ultimate Strain (%)	0.99	2.4	5.0
Density (g/cm^3)	1.78	1.44	1.16
Denier (g/9000m)	6930	7100	N/A

3.3 GEOMETRIC FACTORS

During the preliminary rebar design, there were several important geometric factors to be considered. These included the relative proportions of core and braid structures, as well as braid angle. The choice of these factors will ultimately impact the manufacturing, geometry, and final mechanical properties of the rebar.

3.3.1 Braid and Core Proportions

In a hybrid composite made from two different types of linear elastic fibers with different failure strains, the low strain material will fail first. When this occurs, the failure can either lead to ultimate failure of the entire composite cross-section or the remaining high strain material can take over the load without immediate failure. Aveston and Kelly [8] introduced an expression (Equation 3.1) to predict the minimum volume fraction of high elongation material needed to bear the load after failure of the low strain component. In this equation, V_H is the volume fraction of the high strain component, σ_L is the ultimate strength of the low strain component, σ_H is the ultimate strength of the high strain component, and σ_H' is the stress in the high strain component when the low strain component fails. For linear elastic materials, σ_H' can be found by simply multiplying the elastic modulus of the high strain component by the ultimate strain of the low strain component ($\sigma_H' = E_H \varepsilon_L$). In order for the hybridization to be successful in avoiding catastrophic failure, the condition in Equation 3.1 must be met. This equation was used to guide the initial rebar design, and ensure that the proportions of the core and braid were such that the high strain yarns of the braid was able to support the load after failure of the low strain core yarns.

$$V_H \geq \frac{\sigma_L}{\sigma_H + \sigma_L - \sigma'_H} \qquad [3.1]$$

A combination of 12 core yarns and 18 braid yarns was chosen to satisfy this minimum requirement. It should be noted that for the braid, the number of yarns was limited to multiples of 18 due to the braiding configuration that was used. The selection of the number of braid and core yarns not only effects the mechanical properties of the rebar, but also influences the geometrical properties such as diameter and braid angle.

3.3.2 Braid Angle

Braid angle is an important factor to the design of the FRP rebar, as it influences both the mechanical properties and geometry of the final composite. It has been shown that an increasing braid angle leads to a decreasing longitudinal elastic modulus of the composite [9], as the fibers are oriented off the loading axis of the rebar. Conversely the elastic modulus can be increased by decreasing the braid angle.

Braids can be either open or closed mesh, depending on the amount of space between braid yarns. This can be described by the cover factor, which is the ratio of the mandrel surface that is covered by braid yarns [10]. When the cover factor is less than 1, there is space between the braid yarns, resulting in an open mesh braid. However, when the cover factor is equal to its theoretical maximum value of 1, the mandrel is completely covered, with no spaces between braid yarns. In this case, the braid is referred to as jammed [10].

When a braid is in the jammed state, the braid angle cannot be increased without increasing the diameter of the braid [10]. The jamming angle can be predicted using Equation 3.2, developed by Du and Popper [10], where w_y is the yarn width, R_m is the mandrel radius, and N_c is the number of carriers used in the braiding process. This jamming phenomenon places a lower limit on the diameter of braid that can be manufactured for a given braid angle, and can therefore place a constraint on the possible dimensions of the FRP rebar. In addition, the mechanical properties of a jammed braid differ from an open mesh braid, and are largely dominated by the properties of the yarns [11].

$$\cos\theta_j = \frac{w_y}{2R_m \sin\left(\frac{2\pi}{N_c}\right)} \quad [3.2]$$

One of the difficulties that arose when using this equation is that the yarn width, w_y, can be difficult to measure in practice. Therefore, in addition to this equation, preliminary trial and error testing of the manufacturing process was conducted to guide the selection of braid angle. The resulting braid angle used for the rebar was approximately 21°, and the braid structure was in the jammed state. More details on the selection and measurement of braid angle, as well as relevant manufacturing parameters for the final rebar can be found in Chapter 4.

3.4 SUMMARY

In this research, the primary objective was to develop FRP rebar that behaves in a pseudoductile manner when loaded in tension. A design consisting of a unidirectional carbon fiber core and braided aramid overwrap, combined with a thermosetting polymer matrix was used to produce FRP rebar. The rebar makes use of both material and structural hybridization in order to tailor the mechanical properties and create the pseudoductile failure mechanism. The selection of core and braid proportions, as well as braid angle are important to the final mechanical and geometrical properties of the rebar. In this chapter, formulae are introduced to help guide the selection of braid angle and number of yarns used for the core and braid structures of the rebar. Preliminary calculations and testing led to a choice of 12 core yarns, and 18 braid yarns, with a braid angle of approximately 21°.

3.5 REFERENCES

[1] Somboonsong, W., Ko, F. K., and Harris, H. G., 1998, "Ductile Hybrid Fiber Reinforced Plastic Reinforcing Bar for Composite Structures: Design Methodology," ACI Materials Journal, **95**(6) pp. 655-666.

[2] Hampton, F., 2004, "Cyclic Behavior, Development, and Characteristics of a Ductile Hybrid Fiber Reinforced Polymer (DHFRP) for Reinforced Concrete Members," Drexel University. United States.

[3] Ewen, K., 2005, "Ductility in FRP Rods for Concrete Reinforcement by Interfacial Shearing," University of Ottawa. Canada.

[4] Toho Tenax America, I., 2009, "Tenax Carbon Fibers".

[5] DuPont, "Technical Guide: Kevlar Aramid Fiber".

[6] Momentive, 2005, "Technical Data Sheet: EPON Resin 826," pp. 1-3.

[7] Lindau Chemicals Inc., 2002, "Technical Data Sheet, Epoxy Resin System for Pultrusion: LS-81K Anhydride Curing Agent," pp. 1-6.

[8] Aveston, J., and Kelly, A., 1980, "Tensile First Cracking Strain and Strength of Hybrid Composites and Laminates," Physical Sciences, **294**(1411) pp. 519-534.

[9] Ayranci, C., and Carey, J. P., 2010, "Predicting the Longitudinal Elastic Modulus of Braided Tubular Composites using a Curved Unit-Cell Geometry," Composites: Part B, **41**pp. 229-235.

[10] Du, G., and Popper, P., 1994, "Analysis of a Circular Braiding Process for Complex Shapes," The Journal of the Textile Institute, **85**(3) pp. 316-337.

[11] Ko, F., Head, A., and Pastore, C., 1989, "Handbook of Industrial Braiding," Atkins and Pearce, Covington, Kentucky.

4 MANUFACTURING AND CHARACTERIZATION OF FRP REBAR

4.1 INTRODUCTION

Traditional unidirectional FRP rebars are typically manufactured using a pultrusion process, which allows for continuous production of constant cross-section bars at high production rates compared to other composite manufacturing techniques [1, 2]. More recently, some researchers have begun producing rebar using a process called braidtrusion, which combines aspects of pultrusion and braiding into a single manufacturing method, allowing for the continuous production of FRP rebar consisting of a combination of unidirectional and off-axis oriented fibers. This process was originally developed by Ko and Pastore [3] and has since been used in various applications including the production of hybrid composite rebar [4-7], and adding surface deformations to FRP rebar to enhance bonding properties [8, 9].

The braidtrusion process is ideally suited to the production of hybrid composite bars, and enables the composite properties to be tailored based on the selection of processing parameters. When manufacturing FRP rebar using this method, it is important to understand how different processing parameters affect the final architecture of the composite, as this can have a significant impact on the final mechanical properties of the rebar. In this chapter, a new variation on the braidtrusion process for the manufacturing of pseudoductile FRP rebar is introduced and the various parts of the manufacturing process are described in detail. The composite architecture of the rebar produced by this process is characterized and equations are presented that allow for important macro and microstructural properties to be predicted based on simple processing parameters. The validity of these equations is examined by comparison to experimental results.

4.2 MATERIALS AND METHODS

4.2.1 Rebar Manufacturing

The rebar was manufactured using a pilot-scale dieless braidtrusion process, shown schematically in Figure 4.1, developed in the Mechanical Engineering Department at the University of Alberta. This process combines aspects of braiding and pultrusion, and can be broken down into four main zones. First, there is the pultrusion and primary impregnation zone, followed by braiding and secondary impregnation. Next there is the curing zone, and finally the pulling and cutting zone. This manufacturing process allows for the continuous production of the composite rebar and has the potential to be scaled up in the future for high-volume industrial rebar production. The entire braidtrusion system was contained in an enclosure under negative pressure to suck out any airborne carbon fiber and fumes caused during curing.

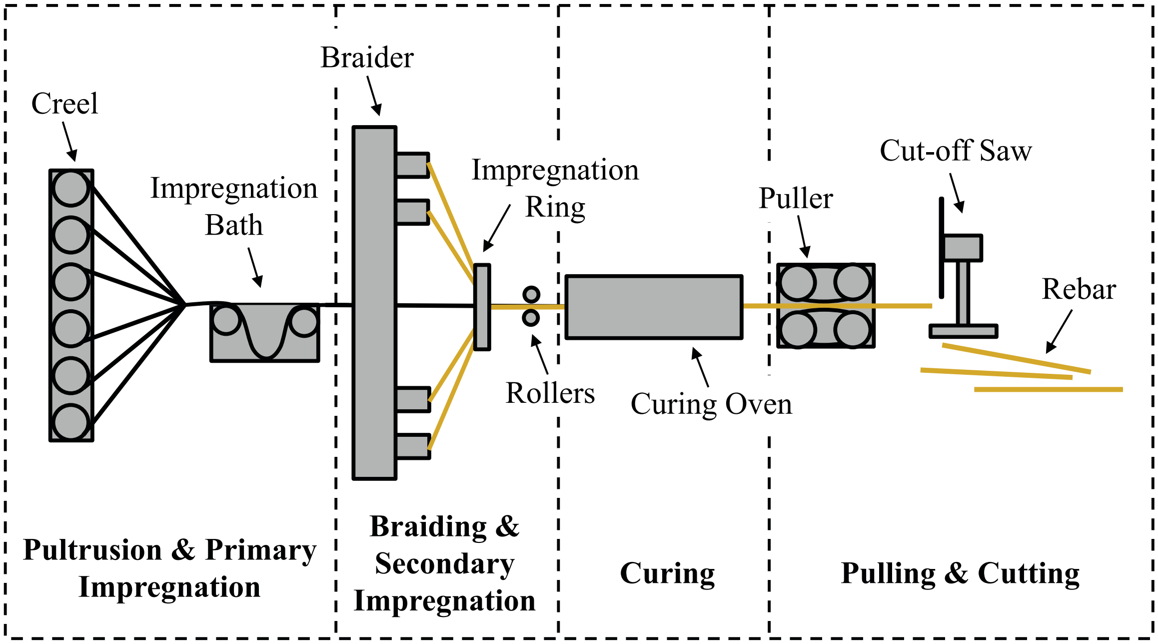

Figure 4.1: Schematic of the dieless braidtrusion manufacturing line

4.2.1.1 Pultrusion and Primary Impregnation

In the first zone, spools of carbon fiber yarns are loaded onto a creel for pultrusion, as shown in Figure 4.2(a). These will become the core yarns in the final rebar structure. When dry, the brittle carbon fibers are susceptible to physical damage, which can negatively impact their performance in the finished composite [4]; therefore, the creel was designed with angled racks to avoid contact between the carbon yarns as they are pulled from the spools. Each individual spool is tensioned in order to ensure that the pultruded yarns remain straight and aligned in the longitudinal direction, and are under uniform tension in the final composite. This helps to ensure consistency in the mechanical performance of the final composite, allowing all fibers to contribute equally to the structure [10]. The yarns converge through a series of guides made with smooth surfaces and rounded corners, which minimize potential fiber damage caused by friction.

The converged yarns then pass through the primary impregnation step consisting of a resin bath, shown in Figure 4.2(b). The core yarns are dipped via a series of rollers into a basin filled with a pre-mixed resin-hardener mixture. During mixing, the resin and hardener are heated to 40 ˚C to reduce viscosity and ensure a homogeneous and bubble-free mixture. The mixture is then placed in an oven at 40 ˚C for 30 minutes to allow for degassing of the mixture. The resin bath is also heated to 40 ± 1 ˚C to maximize pot life and maintain low viscosity of the resin, which facilitates better wetting of the carbon fibers. The resin was heated using a resistive heating pad adhered to the bottom of the steel basin. Temperature of the resin was measured by a thermocouple, which was used as feedback to the temperature controller (Omega® CN74000, Omega, USA).


(a) (b)

Figure 4.2: (a) Creel loaded with carbon fiber spools, (b) core yarns passing through impregnation bath

4.2.1.2 Braiding and Secondary Impregnation

After primary impregnation, the core yarns continue to the braiding step where the braid is formed over the impregnated core, which acts as the mandrel for the braiding process. A maypole braider (D-5600, Steeger, Germany), shown in Figure 4.3(a), was used. The braider is equipped with 18 horn gears and loaded with 18 carriers arranged to produce a diamond braid pattern. A forming ring is used to help set the convergence point of the braid and ensure consistency of the braid structure. Figure 4.3(b) shows the convergence of the braid yarns around the carbon core. A rotational speed of 1.7 RPM was used for the braiding process, resulting in a tension-jammed braid with a cover factor of 1.0, and a nominal braid angle of approximately 21˚

as mentioned in the previous chapter. Preliminary tests were done to calibrate the braider speed control; details can be found in Appendix B.

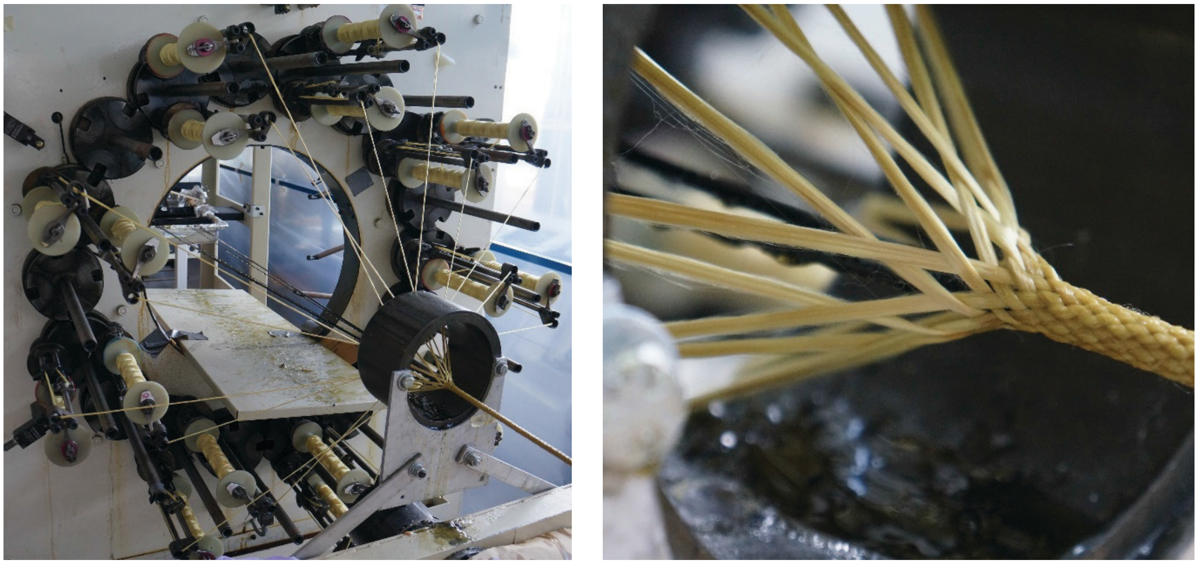
(a) (b)

Figure 4.3: (a) Maypole braider loaded with 18 spools of Kevlar 49 yarns, (b) convergence of braid yarns over impregnated core

A secondary impregnation step, shown in Figure 4.4 was incorporated into the braiding process to impregnate the braid yarns. An impregnation ring was used in the place of a conventional forming ring to wet the braid yarns as they converge onto the core. The impregnation ring takes the place of the forming ring, and serves both purposes of impregnating the braid yarns and setting the convergence point. Resin is pumped into the ring, and out of holes located on the inside circumference of the ring. Resin saturates the inner circumference, and the braid yarns are impregnated as they slide across this surface during braiding. The braiding motion causes the braid yarns to rub back and forth against the ring, effectively massaging the resin into the yarns. Similar to the primary impregnation step, the resin is pre-mixed and heated to 40 ± 1 ˚C before it is pumped into the ring. The resin is pumped using a peristaltic pump (Masterflex L/S Easy-Load II, Cole Parmer, USA) from a steel basin where it is heated using a resistive heating pad regulated by a thermocouple and temperature controller (Omega® C360, Omega, USA).

Ring impregnation leads to a large quantity of excess resin on the outer surface of the braid. To address this, the rebar passes through a series of rollers, which apply pressure to the external surface of the braid and wipe away excess resin, which is captured, reheated, and re-circulated to the impregnation ring. Preliminary work used to select the impregnation methods used in the final braidtrusion process can be found in Appendix C.

Figure 4.4: (a) Overview of secondary impregnation step

4.2.1.3 Curing

The rebar then moves through a series of ovens to be cured. A dieless braidtrusion process was used, meaning that curing was not done using a heated die as is common with other similar processes [3, 7, 11-13]. Instead, the rebar was cured by a pair of in-line tube ovens, shown in Figure 4.5(a). A steel tube is placed inside the ovens, and serves as a liner to prevent any resin drips from falling onto the heating elements. The tube is sectioned longitudinally to allow easy access to the rebar inside the ovens. When operating, the top half of the tube is replaced to promote consistent heating conditions all around the rebar and prevent uneven curing. Six thermocouples were positioned to measure air temperature inside the ovens, as shown in Figure 4.5(b).

Figure 4.6 shows a schematic of the full heating setup used for curing. Two ovens were used; oven #1 (SF17, Satec Systems Inc, USA) contained of 3 separate heating zones, each regulated independently, and oven #2 (54451, Lindberg, USA) contained only a single heating zone. These ovens were chosen based on availability. The multiple independent heating zones in oven #1 allow for more granular control over the curing temperature than the single zone in oven #2. This is most important at the inlet and outlet, where the ovens are open to the ambient air. Thermocouples were positioned inside the ovens at the locations specified in Figure 4.6. Three thermocouples were used in oven #1, and were positioned in the middle of each heating zone. The other three thermocouples were evenly spaced inside oven #2. A program was written in LabWindows CVI using a simple on/off control system to regulate the oven temperatures around a user-defined setpoint of 160˚C. Zones 1, 2, and 3 were controlled based on readings from thermocouples TC1, TC2, and TC3 respectively. Zone 4 was controlled using the average measured temperature of TC4, TC5, and TC6 combined.

Figure 4.7 shows a typical plot of thermocouple readings over the course of a rebar production run. After the initial heat-up process, the oven temperatures stabilized relatively well, with only small fluctuations in temperature. Rebar production was started after temperature stabilization, and any rebar left in the ovens during the heat up or cool down of the ovens was discarded. Table 4.1 shows the average and standard deviations of the stabilized temperature readings for each of the thermocouples during a typical production run. The average temperature (+/- standard deviation) measured from all thermocouples combined was 160.1 ± 7.4˚C. Zones 1, 2, and 3 were maintained relatively close to the 160 ˚C setpoint, and even allowed for temperature at the inlet to be well maintained, despite being open to the air. Zone 4 in oven #2 showed a wider range of temperatures. Because this oven only had one heating element and the temperature was controlled based on the average of TC4 TC5 and TC6, temperature at the outlet was consistently lower than the setpoint, while temperature in the rest of the oven was slightly above the setpoint. The temperature distribution could be improved in the future by using an oven with multiple independent heating zones, similar to oven #1. It should be noted that even though the temperature was not constant throughout the entire curing process, each point on the rebar was exposed to the same curing conditions, since the process operates continuously. The total combined length of the ovens was 1250 mm, and rebar was pulled through the system at a rate of 77.2 mm/min, resulting in a total curing time spent inside the ovens of 16.2 min.

The total length of the heating step directly impacts the maximum production rate that can be used, since the rebar needs to spend a minimum amount of time inside the ovens to achieve full cure. Decreasing the total oven length could allow for a shorter overall system, but would require a slower production rate. Increasing the length of the curing zone would allow for faster production rates. A longer curing zone may also lead to a less pronounced impact of the inlet and outlet on the overall temperature distribution, since these regions would make up a smaller percentage of the total length.

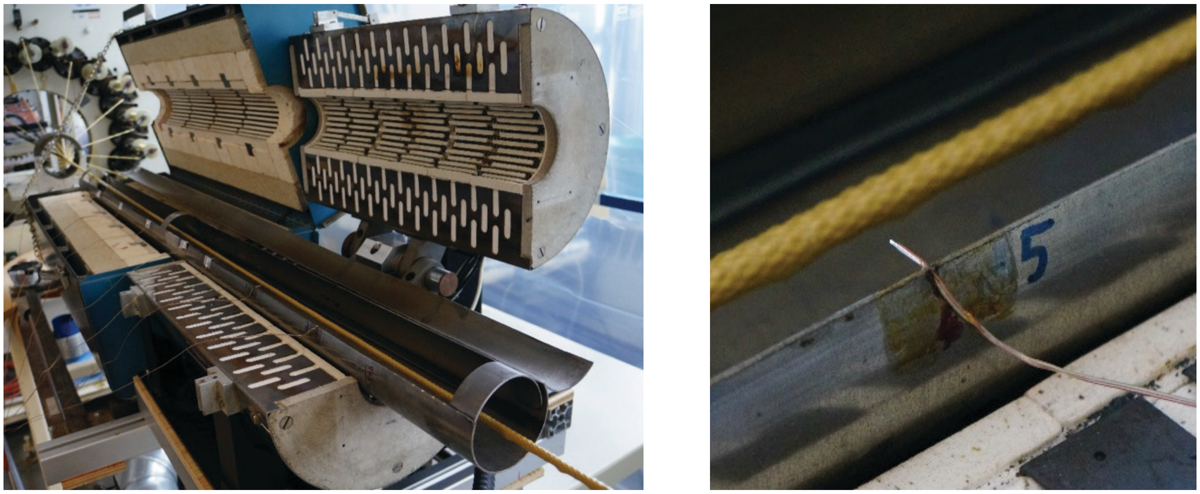

(a) (b)

Figure 4.5: (a) Opened curing ovens with steel tube liner in place, (b) positioning of thermocouple inside ovens

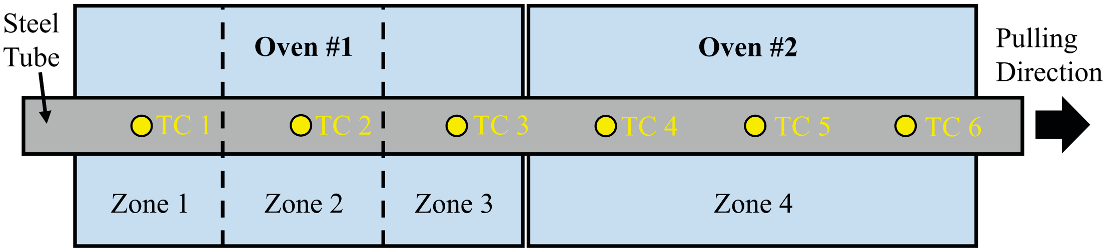

Figure 4.6: Schematic of heating zones in ovens #1 and #2 as well as relative thermocouple locations. Thermocouples are labeled TC1 to TC6

Table 4.1: Summary of temperature distribution inside ovens as measured by thermocouples

Thermocouple	TC1	TC2	TC3	TC4	TC5	TC6
Average Temperature (˚C)	161.6	161.7	160.8	165.5	165.3	145.4
Standard Deviation (˚C)	2.2	1.0	2.0	0.7	1.1	1.7

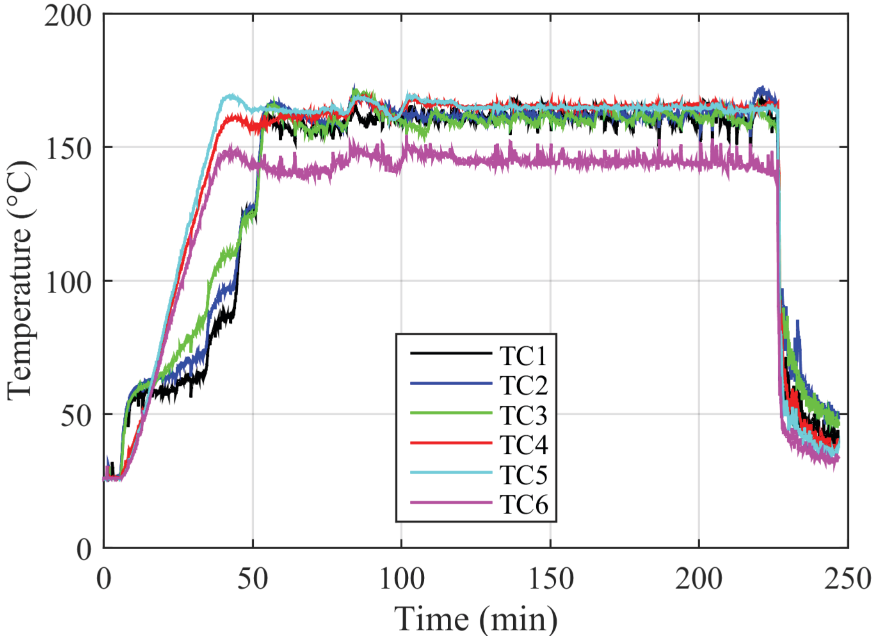

Figure 4.7: Representative plot of temperature readings at thermocouples for a rebar production run. Temperature ramps up to user-selected temperature, stabilizes, and then ramps down after production is complete.

4.2.1.4 Pulling and Cutting

The rebar is advanced using a caterpillar-type puller, shown in Figure 4.8(a). Two synchronous belts are clamped down on the cured rebar and pull it through at a constant rate. The pulling rate helps to determine the braid angle and also dictates the amount of time the rebar resides inside the ovens for curing. Preliminary testing used to calibrate the puller speed control can be found in Appendix B. After exiting the ovens and before entering the puller, the rebar is air cooled to avoid heat damage to the belts. Finally, the rebar is cut to length using a miter saw (Ryobi, USA) located at the end of the line, as shown in Figure 4.8(b). The miter saw was equipped with a fine-toothed blade, rated for cutting polymeric materials.

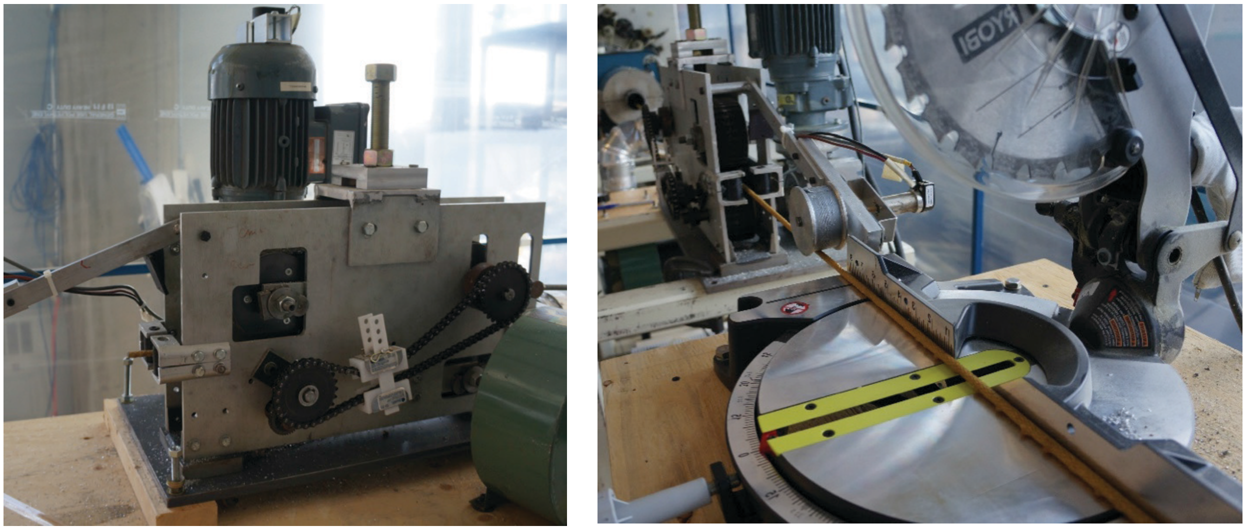

(a) (b)

Figure 4.8: (a) Caterpillar-type puller used toadvance rebar, (b) miter saw used to cut finished lengths of rebar

4.2.2 Prediction of Rebar Architecture

The ability to accurately predict the geometry of the rebar structure formed by a particular set of production parameters will facilitate future predictions of mechanical properties. Braid angle, shown schematically in Figure 4.9(a), is defined as the angle between the longitudinal axis of the braid and the braid yarn orientation [14]. For a conventional braiding process, braid angle, θ, can be predicted based on the braid midpoint diameter, D, and the helix length, L_h, of the braid yarns, using Equation 4.1 [14-16]. As shown in Figure 4.9(b), the helix length is the axial length required for a braid yarn to complete a full revolution around the mandrel. During the braiding process, L_h can be set based on the longitudinal pulling speed, v_L (mm/min) and the rotational speed of the braider v_R (RPM). Braid angle can have a significant effect on the mechanical properties and final cross-sectional area of the rebar, making it important to be able to accurately set the braid angle of the rebar by changing these processing parameters.

$$\tan\theta = \frac{\pi D}{L_h} = \pi D\left(\frac{v_R}{v_L}\right) \qquad [4.1]$$

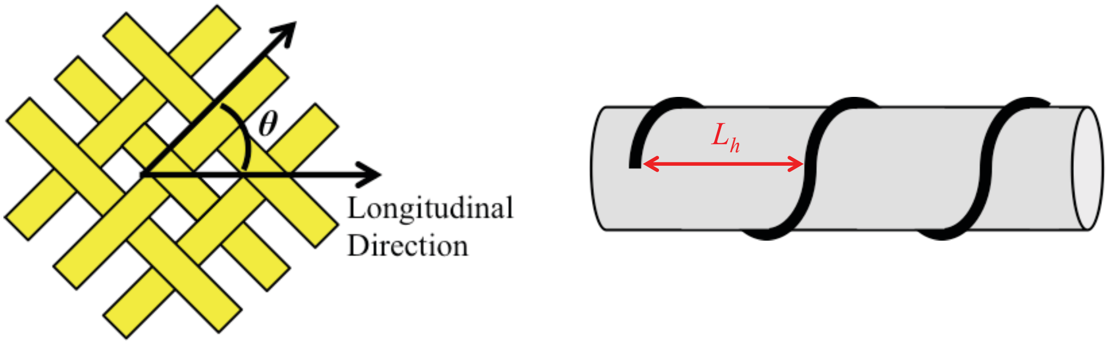

(a) (b)

Figure 4.9: (a) Schematic showing definition of braid angle, *θ*, relative to the longitudinal direction of the braid, (b) schematic of a single braid yarn wrapped around a mandrel, showing helix length, L_h

The impregnated areas of the core and braid portions of the rebar can be predicted analytically using Equation 4.2 [5]. Impregnated area refers to the total cross-sectional area occupied by either the cured braid or core structure, including area taken up by both fibers and matrix. These cross-sectional areas will help to define the mechanical properties of the rebar. The predictions rely on the linear density, *den*, specific gravity, ρ, and braid angle, θ, of the selected yarns, as well as the fiber volume fraction, V_f, and number of yarns, N_c, in the composite. In this equation, ρ is in units of g/cm^3, and *den* is expressed in units of denier, where 1 denier is equal to 1 g per 9000 m of yarn. When calculating area of the core, the angle, θ, is equal to zero, since the yarns are aligned in the axial direction.

$$A_{impreg} = \frac{\frac{N_c den}{9000\rho\cos\theta}}{V_f} \qquad [4.2]$$

In order to verify the validity of these equations, the rebar produced by the braidtrusion process was characterized and the measured quantities were compared to the analytical predictions.

4.2.3 Microstructural Characterization

Microstructural characterization was conducted on the manufactured rebar. The microstructure of the rebar was examined in order to evaluate the composite architecture and quality of the composites resulting from the dieless braidtrusion process. This knowledge will be essential in the future towards understanding the mechanical performance of the composite.

4.2.3.1 Optical Microscopy

The rebar was examined by optical microscopy to analyze the microstructure of the composite and assess the effectiveness of the current manufacturing process. The analysis was conducted on cross-sections of multiple rebar specimens taken at random locations. To prepare the specimens for analysis, the cross-sections were cut and mounted in epoxy (ColdCure, Industrial Formulators Inc., USA). The mounted cross-sections were then ground using 320 grit sandpaper, followed by 600 grit sandpaper. Next, the surfaces were polished using a 9 μm diamond slurry, then a 3 μm diamond slurry, and finally a 0.05 μm alumina suspension for fine polishing. The polished samples were imaged under an optical microscope (Olympus® BX61, Olympus, USA) to examine microstructural characteristics including fiber wetting in the braid and core, fiber dispersion and distribution, and the interface between the braid and core, among any other features of interest.

4.2.3.2 Scanning Electron Microscopy

Select rebar cross-sections were also imaged by scanning electron microscopy (SEM) to examine the fiber-matrix interface in the specimens, and other microscopic features that could not be resolved under the optical microscope. Specimens were cut, mounted, ground, and polished following the same procedure described for optical microscopy. After polishing was complete, a conductive gold coating was applied to the specimens using a sputter-coating instrument (Model 682 PECS™, Gatan Inc., USA) to allow the samples to be imaged in the SEM without excessive charging, due to the non-conductive nature of the aramid fibers and epoxy matrix. Conductive carbon tape was used to ground the samples to the microscope (Vega-3, TESCAN, Czech Republic). SEM scans were conducted in secondary electron mode, with an accelerating voltage of 20 kV.

4.2.4 Determination of Cure Fraction by Differential Scanning Calorimetry

Differential scanning calorimetry (DSC) was conducted in order to characterize the degree of cure of the thermoset matrix in the manufactured rebar [17-19]. DSC is a thermomechanical analysis technique where heat flow into or out of a sample is measured under heating, cooling, or isothermal conditions [18]. The heat flow is measured as a function of time or temperature and can be used to determine such properties a glass transition temperature, onset and completion of cure, heat of cure, maximum rate of cure, percent cure, and heat capacity, among other properties [17, 18]. Matrix material was extracted from several locations of different rebar specimens for DSC analysis. Care was taken to ensure that no fibers were present in the specimens, as these would skew the test results. To facilitate this, only matrix from the outer portion of the rebar was used. The matrix material was ground into small pieces using a mortar and pestle in preparation for testing. Due to the relatively small diameter of the rebar, it was assumed that a high degree of cure measured from the outer portion of the rebar would translate to a high degree of cure throughout the structure. This assumption was supported by preliminary hardness testing comparing the matrix hardness in the core of the rebar to the hardness of the fully cured epoxy, as described in Appendix D. While a hardness test cannot be directly correlated to degree of cure, it can be used as a quality control measure for comparing degree of cure between samples [20]. Hardness values from the matrix in the core of the rebar were in good agreement with the fully cured epoxy samples, indicating that the core was well cured.

Specimens were loaded into the DSC instrument (DSC-Q100, TA Instruments, USA); temperature was equilibrated at 20 ˚C, then ramped to 230 ˚C at a rate of 10 ˚C/min while recording time, temperature, and heat flow. Data analysis was conducted using TA Universal Analysis software. All samples were tested in duplicate to ensure consistency in the results.

Degree of cure for a thermoset can be determined by comparing the residual heat of cure of the unknown sample to the heat of cure required to cure the material from 0 to 100% and is calculated by Equation 4.3 [18]. In this equation, $\Delta H_{uncured}$ is the heat of cure of the unknown sample, and ΔH_{cured} is the heat of cure to cause an uncured sample to achieve 100% cure. To find ΔH_{cured}, a DSC scan was conducted on the liquid mixture of resin and hardener.

$$\%\,Cure = \frac{(\Delta H_{uncured} - \Delta H_{cured})}{\Delta H_{uncured}} \times 100\% \qquad [4.3]$$

4.2.5 Measurement of Constituent Volume Fractions and Impregnated Areas

4.2.5.1 Constituent Volume Fractions by Burn-off Testing

Burn-off testing was conducted based on ASTM D3171 [21] in order to determine the overall constituent volume fractions of the rebar. In these tests, composite samples are heated to burn away the matrix material, while leaving behind the reinforcing fibers. The test allows for fiber, matrix, and void volume fractions to be calculated based on mass, density, and volume measurements. Samples weighing approximately 2 g were cut from the rebar specimens. The samples were weighed to the nearest 0.001 g and their volume was measured by water displacement method. Volume measurements were repeated three times for each sample, and the average volume was used for further calculations.

Samples dried and placed into porcelain crucibles of known mass, and into an oven at a temperature of 700 F (371 ˚C) for 7 hours. This temperature was chosen to be high enough for the matrix to burn away, yet low enough not to degrade the carbon or aramid fibers. The decomposition temperature of the carbon fibers is approximately 650 ˚C (1202 F) [22], and the decomposition temperature of the aramid fibers is between 800 F (427 ˚C) and 900 F (482 ˚C) [23]. After the burn-off process was complete, the samples were cooled to room temperature and reweighed. The core and braid were also weighed separately to allow their respective volume fractions to be found. Fiber, matrix and void volume fractions were calculated following Equation 4.4, where V_c is the constituent volume fraction, m_c is the measured constituent mass, ρ_c is the constituent density, and v_{total} is the total volume of the sample before burn-off. This method allowed the volume fractions of core fibers, braid fibers, matrix, and voids to be determined.

$$V_c = \frac{\frac{m_c}{\rho_c}}{v_{total}} \qquad [4.4]$$

4.2.5.2 Constituent Volume Fractions by Image Analysis

Because the rebar architecture consists of both pultruded and braided fibers of different types, braid and core areas were analyzed separately using an image analysis technique to determine the local constituent volume fractions in each region.

Polished rebar cross-sections were imaged using an optical microscope (Olympus® BX61, Olympus, USA). Microstructural images were taken at random locations inside the core and braid. The core was imaged at 500x magnification, while the braid was imaged at 200x magnification to balance the field of view with the ability to resolve individual fibers. A larger field allows for more fibers to be present in the image, resulting in a more representative sample of the overall structure. The nominal diameter of the carbon and aramid fibers was 8 μm and 12 μm respectively, which contributed to the choice of magnification. Image analysis was conducted on the core and braid separately. 48 images taken from nine different samples were examined for the core, and 43 images taken from the same nine samples were examined for the braid.

The images were processed using MATLAB® to segment the fibers from the matrix; detailed code used to achieve this can be found in Appendix E. Figure 4.10 shows the processing steps used for segmentation. The RGB color image is imported into MATLAB®, converted to grayscale, and cropped to remove the scale bar. Contrast is enhanced, and the image is thresholded based on contrast to create the segmented binary image. Finally, the pixel areas of the black and white regions are found and divided by the total image area to calculate the local fiber and matrix volume fractions in the braid and core. The core images showed excellent contrast between fibers and matrix, and good results were achieved using a conventional thresholding algorithm based on global image contrast. The braid images were more difficult to segment due to slight color and lighting changes across the images. To address this problem, a local adaptive thresholding algorithm [24] was used. This method changes the threshold dynamically across the image, allowing the image to be segmented while accounting for uneven illumination.

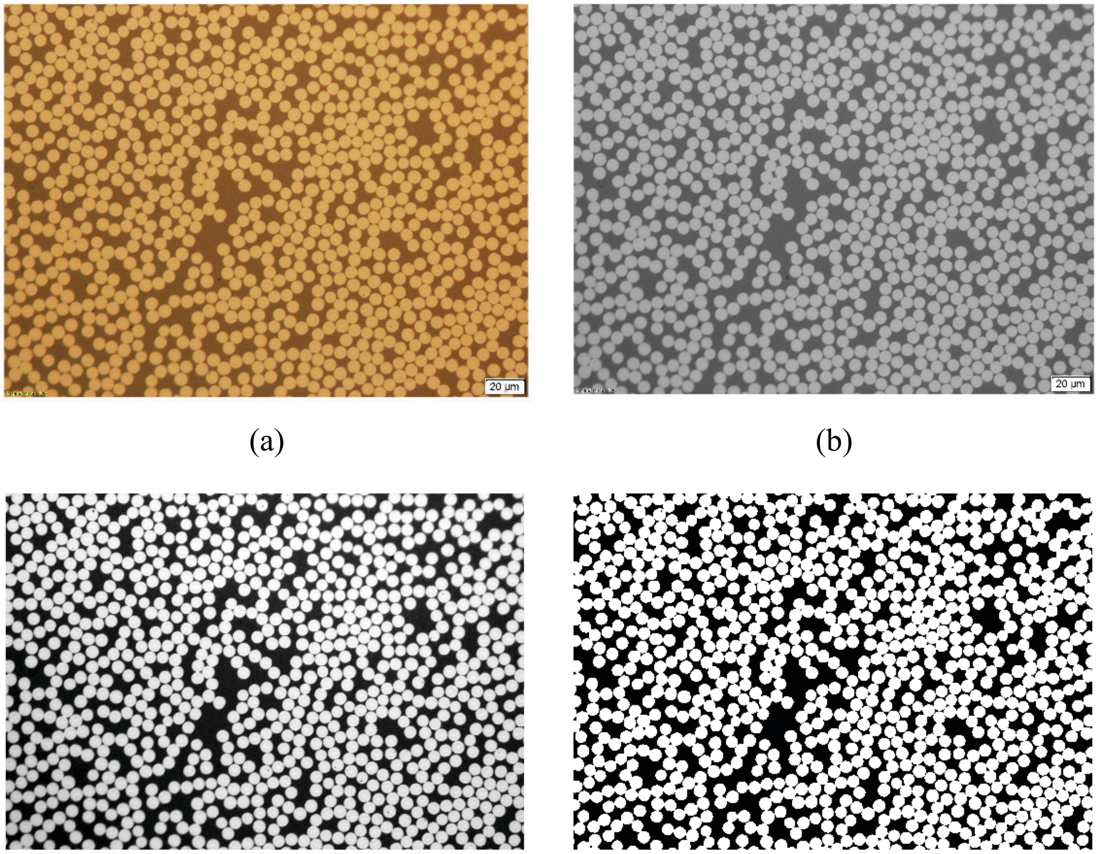

(a) (b)

(c) (d)

Figure 4.10: Image analysis steps used to segment fiber and matrix volume fractions in optical micrographs. (a) original image, (b) image converted to grayscale, (c) image cropped to remove scale bar and contrast enhanced, (d) final thresholded image based on contrast between fibers and matrix

4.2.5.3 Impregnated Areas by Image Analysis

Image analysis was also used to determine the impregnated areas of the braid and core. These measurements can be compared to the geometric predictions made in Section 4.2.2 to assess the validity of Equation 4.2. The impregnated areas of the core and braid portions of the rebar were measured from micrographs of nine separate rebar cross-sections.

Figure 4.11 shows an example of the processing steps that were taken to segment the images. Images were taken of the rebar cross-sections using an optical microscope (Olympus® BX61, Olympus, USA). Images of the entire rebar cross-section were assembled from overlapping pictures across the entire rebar cross-section using a feature in the microscope software (Olympus Stream, Olympus, USA). The cross-section images were imported into photo editing software (GIMP) for segmentation. Image contrast was adjusted to accentuate the boundaries of the braid, and core and the boundaries were traced manually at high magnification. To minimize bias from tracing of the areas by hand, each image was traced by three different people, and the average measurements from all three trials were used. Figure 4.11(a) shows the boundaries that were traced to obtain masks of the braid area (Figure 4.11(b)), the core area (Figure 4.11(c)), and the total rebar area, including the shell (Figure 4.11(d)). The original image and the masks were then imported into MATLAB®, where the areas of the core braid, interface, and shell were calculated in terms of square pixels. The core and braid areas were computed directly from their respective masks. The interface area corresponded to the white space between the core and braid masks. The shell area corresponded to the mask of the entire cross-section minus the core, braid, and interface areas. The pixel values were calibrated in using the scale bar present in the micrographs, in order to express the areas in units of μm^2. MATLAB® code used for the image analysis can be found in Appendix E.

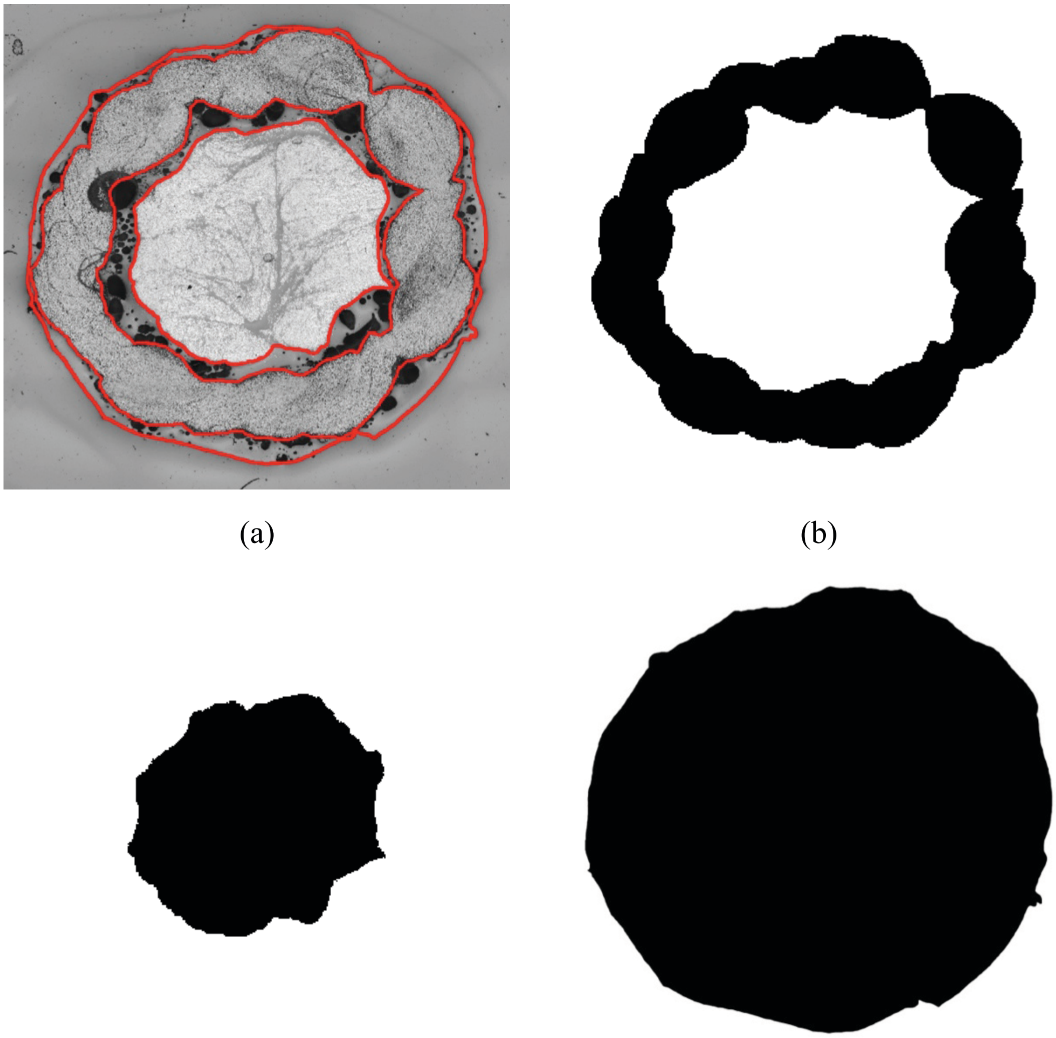

(a) (b)

(c) (d)

Figure 4.11: Image analysis steps used for segmentation of impregnated areas. (a) boundaries used to generate masks traced by hand on the cross-sectional image, (b) mask of impregnated braid, (c) mask of impregnated core, (d) mask of entire cross-section including outer shell

4.2.6 Braid Angle Measurement

Braid angle is an important macroscopic feature of the rebar that can influence mechanical properties and final bar geometry. Braid angle was measured by two different methods in this study. Braid angle can be difficult to measure accurately in practice; therefore the results of two separate methods were compared to ensure that the angles being measured were truly representative of the structure. If the results are comparable, then it can be assumed that the measured angles are correct.

In method 1, the midpoint braid diameter, D, and helix length, L_h, are measured, and the braid angle is calculated from Equation 4.1. The helix length can be measured easily and repeatedly from the braid surface. For the current braid configuration with 18 carriers, L_h corresponds to the distance between nine picks, where a pick is defined as the crossover region between two yarns [25], as shown in Figure 4.12(a). Helix length was measured at 40 different locations across various rebar specimens. The midpoint braid diameter is more difficult to measure. It can either be determined based on knowledge of the inner braid diameter and braid yarn width, or be measurement from cross-sectional images. In the current application, the yarn width was difficult to determine, as the yarns experience deformation during the braiding process. Therefore, the midpoint diameter was estimated based on the cross-sectional images. The inner and outer cross-sectional areas of the braid were found using similar image analysis methods as previously described. The inner and outer diameter of the braid was then calculated, assuming a circular cross-section, and the average of these two was taken to estimate the midpoint diameter. Nine separate images were used for midpoint diameter measurements.

In method 2, measuring braid angle consisted of direct angle measurements of individual crossover regions. Photos were taken of the braid surface, which were imported into image analysis software (ImageJ). For a given crossover region forming a diamond shape, three points were chosen at the corners of the diamond as shown in Figure 4.12(b). This angle was measured, and divided in half to obtain the braid angle. This method is highly sensitive to the selection of points; so all measurements were repeated three times in order to minimize measurement error. Measurements were conducted on 26 images, resulting in a total of 234 data points. When using this method, curvature of the rebar may have an effect on the measured braid angle. To minimize this effect, measurements were made only in the central portion of the rebar, away from the edges.

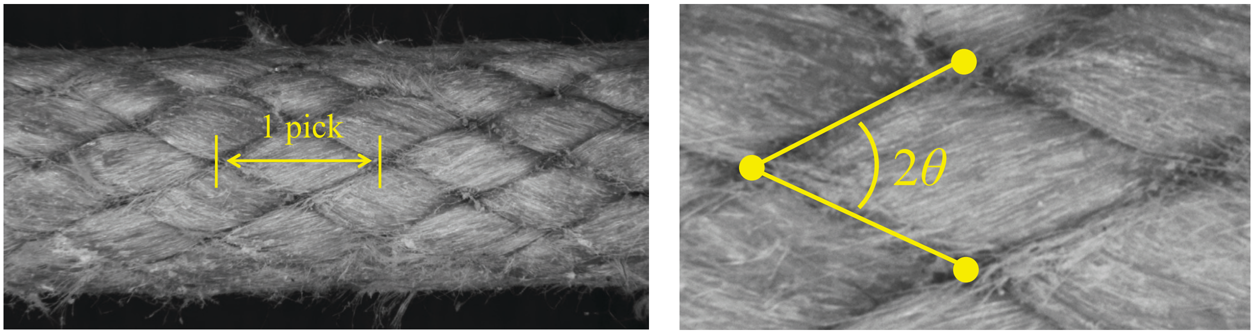

(a) (b)

Figure 4.12: (a) Image of braid surface, showing the length of 1 pick, (b) direct angle measurement from the braid surface, measured based on three corners of diamond shape

4.3 RESULTS AND DISCUSSION

4.3.1 Braidtruded rebar

An example of the resulting rebar produced by the dieless braidtrusion process is shown in Figure 4.13. The braid appeared to be in the jammed state, as there was no space between the crossover regions of the braid. The cured rebar was approximately circular in cross-section with a nominal outer diameter of approximately 6.45 mm. Since there was no forming die in the curing process, the cross-sectional shape of the rebar was dictated by the natural shape of the jammed braid [5]. This also resulted in undulations on the outer surface of the rebar, which may add to the bonding properties of the rebar when embedded in concrete [9]. Cured matrix-only drips were observed on the underside of the rebar as shown in Figure 4.13(a). These drips occurred during curing, and were not present on the rebar prior to entering the ovens. Inside the ovens, the liquid resin heats up before beginning to solidify. As it is heated, viscosity decreases, allowing excess resin to flow to the bottom of the bar, forming droplets on the underside, which are frozen in place as they cure. This is a limitation of the dieless curing process, as the outer morphology of the composite cannot be tightly controlled. Using a die in the braidtrusion process could help to eliminate the drips; however this would also have the consequence of removing the natural undulations of the braid surface, as seen in other similar processes [5, 26].

(a) (b)

Figure 4.13: Typical rebar produced by dieless braidtrusion. (a) side view showing resin drips, (b) image showing surface undulations and circular cross-section of rebar

4.3.2 Rebar Cure Fraction

DSC scans were conducted to assess the degree of cure that was achieved during manufacturing. Figure 4.14 shows a representative DSC curve for the cured rebar matrix, compared to the curves for uncured and fully cured resin. An average (± standard deviation) degree of cure of 99.5 ± 0.3% was found, which confirmed that the curing method and processing parameters used were acceptable for the production of composite rebar with a high degree of cure. A high degree of cure is necessary to maximize the mechanical performance of the composite [17], and it is therefore important to ensure that the curing process is effective. This type of analysis has not been reported for braidtrusion processes in the past, with most researchers simply assuming a well-cured composite [4-7, 13].

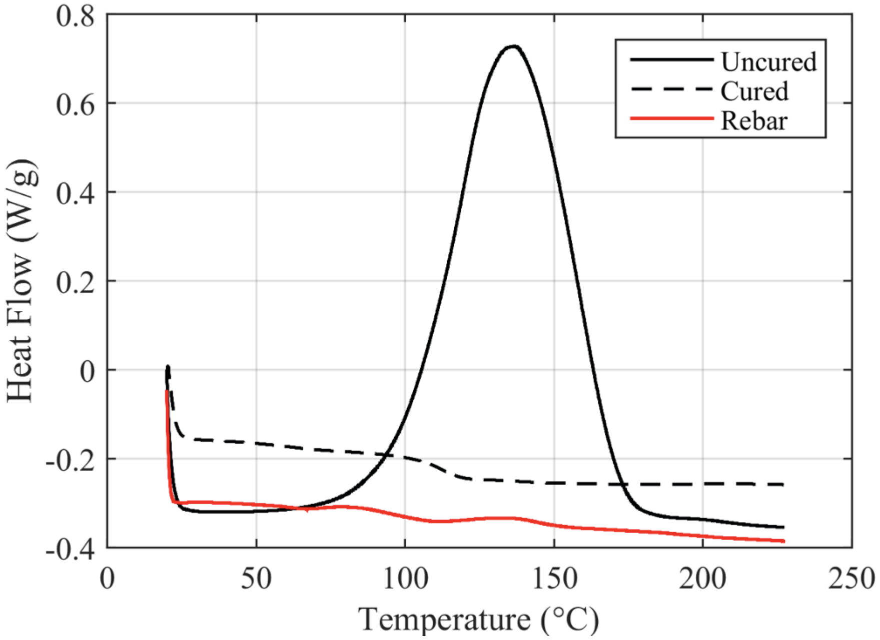

Figure 4.14: Representative DSC curve comparing heat flow of uncured specimen, fully cured specimen, and rebar matrix specimen. Rebar shows high degree of cure, approaching fully cured specimen.

4.3.3 Microstructural Characterization

4.3.3.1 Optical Microscopy

Optical microscopy was conducted to examine the microstructure of the rebar. Figure 4.15(a) shows a representative micrograph of a rebar cross-section. The core is generally well consolidated and reasonably circular in shape. The shape of the braid is also circular, which is to be expected for this type of braid. Because the braid is in the jammed state, there is a limit to the inner diameter of the braid [15]. In this case, this minimum diameter is larger than the core diameter, leading to separation between the core and braid, resulting in an interfacial region consisting primarily of matrix. Figure 4.15 shows a close-up of the core/braid interface. While some voids are present, the majority of the interface is filled with matrix and should provide adequate load transfer between the braid and core under mechanical loading. A resin-only “shell” is also observed on the outside surface of the braid due to excess resin on the outside of the rebar.

Figure 4.16 shows the typical microstructure within the braid yarns, and reveals good impregnation and tight fiber packing in the braid. Despite the tight packing, the majority of the braid fibers are surrounded by matrix, indicating generally good fiber wetting. The microstructure of the core is shown in Figure 4.17. Overall, the core is well impregnated and free of large voids, with excellent fiber wetting. The fiber distribution is good overall; however, some resin-rich regions are present and the core fibers were less tightly packed than those in the braid. This may be due to the lack of pressure exerted on the core, due to the limitations on the inner diameter of the jammed braid.

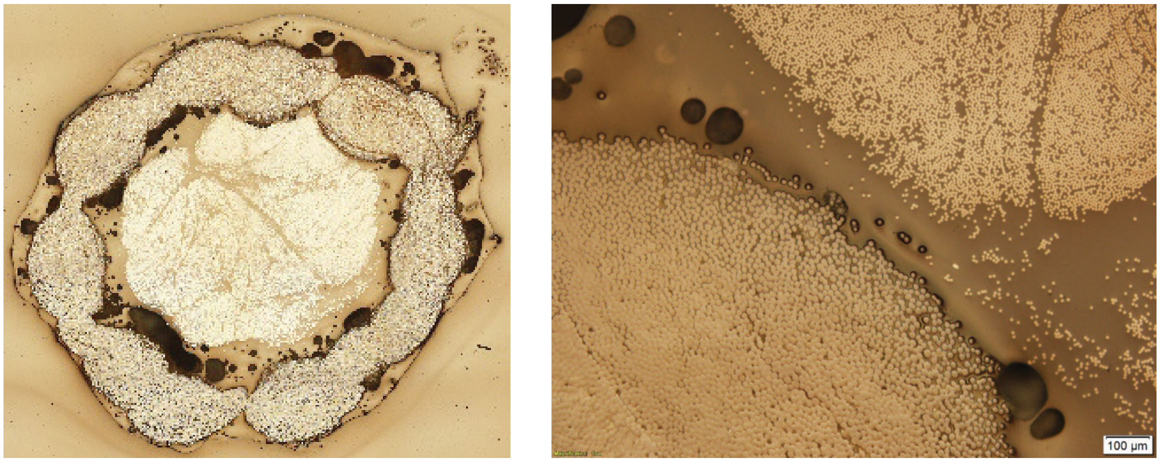

(a) (b)

Figure 4.15: Closeup of improved core/braid interface showing resin making up the majority of the interface, with somerelatively small voids still present in the structure

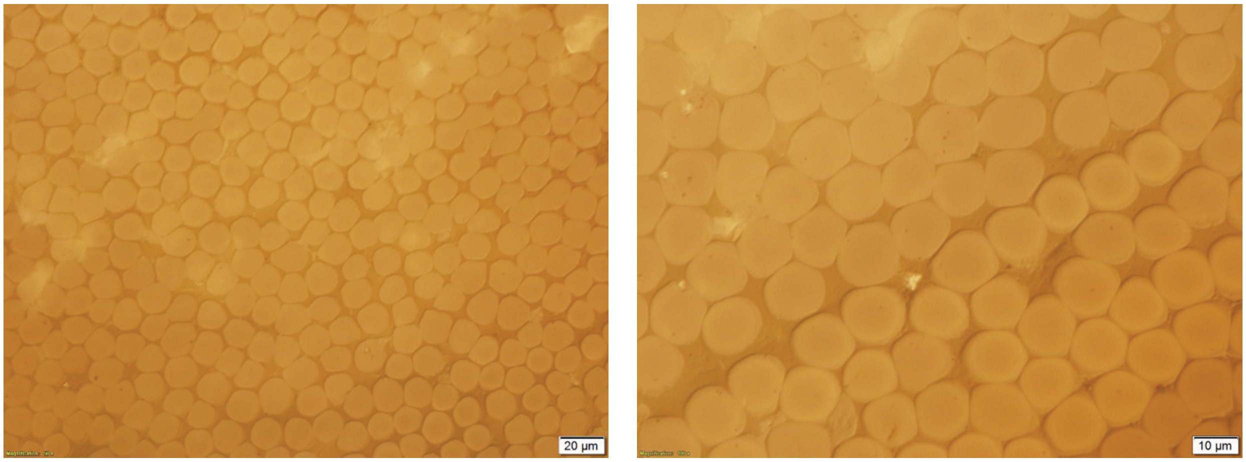

(a) (b)

Figure 4.16: Representative microstructure of braid showing less dense fiber packing and improved impregnation with more complete fiber wetting

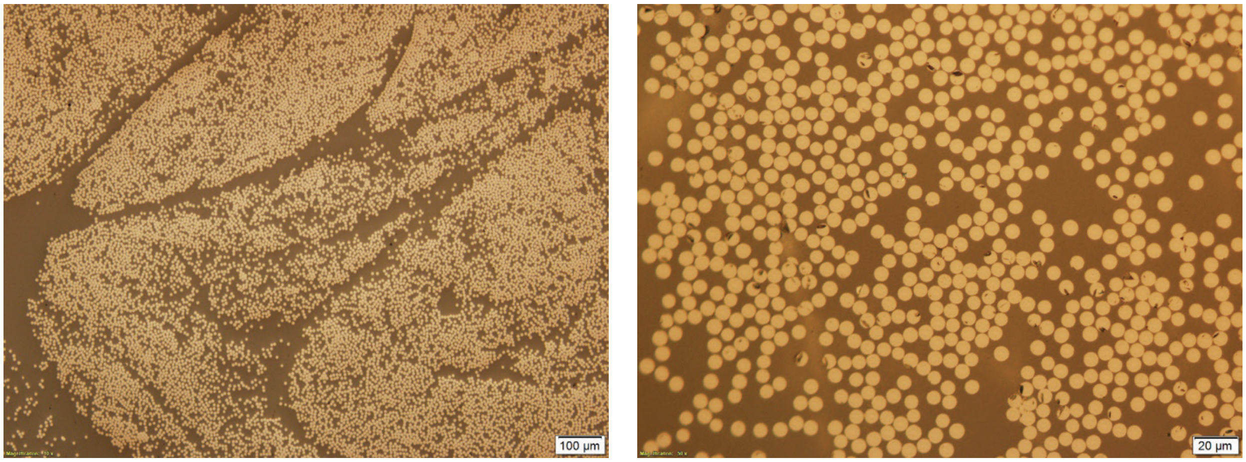

(a) (b)

Figure 4.17: Representative images of core microstructure showing (a) resin reich regions present in the core, (b) good fiber wetting of individual carbon fibers in the core

4.3.3.2 Core and braid microstructure assessment using SEM

SEM analysis was conducted on the rebar to further examine the microstructure of the core and braid. Figure 4.18(a) shows a close-up image on one of the core carbon fibers. As expected, the fiber is fully surrounded by matrix material. Small voids on the order of 300 nm in diameter were visible in the matrix surrounding the carbon fibers. This may be due to the presence of air bubbles trapped in the resin during manufacturing, and may be minimized by allowing the resin more time to degas prior to application, or if the rebar structure were adjusted for the braid to squeeze the core more tightly. However, it is unlikely that all bubbles will be able to be eliminated, as the impregnation process is open to the air.

Figure 4.18(b) shows an example of the fiber-matrix interface in the braid. Fibers are packed more tightly than the carbon fibers with less matrix present in between fibers. While the majority of the center fiber is surrounded by matrix, there are some points were direct fiber on fiber contact occurs, however, overall, good fiber wetting was achieved. Comparison to other composites produced by braidtrusion is difficult, as previous studies have only considered general fiber packing at low magnifications [5, 7, 10]. As the braidtrusion process continues to be refined in the future, these images can serve as a point of comparison when assessing the impregnation quality of the bars.

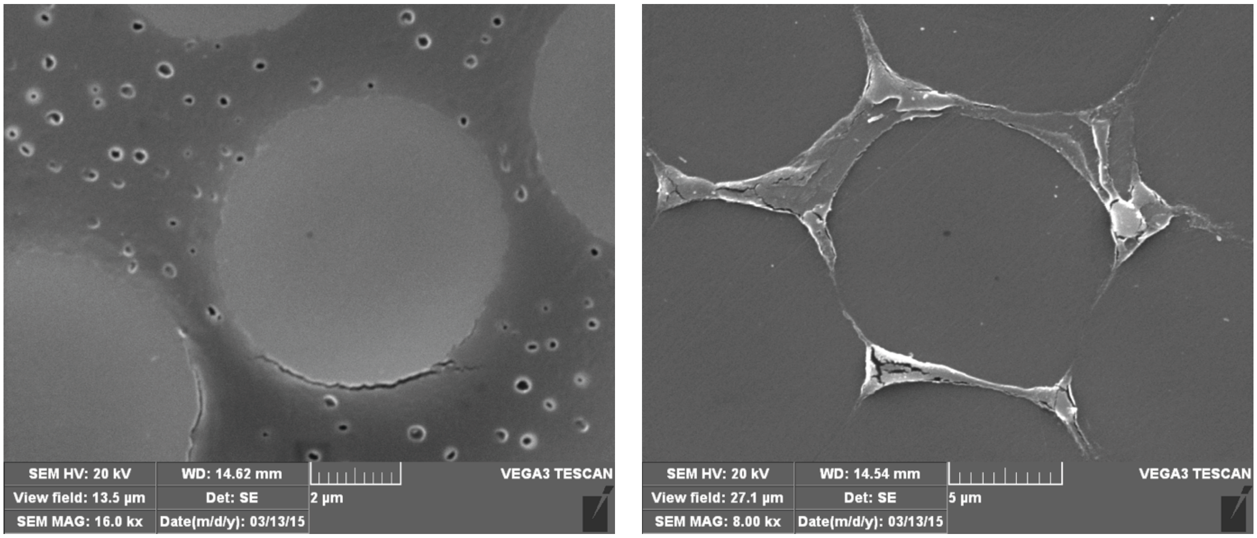

(a) (b)

Figure 4.18: Closeup of fiber-matrix interface for (a) carbon fiber in core, (b) Kevlar fiber in braid

4.3.4 Constituent Volume Fractions

4.3.4.1 Overall Volume Fractions (Burn-off testing)

Burn-off testing was conducted on rebar specimens to measure constituent volume fractions. The average volume fractions and their standard deviations are summarized in Table 4.2. In this table, subscripts *f*, *m*, and *v*, correspond to fiber, matrix, and voids, respectively.

The matrix volume fraction calculated from this method represents the average of the entire sample and is unable to show the distribution of constituents within specific areas of the composite structure. This average value is not necessarily representative of the matrix volume fraction found locally inside the braid or the core. Microstructural analysis showed that the rebar is not a homogeneous composite and the constituent volume fractions in the core and braid should be expected to differ. The burn-off results may also be skewed by the presence of resin drips on the surface of the rebar. These large deposits of matrix can cause the experimental volume fraction of matrix to increase, even though this portion of the composite is not functional to the structure.

Table 4.2: Summary of burn-off test results

	V_f	V_m	V_v
Average Volume Fraction	0.408 ± 0.016	0.493 ± 0.024	0.099 ± 0.010

4.3.4.2 Local Volume Fractions (Image analysis)

Image analysis was used to determine the local fiber and matrix volume fractions in the core and braid regions of the rebar. Sample images of core segmentation are shown in Figure 4.19. Figure 4.19(a) shows the original image, and Figure 4.19(b) shows the segmented image with fibers in green and matrix in red. Average volume fractions of fiber and matrix in the core were 0.465 ± 0.096 and 0.535 ± 0.096 respectively. Sample image of braid segmentation are shown in Figure 4.20. Figure 4.20(a) shows the original image, and Figure 4.20(b) shows the segmented image with fibers in green and matrix in red. Average volume fractions of fiber and matrix in the braid were 0.711 ± 0.029 and 0.289 ± 0.029 respectively.

This method of measuring fiber and matrix volume fractions has several limitations. First, this method operates under the assumption that the images analyzed are representative of the entire composite structure. This is not always the case, but analyzing a large number of images, selected at random locations from various different samples minimizes these effects. Another limitation is that the edges of the structure tend to be under-represented, since the edges can only make up a small portion of each image taken. In the braid, fiber packing was generally less dense near the edges of the structure, and therefore this method may result in a slight underestimation of the total matrix volume fractions. This analysis method is also highly dependent on the quality and contrast of the images, and can be difficult and time consuming to tailor to the particular set of images being analyzed.

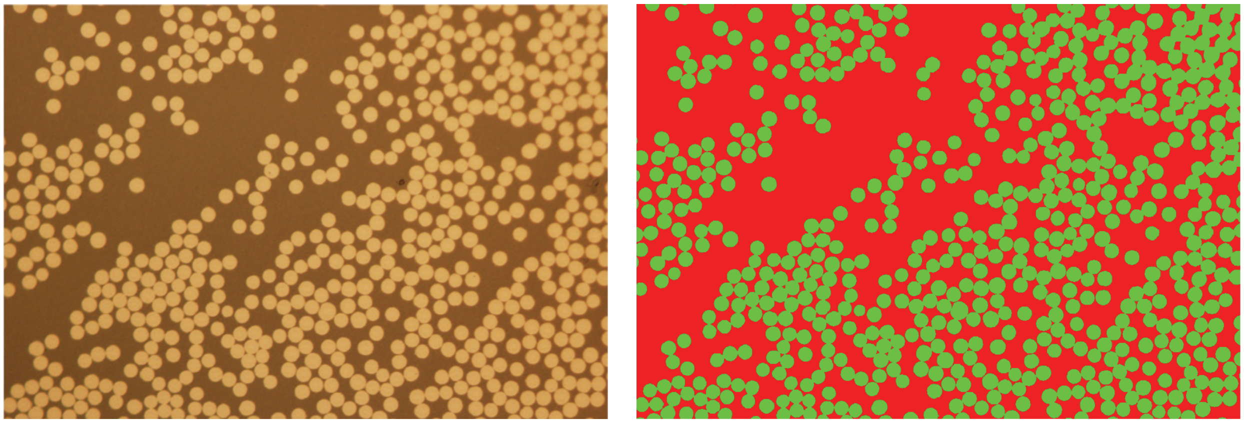
(a) (b)

Figure 4.19: Example of segmentation to determine fiber and matrix volume fractions in core. (a) original image, (b) segmented image

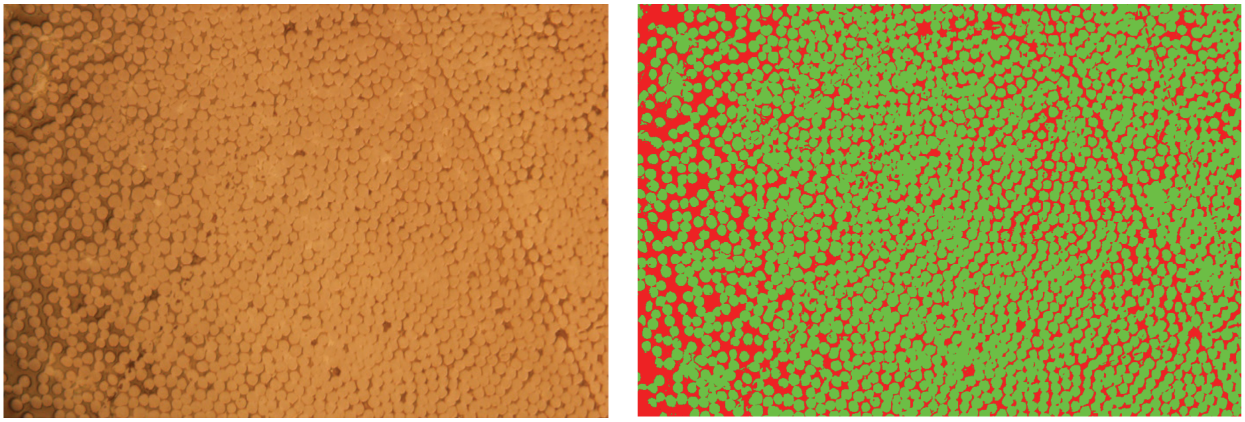
(a) (b)

Figure 4.20: Example of segmentation to determine fiber and matrix volume fractions in braid. (a) original image, (b) segmented image

4.3.5 Comparison of Predicted Structure to Actual Structure

4.3.5.1 Braid Angle

The predicted braid angle, as well as the average and standard deviations of braid angle measured by both measurement methods are shown in Table 4.3. Method 1 was based on the average measured midpoint diameter and average measured helix length, resulting in an average braid angle of 21.7 ± 0.6˚. Method 2 was based on direct measurements from the braid surface and resulted in an average braid angle of 22.5 ± 2.8˚. The predicted braid angle was based on the average measured midpoint diameter, and a helix length found by dividing the puller speed, v_L, by the braiding speed, v_R. The result was a predicted braid angle of 20.7˚.

The result show good agreement between the predicted braid angle, and the measured braid angles from both methods. The midpoint diameter used in method 1 and in the braid angle prediction was the same, meaning that the difference in braid angle is due to differences in measured and predicted helix length. Therefore, helix length measurements may be used as a simple quality control check to ensure the true braid structure being produced is in agreement with the selected pulling and braiding speeds. The average braid angle measured using method 2 showed a greater deviation from the predicted angle. However, the prediction and measurements from method 1 still fell within one standard deviation of the direct angle measurements, which gives confidence that the predicted angle is reasonable.

These results show that Equation 4.1 is adequate to predict braid angle, provided an accurate value for the midpoint diameter is known. A major limitation of this equation is that the midpoint diameter can be difficult to measure, especially in the current case, where the braid is not being formed tightly on a rigid mandrel. When dealing with larger braids that are formed tight to a mandrel, this is less of an issue, as the mandrel diameter can be used as an approximation of the midpoint diameter. In the current case, the thickness of the braid yarns makes up a significant portion of the midpoint diameter, and must be taken into account, as the choice of diameter can have a significant effect on braid angle calculations, For example, in the current rebar the calculated braid angle ranges from 17.1˚ when based on the inner diameter of the braid (4.44 mm), all the way to 24.2˚ when based on the outer diameter (6.45 mm).

Table 4.3: Summary of braid angle measurements and prediction

	Method 1	**Method 2**	**Prediction**
Midpoint Diameter, *D* (mm)	5.45	N/A	5.45
Helix Length, L_h (mm)	43.1 ± 1.2	N/A	45.4
Angle (˚)	21.7 ± 0.6	22.5 ± 2.8	20.7

4.3.5.2 Impregnated Area

The impregnated areas of the core and braid portions of the rebar were measured by image analysis; Figure 4.21 shows an example of one of the rebar cross-sectional images before and after segmentation. The average measured areas (± standard deviation) for the braid, core, interface, and shell, are summarized in Table 4.4. The results for the core, braid, and interfacial areas show good consistency between samples. The shell areas showed greater variation, with the measured area depending on whether or not a resin drip was present at the cross-section location.

The measured impregnated areas were compared to the predicted impregnation areas calculated by Equation 4.2. In this equation, the measured local fiber volume fractions from image analysis for the core ($V_{f,core} = 0.465$) and braid ($V_{f,braid} = 0.711$) were used. The braid angle of 20.7°, as calculated by Equation 4.1 was also used for the area predictions. Equation 4.2 predicted cross-sectional areas of 11.16 mm^2 and 14.83 for the core and braid, respectively. The predictions were in reasonably good agreement with the measured areas. The predicted core area was only 0.7% lower than the average measured value, and the predicted braid area was 14.7% lower than the measured value. This shows that Equation 4.2 adequately predicts the impregnated areas of the composite, especially in the case of the unidirectional core. It should be noted that this equation is limited to calculating the areas of the composite, and is not able to account for the interface or shell areas of the rebar.

The differences between the measured and predicted area of the braid may be due to a number of factors. First, the fiber and matrix volume fractions in the braid were more difficult to measure compared to the core due to inconsistent contrast across the images and exceptionally tight fiber packing. Since Equation 4.2 is highly sensitive to changes in fiber volume fraction, errors in this measurement could have an important effect on the predicted area. Improving image quality and contrast may help to improve the volume fraction measurements and lead to more accurate area predictions. A lower measured fiber volume fraction would result in a predicted cross-sectional area that is closer to that of the measured rebar. In section 3.4.4.2 it was also suggested that the image analysis data for the braid may be slightly overestimating the fiber volume fraction due to an under-representation of the edges of the braid, which may have contributed the difference between predicted and measured results. Another contributing factor could be inaccuracies associated with the braid angle calculation used. It was seen in section 3.4.5.1 that the value of braid angle changes depending on the measurement technique used. A higher braid angle would result in a higher calculated cross-sectional area of the braid, bringing it more in line with the area measured from the rebar cross-sections. Angle measurement was not a factor when calculating the core area, as the core fibers were all oriented along the longitudinal axis.

Table 4.4: Summary of impregnated areas and area fractions of rebar produced using secondary impregnation step

	Braid	Core	Interface	Shell
Predicted Area (mm^2)	14.83	11.16	N/A	N/A
Average Area (mm^2)	17.39 ± 0.88	11.24 ± 0.33	4.23 ± 0.53	6.55 ± 2.25
Average Area Fraction	0.443 ± 0.029	0.286 ± 0.014	0.108 ± 0.013	0.164 ± 0.045

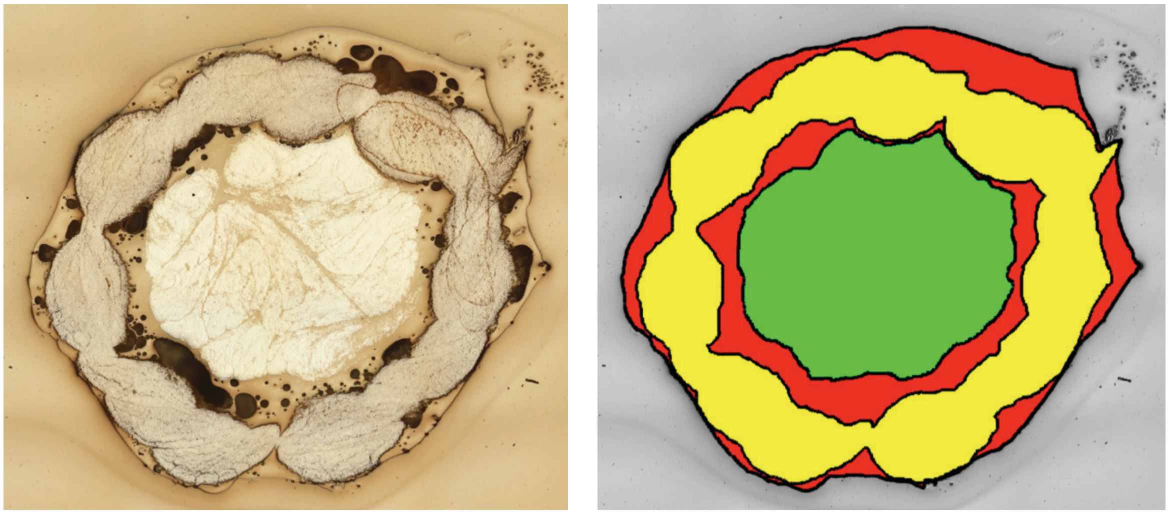
(a) (b)

Figure 4.21 Example of image segmentation to determine impregnated areas. (a) original cross-sectional image, (b) segmented image highlighting shell, braid, interface, and core

4.4 CONCLUSIONS

In this chapter, a new dieless braidtrusion process was introduced for the production of hybrid FRP rebar consisting of a unidirectional core encased in a braided overwrap. The resulting rebar were characterized in terms of their micro and macrostructure, as well as degree of cure. The curing process and cure schedule used in production successfully produced rebar with a high degree of cure, nearing 100%. Optical microscopy and SEM showed good fiber wetting, and a well-bonded interface between the core and braid. Image analysis of the core and braid microstructures revealed an average fiber volume fraction of 0.465 in the core, and 0.711 in the braid. Braid angle was measured using two different methods, and measured angles were relatively consistent with the predicted braid angle of 20.7˚, indicating that the equation used to calculate braid angle was acceptable. Cross-sectional areas occupied by the impregnated core, braid, interface, and surrounding matrix was measured via image analysis. The core and braid areas were compared to analytical equations, which did a relatively good job at predictions these areas. The measured area of the core matched the predicted area with only a 0.7% difference between the two, while the measured area of the braid was 14.7% lower than the analytical prediction. Improving the fiber volume fraction measurements and braid angle measurements may help to improve these results for the braid.

The structural information gained from this study helped to validate equations, which will help to predict the mechanical properties of the FRP rebar. This knowledge is essential to understanding the underlying mechanisms behind mechanical behavior of the rebar, and will lead to further improvements in the manufacturing process and design.

4.5 REFERENCES

[1] Strong, B.A., 2008, "Fundamentals of Composites Manufacturing - Materials, Methods, and Applications (2nd Edition),"Society of Manufacturing Engineers (SME), pp. 453-461, Chap. 18.

[2] Hoa, S.V., 2009, "Principles of the Manufacturing of Composite Materials,"DEStech Publications, pp. 233-245, Chap. 6.

[3] Pastore, C.M., and Ko, F.K., 1999, "Braided Hybrid Composites for Bridge Repair," National Textile Annual Report, F98-P01.

[4] Ewen, K., 2005, "Ductility in FRP Rods for Concrete Reinforcement by Interfacial Shearing," University of Ottawa. Canada.

[5] Hampton, F., 2004, "Cyclic Behavior, Development, and Characteristics of a Ductile Hybrid Fiber Reinforced Polymer (DHFRP) for Reinforced Concrete Members," Drexel University. United States.

[6] Harris, H. G., Somboonsong, W., and Ko, F. K., 1998, "New Ductile Hybrid FRP Reinforcing Bar for Concrete Structures," Journal of Composites for Construction, **2**pp. 28-37.

[7] Somboonsong, W., Ko, F. K., and Harris, H. G., 1998, "Ductile Hybrid Fiber Reinforced Plastic Reinforcing Bar for Composite Structures: Design Methodology," ACI Materials Journal, **95**(6) pp. 655-666.

[8] Fangueiro, R., Sousa, G., Soutinho, F., 2006, "Application of Braided Fibre Reinforced Composite Rods in Concrete Reinforcement," Materials Science Forum, **514-516**pp. 1556-1560.

[9] You, Y., Park, Y., Park, J., 2007, "Development of FRP rebar for concrete structures in Korea," FRPRCS-8, pp.1-8.

[10] You, Y., Kim, J., Kim, S., 2015, "Methods to Enhance the Guaranteed Tensile Strength of GFRP Rebar to 900 MPa with General Fiber Volume Fraction," Construction and Building Materials, **75**pp. 54-62.

[11] Hamada, H., Kameo, K., Sakaguchi, M., 2000, "Energy-Absorption Properties of Braided Composite Rods," Composites Science and Technology, **60**pp. 723-729.

[12] Ahmadi, M. S., Johari, M. S., Sadighi, M., 2009, "An Experimental Study on Mechanical Properties of GFRP Braid-Pultruded Composite Rods," Express Polymer Letters, **3**(9) pp. 560-568.

[13] Pastore, C., Armstrong-Carroll, E., and Ko, F., 2012, "Effect of Yarn Size on the Performance of Hybrid Braided Composite Rebar," The Masterbuilder, pp. 234-244.

[14] Ko, F., Head, A., and Pastore, C., 1989, "Handbook of Industrial Braiding," Atkins and Pearce, Covington, Kentucky.

[15] Du, G., and Popper, P., 1994, "Analysis of a Circular Braiding Process for Complex Shapes," The Journal of the Textile Institute, **85**(3) pp. 316-337.

[16] Alpyildiz, T., 2012, "3D Geometrical Modeling of Tubular Braids," Textile Research Journal, **82**(5) pp. 443-453.

[17] Mutlur, S., 2004, "Advanced Topics in Characterization of Composites,"Trafford Publishing, pp. 11-33.

[18] Sichina, W.J., 2000, "Characterization of epoxy resins using DSC," PerkinElmer Instruments.

[19] TA Instruments, "Characterization of the degree of cure of thermosetting resins by DSC," TA Instruments.

[20] Hoa, S.V., 2009, "Principles of the Manufacturing of Composite Materials,"DEStech Publications, pp. 45-98, Chap. 2.

[21] ASTM International, 2011, "ASTM D3171 - 11 Standard Test Method for Constituent Content of Composite Materials," pp. 1-11.

[22] Toho Tenax America, I., 2014, "Safety Data Sheet SDS no. 0503 Rev L".

[23] DuPont, "Technical Guide: Kevlar Aramid Fiber".

[24] Xiong, G., 2006, "Local Adaptive Thresholding".

[25] Ko, F.K., 2001, "ASM Handbook, Volume 21: Composites,"ASM International, pp. 70-77, Chap. Braiding.

[26] Lebel, L. L., and Nakai, A., 2012, "Design and Manufacturing of an L-Shaped Thermoplastic Composite Beam by Braid-Trusion," Composites: Part A, **43**pp. 1717-1729.

5 MODELING AND MECHANICAL CHARACTERIZATION OF TENSILE PROPERTIES

5.1 INTRODUCTION

Early work on the failure mechanisms in hybrid composite laminates was conducted by Aveston and Kelly [1]. They found that, for a hybrid composite consisting of a low strain component and a high strain component, multiple fractures can take place in the composite, leading to progressive failure and a pseudoductile response. For this to occur, the composite must contain a minimum fraction of the high strain component, as described in Chapter 3. If this minimum requirement is not met, the hybrid composite fails catastrophically when the low strain component reaches its ultimate strain. Bunsell and Harris [2] also studied the effects of material hybridization in glass-carbon laminates. They found that failure began with the fracture of the carbon plies around the failure strain of the carbon fibers, and final failure occurred when the glass plies fractured at their failure strain. Failure behavior was dependent on the interlaminar bond properties. For poor bonding, a large load drop was observed at the initial failure, followed by linear elastic loading of the glass plies until final failure. When the bonding between plies was strong, a "saw-tooth" pattern was observed, with many smaller load drops and reloading steps starting at the ultimate strain of the carbon plies until ultimate failure. In more recent years, researchers have applied these concepts towards composite rods [3, 4] with similar results.

Most attempts at modeling pseudoductile hybrid FRP bars have assumed that behavior is similar to the case described by Bunsell and Harris [2] where a large load drop is observed at initial failure, followed by a linear reloading of the low-strain component [3-5]. In general, analytical models have done a good job of predicting the initial elastic modulus of the hybrid composite, but have struggled to accurately predict the rebar behavior after the initial failure point. In previous studies looking at hybrid braided FRP rebar similar to those in this thesis, models often over-predict the ultimate strains of the rebar [3, 4, 6] and little explanation has been provided to explain the variations between experimental and predicted results.

The ability to understand the failure mechanism of the FRP rebar and accurately predict the mechanical properties is important to enable the rebar to be scaled to different sizes and tailored for different applications and material systems. In this chapter, a model is presented to predict the mechanical properties of the rebar according to the proposed failure mechanism for this type of hybrid composite. Mechanical testing is conducted and the results are compared to the model predictions. The validity of the failure mechanism is evaluated and modifications are made to the model in order to better represent the true properties of the rebar.

5.2 EXPECTED FAILURE MECHANISM

As previously discussed, hybrid FRP rebar was manufactured by a dieless braidtrusion process, combining aspects of pultrusion and braiding to enable the continuous production of rebar consisting of a unidirectional core, encased in a braided overwrap, as shown schematically in Figure 5.1. Because no die was used in the manufacturing process, the cross-sectional shape of the rebar was dictated by the natural shape of the braid [3], and consisted of an approximately circular cross-section with an undulating surface. The braid was manufactured in the jammed state, meaning that the braid is in its tightest possible configuration, with a cover factor of 1.0 [7, 8]. Table 5.1 summarizes the important manufacturing parameters used for the rebar production. 12 core yarns and 18 braid yarns were used to form the structure. The puller operated at a speed of 77.2 mm/min and the braider was run at a speed of 1.70 RPM. This resulted in the production of rebar with a nominal outer diameter of 6.45 mm, and a braid angle of approximately 20.7˚. Since they were pultruded, the core yarns were oriented at 0˚ to the axial direction of the rebar.

(a) (b)

Figure 5.1: Schematic of rebar produced by dieless braidtrusion, (a) cross-section, (b) side view, where carbon core is shown in black, and aramid braid is shown in yellow

Table 5.1: Summary of important manufacturing parameters

Parameter	Value
Number of core yarns, N_{core}	12
Number of braid yarns, N_{braid}	18
Pulling speed, v_L,	77.2 mm/min
Braiding speed, v_R	1.70 RPM
Braid angle, θ	20.7°

By combining different fiber types and fiber orientations, the rebar design takes advantage of material and structural hybridization to achieve a multi-stage, pseudoductile failure. Figure 5.2 presents the proposed failure mechanism for the rebar under uniaxial tensile loading. This mechanism was based on the assumption of constant strain between the core and braid structures, and that failure was limited by the maximum strain criteria. This approach has been used to describe the tensile behavior of hybrid FRP laminates and bars in the past [1-5]. Initially (Figure 5.2(a)), the load is shared between the core and the braid, with the 0° fibers in the core providing high stiffness to the composite structure. When the failure strain of the core fibers is reached, the entire core fails instantly (Figure 5.2(b)). In the context of hybrid composites, this initial failure is sometimes referred to as "yielding" [3-6], as it is the point where the composite strays from its initial linear elastic properties. After yielding, the load is picked up by the braid and the rebar continues to be strained (Figure 5.2(c)). The failure strain of the braid yarns is higher than that of the core, allowing for additional elongation of the rebar. Once the failure strain of the braid fibers is reached, the braid will fail at the same location as yielding occurred, causing final fracture of the rebar (Figure 5.2(d)).

Figure 5.2: Schematic of proposed failure mechanism. (a) Initial loading of complete rebar structure, (b) fracture of core yarns at ultimate strain of carbon fibers, (c) continued loading of rebar, load is picked up by intact braid, (d) fracture of braid yarns at ultimate strain of the aramid fibers.

5.3 MODEL DESCRIPTION

An analytical model was developed to predict the stress-strain behavior of the rebar under uniaxial tension. Implementation of the model was done using code written in MATLAB®, which can be found in Appendix F. To calculate elastic properties, the rebar was modeled as a laminated composite, as shown schematically in Figure 5.3. A balanced, symmetric stacking sequence of $[\pm\theta/0]_S$ was used, where θ is the braid angle, and the 0° ply is used for the core. Both $+\theta$ and $-\theta$ lamina were used to represent the braid, accounting for warp and weft yarns. This approach was chosen in order to limit the model complexity as a first step in predicting the elastic properties of the rebar

Figure 5.3: Schematic of laminated composite used to model rebar properties

The model also relies on the following assumptions. First, the model assumes that strain is uniform over the entire gage length of the bar, meaning that the average strain in the bar is the same as local strain at any given point. Other attempts to model similar composite rebar have relied on this assumption to reasonable success [3-5]. Strain is assumed to be constant between plies, and failure is limited by the maximum fiber strain. The model also assumes perfect bonding between fibers and matrix. Though the proposed failure mechanism implies that there are changes in effective cross-section that carries the load after yielding, a constant cross-section was used when calculating elastic properties of the rebar. This approach is analogous to using the original specimen cross-section to calculate engineering stress in a ductile material despite the changing cross-section due to necking of the material.

A schematic of the expected stress-strain behavior of the rebar is shown in Figure 5.4. This curve shows a bilinear failure that can be broken down into four steps, corresponding to those shown in the proposed failure mechanism in Figure 5.2. Part A of the curve shows the initial loading of the rebar with a high elastic modulus combining the core and braid properties. At point B, the core fibers fail at their ultimate strain, and a load drop occurs. This drop is a result of a sudden decrease in elastic modulus of the rebar due to failure of the core. The stress then increases in part C as the braid picks up the load. The elastic modulus is lower in this region, and is dominated by the properties of the braid, as the core stiffness is discounted after yielding. Final failure occurs at point D, when the failure strain of the braid yarns is reached.

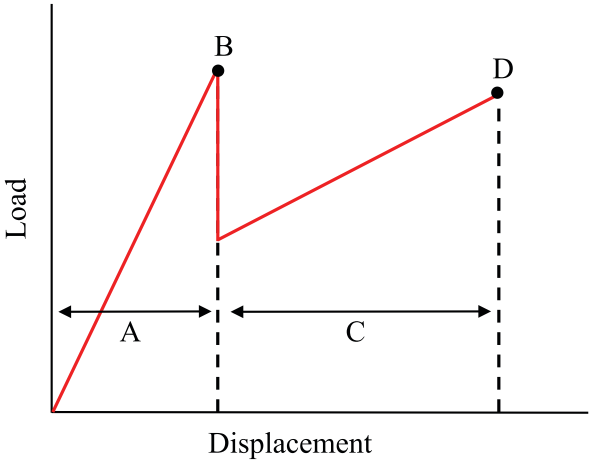

Figure 5.4: Example of predicted stress-strain curve for pseudoductile FRP rebar

Figure 5.5 shows a flowchart of the steps needed for the model to calculate the predicted stress-strain behavior of the composite. Each step of the process is explained in detail in this section. The first step is to define the required input parameters. These include braid angle, fiber volume fraction in the core, $V_{f,c}$, and in the braid, $V_{f,b}$, as well as material properties of the fibers and matrix. For the current rebar design, $V_{f,c}$ and $V_{f,b}$ are 0.465 and 0.711 respectively. These properties and parameters are all that is needed to calculate the predicted stress-strain response of the rebar.

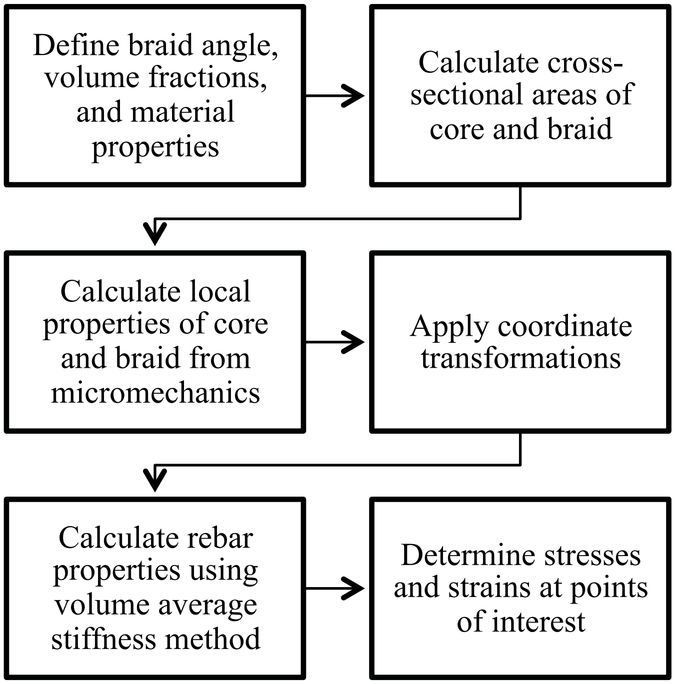

Figure 5.5: Flowchart of analytical model

The next step is to determine the cross-sectional area occupied by the impregnated core and braid portions of the rebar. This area includes both the fibers and matrix that make up the cured composite structure, and is calculated by finding the cross-sectional area taken up by the fibers and then adjusting for the fiber volume fraction. Equation 3.1 is used to calculate the specific area, A_{sp}, taken up by the fibers in the core or braid [3]. In this equation, N is the number of yarns, *den* is the linear density of the yarns in denier, ρ is the density of the fibers in g/cm^3, and θ is the braid angle. In the core, θ is equal to 0, since the fibers are all axially oriented. This equation assumes that the fibers have a circular cross-section, and calculates area based on the elliptical fiber cross-sections created by cutting through fibers at the specified angle. Since A_{sp}

gives only the specific area of the fibers, it must be divided by the fiber volume fraction, V_f to find the impregnated cross-sectional area, A, as shown by Equation 5.2. The total cross-sectional area of the composite is then equal to the sum of impregnated areas of the core and braid.

$$A_{sp} = \frac{N \cdot den}{9000\rho \cos\theta} \qquad [5.1]$$

$$A = \frac{Area_{sp}}{V_f} = \frac{N \cdot den}{V_f 9000\rho \cos\theta} \qquad [5.2]$$

The composite properties are then calculated from micromechanics, for each lamina representing the braid and core structures; here, Halpin-Tsai equations were used [9], providing values for elastic modulus, *E*, shear modulus, *G*, and Poisson's ration, *υ*, in the local coordinates (1-2-3 coordinate system) for each lamina. In the local coordinate system, the 1-direction is oriented with the fibers, the 2-direction is perpendicular to the fibers, and the 3-direction is normal to the lamina. The global coordinate system (x-y-z) is oriented such that the x-direction is the axial direction of the rebar. Therefore, for the lamina representing the braid yarns, the local and global coordinate systems differ by the braid angle, *θ*, as shown schematically in Figure 5.6. For the core yarns, the local and global coordinates are identical due to the 0˚ orientation.

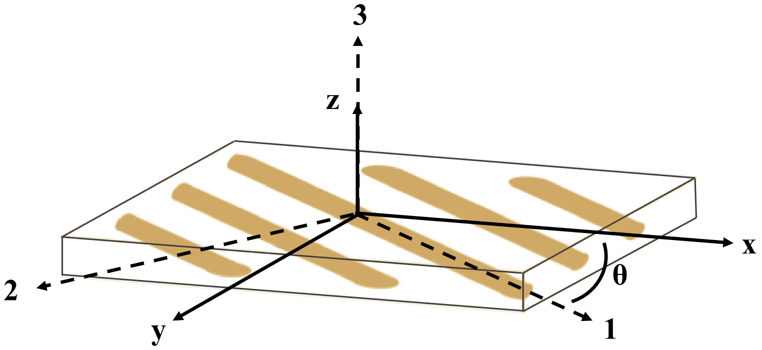

Figure 5.6: Schematic of local and global coordinate systems

Once the local elastic properties have been found for the braid and core laminae, the compliance and stiffness matrices are determined for each lamina in local coordinates, and adjusted to global coordinates, based on θ. Treating each individual lamina as a transversely isotropic material, the local compliance matrix for a particular lamina can be determined following Equation 5.3 [10, 11]. The compliance matrix, [S] is then transformed into the global coordinate system using the transformation matrix, [T], shown in Equation 5.4 [10]. The transformation is achieved by Equation 5.5, where [S'] is the new compliance matrix in global coordinates. Taking the inverse of the global compliance matrix gives the global stiffness matrix, [C'], as shown in Equation 5.6.

$$[S] = \begin{bmatrix} \frac{1}{E_1} & -\frac{v_{12}}{E_1} & -\frac{v_{13}}{E_1} & 0 & 0 & 0 \\ -\frac{v_{21}}{E_2} & \frac{1}{E_2} & -\frac{v_{23}}{E_2} & 0 & 0 & 0 \\ -\frac{v_{31}}{E_3} & -\frac{v_{32}}{E_3} & \frac{1}{E_3} & 0 & 0 & 0 \\ 0 & 0 & 0 & \frac{1}{G_{23}} & 0 & 0 \\ 0 & 0 & 0 & 0 & \frac{1}{G_{31}} & 0 \\ 0 & 0 & 0 & 0 & 0 & \frac{1}{G_{12}} \end{bmatrix} \qquad [5.3]$$

$$[T] = \begin{bmatrix} \cos^2\theta & \sin^2\theta & 0 & 0 & 0 & 2\sin\theta\cos\theta \\ \sin^2\theta & \cos^2\theta & 0 & 0 & 0 & -2\sin\theta\cos\theta \\ 0 & 0 & 1 & 0 & 0 & 0 \\ 0 & 0 & 0 & \cos\theta & -\sin\theta & 0 \\ 0 & 0 & 0 & \sin\theta & \cos\theta & 0 \\ -\sin\theta\cos\theta & \sin\theta\cos\theta & 0 & 0 & 0 & \cos^2\theta - \sin^2\theta \end{bmatrix} \qquad [5.4]$$

$$[S'] = [T]^T[S][T] \qquad [5.5]$$

$$[C'] = [S']^{-1} \qquad [5.6]$$

Once the global stiffness matrices have been found for the core and braid, the overall composite stiffness can be determined using the volume average stiffness method [10, 12]. This method relies on the assumption of constant strain between the laminae, and combines the stiffness of each lamina based on their volume fractions of the overall composite. To do this, the volume fractions of the core and braid structures are first found using Equation 5.7, where subscripts b and c correspond to braid and core, respectively. This equation assumes a constant cross-section of the rebar, which allows the volume fractions, V_b and V_c, to be calculated based on their impregnated cross-sectional areas. The stiffness matrix is then computed for the rebar before yielding, $[C_{comp}]_1$, and after yielding, $[C_{comp}]_2$, following Equations 5.8 and 5.9 respectively. $[C'_{\theta+}]_b$, $[C'_{\theta-}]_b$, and $[C'_{0^\circ}]_c$ correspond to the global stiffness matrices for the $+\theta$ braid lamina, the $-\theta$ braid lamina, and the 0° core lamina respectively. Equations 5.8 and 5.9 are identical, except that for after yielding, the contribution of the core stiffness is fully discounted to zero.

$$V_b = \frac{A_b}{A_b + A_c} \;, \qquad V_c = \frac{A_c}{A_b + A_c} \qquad [5.7]$$

$$[C_{comp}]_1 = \frac{A_b}{2}[C'_{\theta+}]_b + \frac{A_b}{2}[C'_{\theta-}]_b + A_c[C'_{0^\circ}]_c \qquad [5.8]$$

$$[C_{comp}]_2 = \frac{A_b}{2}[C'_{\theta+}]_b + \frac{A_b}{2}[C'_{\theta-}]_b + 0[C'_{0^\circ}]_c \qquad [5.9]$$

Taking the inverse of $[C_{comp}]_1$ and $[C_{comp}]_2$ gives the compliance matrices before and after yielding, as shown in Equation 5.10. Finally, the longitudinal elastic modulus of the rebar before yielding, $E_{x,1}$, and after yielding, $E_{x,2}$, can be extracted from $[S_{comp}]_1$ and $[S_{comp}]_2$, as shown in Equation 5.11. In this equation, the subscript 1,1 corresponds to the matrix element located in the first row and first column.

$$[S_{comp}]_1 = [C_{comp}]_1{}^{-1} \;, \qquad [S_{comp}]_2 = [C_{comp}]_2{}^{-1} \qquad [5.10]$$

$$E_{x,1} = \frac{1}{[S_{comp}]_{1_{1,1}}} \;, \qquad E_{x,2} = \frac{1}{[S_{comp}]_{2_{1,1}}} \qquad [5.11]$$

In the current model, the failure behavior of the rebar is assumed to be strain limited. Yielding occurs when the failure strain of the core fibers, $\varepsilon_{c,f}$, is reached, and ultimate failure occurs when the failure strain of the braid fibers, $\varepsilon_{b,f}$, is reached, as summarized in Equation 5.12. For the current core and braid materials, $\varepsilon_{c,f}$ is 0.099 mm/mm and $\varepsilon_{b,f}$ is 0.024 mm/mm. The stresses in the rebar can then be calculated for yielding and failure based on the pre and post yielding elastic modulus values and limiting strain values, as shown in Equations 5.13, 5.14, and 5.15. The yield stress, σ_y, is the stress at which the core fails, the dropped stress, σ_d, is the stress in the bar when the load is transferred to the braid immediately after yielding, and the ultimate stress, σ_{ult}, is the stress at which final failure of the braid occurs. These values can be used to plot stress versus strain for the rebar, which can be compared to experimental data to validate the model.

$$\varepsilon_y = \varepsilon_{c,f} \ , \qquad \varepsilon_{ult} = \varepsilon_{b,f} \tag{5.12}$$

$$\sigma_y = E_{x1}\varepsilon_y \tag{5.13}$$

$$\sigma_d = E_{x2}\varepsilon_y \tag{5.14}$$

$$\sigma_{ult} = E_{x2}\varepsilon_{ult} \tag{5.15}$$

5.4 MATERIALS & METHODS

5.4.1 Tensile Testing

Tensile testing was conducted on the FRP rebar using a uniaxial mechanical testing system (Instron, USA), equipped with a 44.4 kN (10000 lbf) load cell. Rebar specimens cut to lengths of 600 mm were potted in custom end tabs, and threaded into custom adapters that allowed the specimens to be attached to the test frame. Figure 5.7(a) shows an example of a rebar specimen mounted for tensile testing. To measure strain of the rebar, an extensometer (Model 63431E-24, MTS Systems USA) was mounted on the test specimen, near the center of the rebar gage length, as shown in Figure 5.7(b). The presence of undulations on the braided surface of the rebar made mounting of the extensometer relatively easy and secure. The gage length of the extensometer was 12.7 mm (0.5 in). The extensometer was removed prior to failure of the rebar core, in order to avoid damaging the instrument. Load, strain, and crosshead displacement was recorded at a rate of 10 samples per second. All tests were conducted to failure at a constant displacement rate of 1.27 mm/min (0.05 in/min).

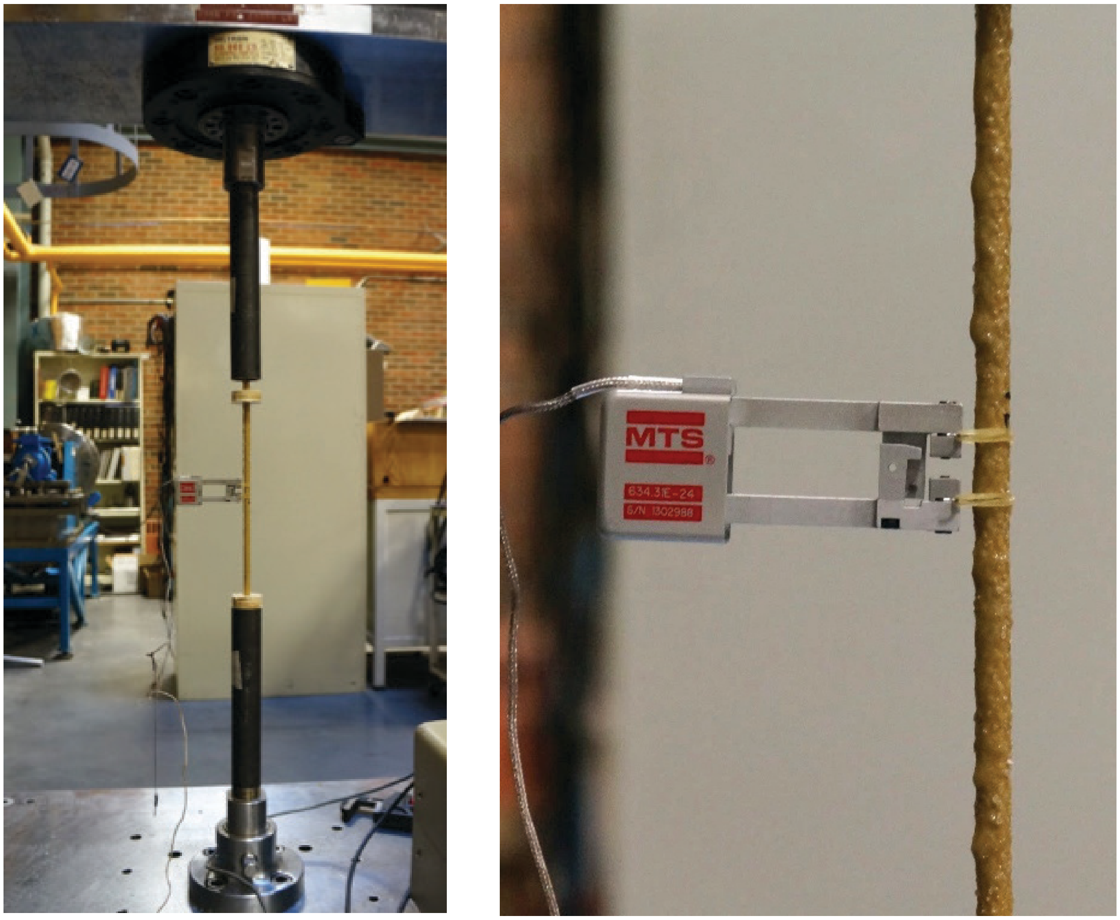

(a) (b)

Figure 5.7: (a) Tensile testing setup, (b) extensometer fixed to rebar for strain measurement

5.4.2 End Tab Development

In order to effectively grip the rebar for tensile testing, custom end tabs were developed based on ASTM D7205 [13] and ACI 440.3R-04 [14] recommendations, as well as previous studies by Hampton [3] and Elzafraney [15]. Figure 5.8 shows a schematic drawing of the rebar mounted in the end tabs. Rebar specimens were potted in threaded steel tubes filled with high strength epoxy resin (Sikadur® 35 Hi-Mod LV, Sika, Canada) [16]. The steel tubes measured 9 inches (228.6 mm) in length with a 1 inch (25.4 mm) inner diameter. The inside surface of the steel tubes was threaded in order to enhance bonding between the potting resin and the tube via mechanical keying. The rebar was potted to a depth of 175 mm in each end tab, leaving a gage length of 250 mm in the center. A long gage length is important to minimize the chance of a failure occurring at the interface between the potting resin and rebar due to stress concentrations. It was important that the rebar be potted as straight as possible to ensure that only axial loading was being applied to the rebar during tensile testing. To achieve this, alignment washers were made in the form of wooden caps with holes drilled in the center; washers were positioned on the ends of the steel tubes. The rebar passed through the alignment washers and proper alignment was achieved by clamping the entire assembly down to steel angles, as shown in Figure 5.9. The clamped assembly was positioned vertically and one tube was filled with resin and allowed 4 hours to set, before flipping the assembly upside down and filling the other tube. The potting resin was then allowed 7 days to cure at room temperature (23 ˚C) to achieve maximum strength prior to tensile testing.

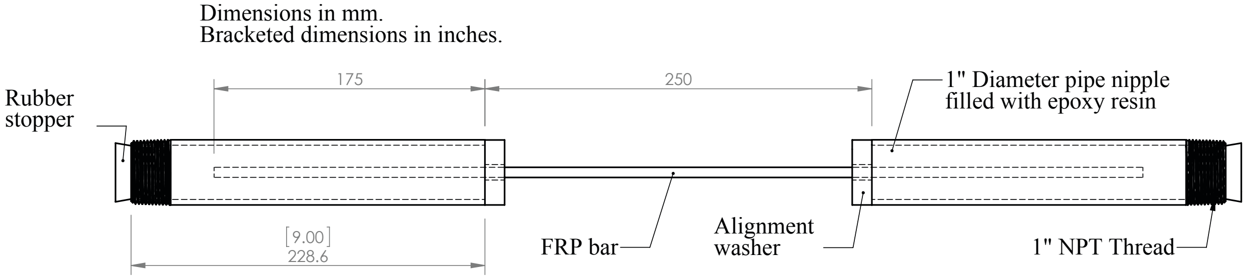

Figure 5.8: Schematic of potting setup for rebar tensile test specimens

Figure 5.9:Potted rebar specimen clamped to steel angle to ensure straightness and alignment

5.4.3 Optical Strain Measurement

For three of the tensile test specimens, an in-house optical strain measurement (OSM) program written in MATLAB® was used for strain measurement in addition to the physical extensometer. The OSM code was based on previous work by Frank [17]. OSM allowed for strain to be measured over the entire duration of the test, as opposed to the physical extensometer, which had to be removed prior to yielding. This allowed for the strain behavior of the rebar during and after yielding to be examined. Contrast marks were painted onto the rebar surface, 1 inch apart, using black acrylic paint, as shown in Figure 5.10. The distance between these contrast marks was monitored as testing progressed in order to calculate strain in the rebar.

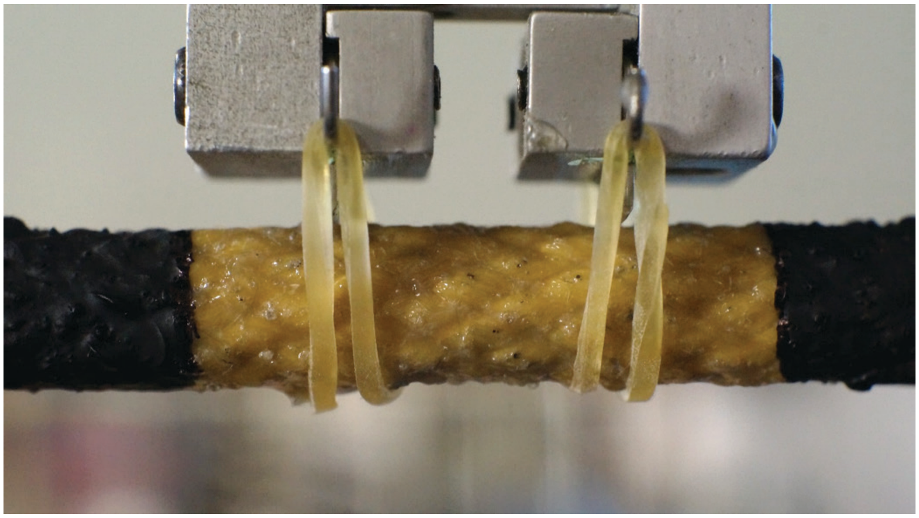

Figure 5.10: Frame captured by camera for OSM showing contrast marks painted on sample, along with physical extensometer attached to gage length

Video of the tensile test was recorded using a DSLR camera (Sony NEX-5R, Sony USA) at a rate of 10 frames per second and a resolution of 1920 x 1080 pixels. Each frame of the video was converted into an image and analyzed sequentially to obtain strain measurement results. Figure 5.11 outlines the OSM analysis steps for a single image. The initial grayscale image of the rebar is shown in Figure 5.11(a). Contrast between the black marks and the rebar surface was reasonably good, but was improved by image processing. The contrast of the image was enhanced by mapping low intensity pixels to black, and mid to high intensity pixels to white, resulting in Figure 5.11(b). A bounding box was then defined (Figure 5.11(c)) for the image in order to limit the boundaries inside of which the strain measurements were performed. The same bounding box is used for the entire image stack. For each column of pixels in the bounding box, an average pixel intensity value was computed. An intensity of zero corresponded to a black pixel, and an intensity of 1 corresponded to a white pixel, with grayscale values falling in between. The intensity values were plotted and a curve was fit to the data using two error functions, as shown in Figure 5.11(d). A large jump in intensity at the contrast marks, and the distance in pixels between the midpoint of these intensity jumps was measured. The pixel distance measured for each frame is compared to the original distance between contrast marks to compute strain in units of pixels/pixel. To verify the validity of the OSM data, physical extensometer data was also recorded for these tests, at the same location as the optical measurements were conducted.

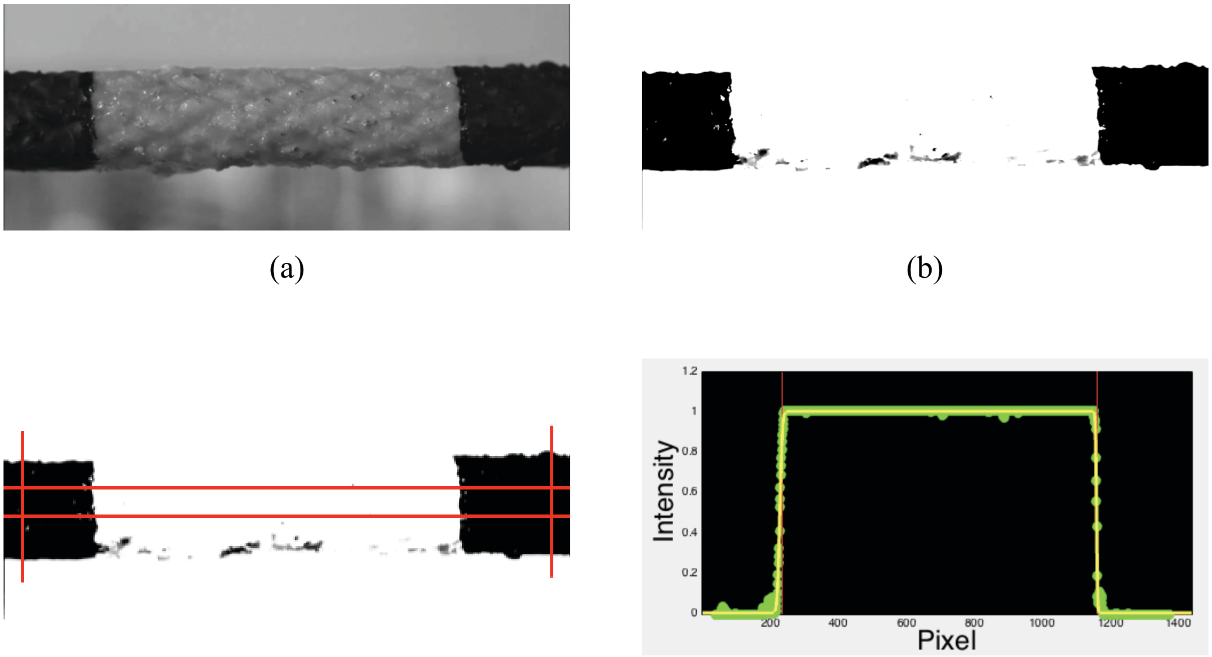

(a) (b)

(c) (d)

Figure 5.11: Sample analysis steps for a single frame using the OSM method. (a) Grayscale image of rebar, (b) enhanced image contrast to accentuate black markings, (c) bounding box to specify analysis region, (d) plot of average pixel intensity along the length of the bounding box

5.5 RESULTS AND DISCUSSION

5.5.1 Tensile Testing Results

Ten rebar specimens were prepared for tensile testing to failure, with seven specimens providing useable results. The seven successful samples experienced final failure ranging from the center of the rebar gage length to near the end tabs. None of the failure occurred directly at the boundary between potted and un-potted rebar, indicating that the test setup reasonably minimized the edge effects of the end tabs. Figure 5.12 shows a plot of load versus displacement for the specimens tested. All specimens showed a similar tensile response, consisting of an initial linear elastic load increase, followed by a load drop, then another increase until final failure of the rebar. This type of failure was consistent with the proposed failure mechanism, and is characteristic of other similar hybrid composite materials [2, 18, 19]. Yielding occurred at an average load (± standard deviation) of 20.3 ± 0.7 kN, and displacement of 3.64 ± 0.11 mm. The load then dropped by an average of 50.0 % to a value of 10.1 ± 1.0 kN before reloading to an average of 87.6 % of the yielding load, resulting in an average ultimate failure load of 17.8 ± 0.7 kN at an average final displacement of 6.39 ± 0.81 mm.

As expected, yielding was characterized by a large load drop corresponded to brittle failure of the unidirectional carbon fiber core. At this yield point, the outer surface of the rebar showed no obvious signs of damage. During the initial linear elastic portion of the loading, some of the samples showed small load drops prior to the full core failure. These drops were a result of small groups of carbon fibers failing prematurely due to uneven tension or slight misalignment of the fibers [3], and may be completely eliminated by further refinement of the manufacturing process. However, these load drops were relatively small and infrequent compared to previous studies [3-5], meaning that overall, the core was well tensioned and well aligned. After the initial failure, the slope of the load-displacement curve decreased, relative to the initial loading step. This was as expected, since the contribution of the unidirectional carbon core to the stiffness of the composite is compromised when the core fractures. However, a slight non-linearity was observed during the reloading of the rebar after yielding. Similar non-linear responses during reloading were observed be Pastore [5], and were attributed to reorientation of the braid structure. In this case, however, because the braid is in the jammed state, significant reorientation is not expected to occur. This may indicate that the fractured core continues to contribute to the rebar stiffness immediately following yielding. This remaining stiffness contribution by the core decreases as the rebar continues to be strained until the slope becomes linear, at which point the stiffness is dominated by the braid and the core can be fully discounted.

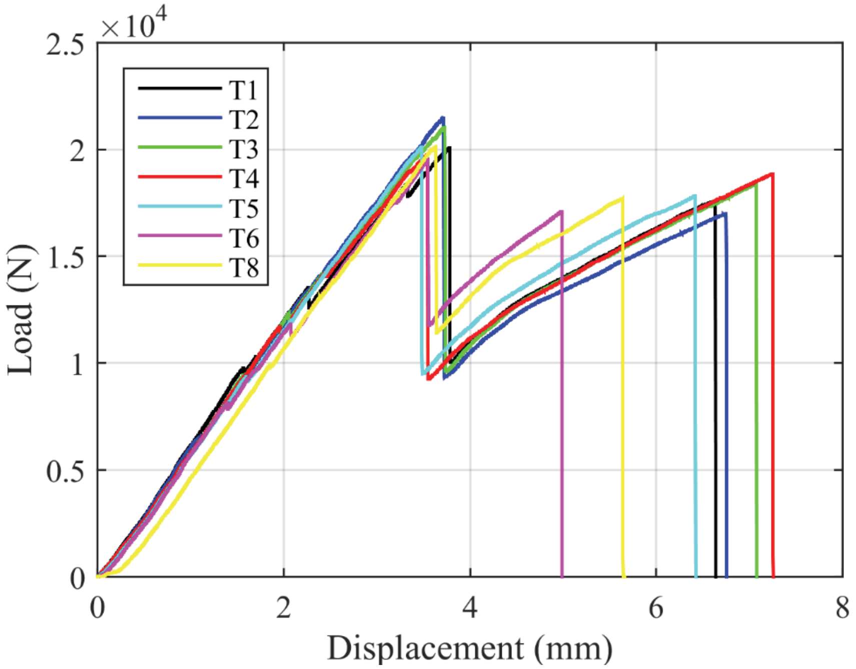

Figure 5.12: Plot of load vs displacement for different rebar specimens

Figure 5.13 shows representative images of one of the failed rebar specimens. As shown in Figure 5.13(a), the failure occurred near the middle of the rebar gage length, away from the end tabs. A close-up of the failure site is shown in Figure 5.13(b). Immediately after ultimate failure of the rebar occurred, the crosshead was stopped and this picture was taken. In this photo, the braid has been pulled back to reveal the failed carbon fiber core. A significant gap is observed between the two ends of the failed core, corresponding to the additional elongation of the rebar achieved during the reloading of the braid after yielding. This additional displacement represents the pseudoductile aspect of the hybrid composite, as it allows for final elongation of the rebar that is nearly double the elongation at yielding.

Figure 5.14(a) provides an even closer view of the failure location, and reveals that yielding resulted in a clean break straight through the core, transverse to the loading direction, with a relatively flat failure surface. This is indicative of even tension and good axial alignment of the carbon fibers in the core [3]. The failed braid yarns appeared relatively dry; this appearance was similar to other aramid fiber composites failing in tension [3]. This is in part a result of the high fiber volume fraction and in the braid, but may also be due to the matrix material simply crumbling away during ultimate failure. A close-up picture of the braid surface near the failure site can be seen in Figure 5.14(b). This image shows matrix cracking brought on by the shock of the final tensile failure of the braid.

(a) (b)

Figure 5.13: (a) Failed tensile test specimen, (b) close-up of failure location, showing gap between fractured ends of carbon core as a result of additional elongation post-yielding

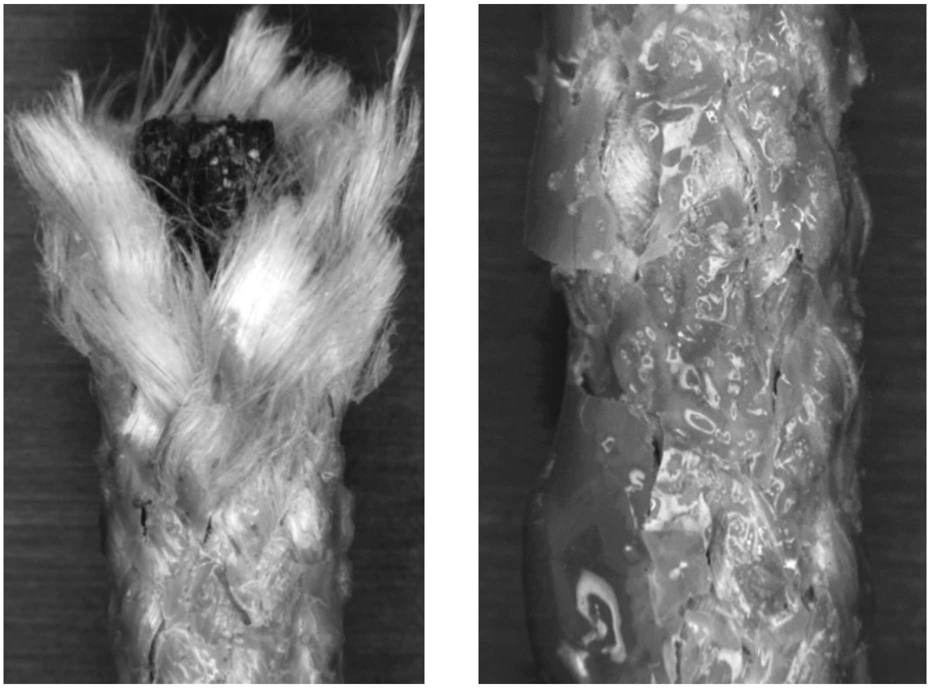
(a) (b)

Figure 5.14: (a) Closeup of failure site, showing clean fracture of core and relatively dry braid yarns after failure, (b) close-up of rebar surface near failure site showing extensive matrix cracking

5.5.2 Stress-Strain Behavior and Comparison to Model Predictions

The tensile test data can be expressed in terms of stress and strain for comparison to the predictive model. The calculated cross-sectional area of the braid and core were combined for a total rebar cross-sectional area of 25.99 mm^2. Dividing the load by this area gives the stress in the rebar. The strain measured by the extensometer attached to the bar was used to determine the elastic modulus of the composite for the linear elastic portion of the curve prior to yielding. Stress-strain data was plotted and a linear regression was used to find the elastic modulus for each specimen, resulting in an average elastic modulus (± standard deviation) of 84.2 ± 7.5 GPa.

Since the extensometer was removed prior to the initial failure in the bar, strain was not measured directly during the load drop and subsequent reloading of the bar. The average strain in the rebar after yielding was estimated by dividing the crosshead displacement by the gage length of the rebar. This estimated strain was consistently higher than the strain recorded by the extensometer, due to the compliance of the end tabs and fixtures. In order to account for the compliance, a correction factor was applied to the estimated strain. The correction factor was chosen such that the rebar elastic modulus from the corrected strain data was identical to the elastic modulus previously found using extensometer strain. This corrected strain was used to plot the following stress-strain results.

Figure 5.15 shows the resulting stress-strain curves for the rebar samples compared to the results from the analytical model. The model predictions and experimental results (average ± standard deviation) are compared in Table 5.2, and were found to be in relatively good agreement. The initial elastic modulus predicted by the model was within one standard deviation of the average measured modulus. Though after yielding, the experimental results showed a region of non-linear elastic behavior, the slope eventually stabilized to 36.3 ± 7.4 GPa, which was in line with the modulus predicted by the model.

The predicted yield stress was an average of 13.8 % higher than the average measured value. This difference can be largely attributed to the small load drops due to premature failure of individual fiber bundles observed during the initial loading of the rebar. These small drops take away from the maximum stress that can be theoretically achieved [3]. The drop in stress at yielding was reasonably well captured by the model, although experimental results showed less of a drop, indicating that fully discounting the core stiffness at yielding may be overly conservative.

The predicted and observed yield strains were in excellent agreement, verifying the assumption that yielding was limited by the failure strain of the core fibers. However, the average ultimate strain of the rebar was observed to be 0.0164 ± 0.0027 mm/mm, which was well below the predicted strain of 0.024 mm/mm. Similar results over-predicting the failure strain of hybrid FRP rebar have been observed in previous work by Hampton [3], Somboonsong [4], and Pastore [5], and were attributed to poor impregnation quality or manufacturing defects, however, this hypothesis was not been thoroughly investigated. The possible cause of this discrepancy is explored in the following section.

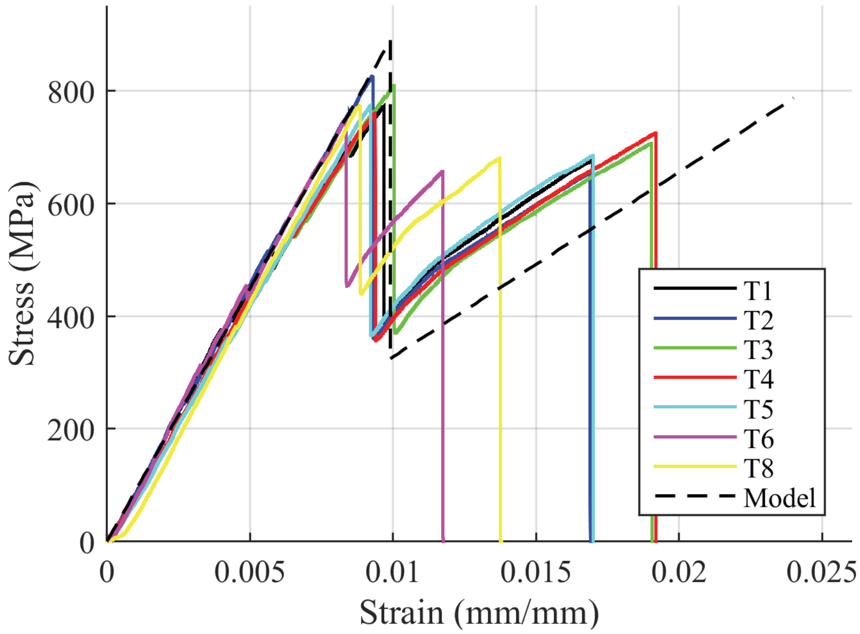

Figure 5.15: Stress-strain plot comparing experimental results and model predictions

Table 5.2: Comparison of experimental and predicted tensile test results

	E_{x1} (GPa)	E_{x2} (GPa)	σ_y (MPa)	σ_d (MPa)	σ_{ult} (MPa)	ε_y (mm/mm)	ε_{ult} (mm/mm)
Experimental	84.2 ± 7.5	36.3 ± 7.4	782 ± 27	390 ± 40	684 ± 26	0.0093 ± 0005	0.0164 ± 0.0027
Predicted	89.9	32.8	890	325	787	0.0099	0.0240

5.5.3 Optical Strain Measurement Results

Optical strain measurement was conducted on three of the rebar specimens, in an attempt to capture strain information directly for the entire duration of the test. Unfortunately, the data showed a large amount of variation from the physical extensometer data, making it difficult to have confidence in the quantitative results. The rebar posed several physical challenges that made it difficult to implement the OSM system. First, the rebar has a curved and undulating surface, which can lead to slight curvature in the contrast marks, and can influence the accuracy of the strain measurements. The surface of the braid was also glossy, which, combined with the undulations, led to some unwanted glare and shadows in the images. However, the OSM results did follow the same overall trend as the extensometer results, and were useful in qualitatively examining the behavior of the rebar during and after yielding.

The OSM strain data showed two different types of strain behavior surrounding the yielding event. Plots of strain versus time are shown in Figure 5.16 for these two behaviors. OSM-1 showed an abrupt jump in strain at the yield point of the rebar, whereas OSM-2 showed the opposite behavior, with an abrupt drop in strain at the yield point. In both cases, the strain began to increase once again after yielding. There was one important difference between the two tests that may explain the strain phenomena being observed. In OSM-1, the failure occurred near the OSM measurement location, while in OSM-2, the failure occurred away from this location, as shown schematically in Figure 5.17. The relative failure locations appear to have a significant impact on the measured strain. It seems yielding influences the local strain distribution of the rebar, causing the strain to no longer be uniform over the entire gage length of the bar. This behavior may help to explain the difference in failure strain observed between the model predictions and the experimental results.

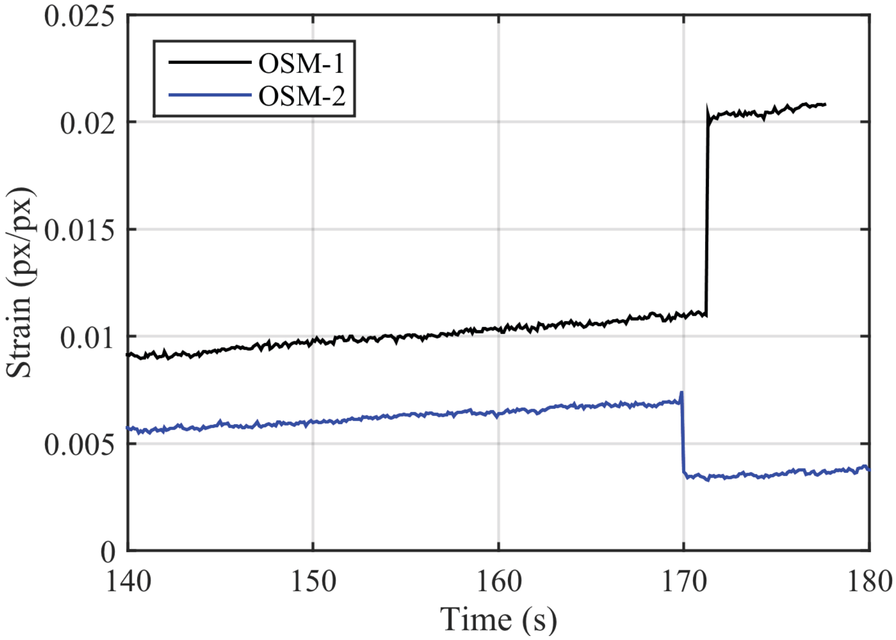

Figure 5.16: Local strain versus time as measured by OSM in rebar near failure site (OSM-1), and away from failure site (OSM-2)

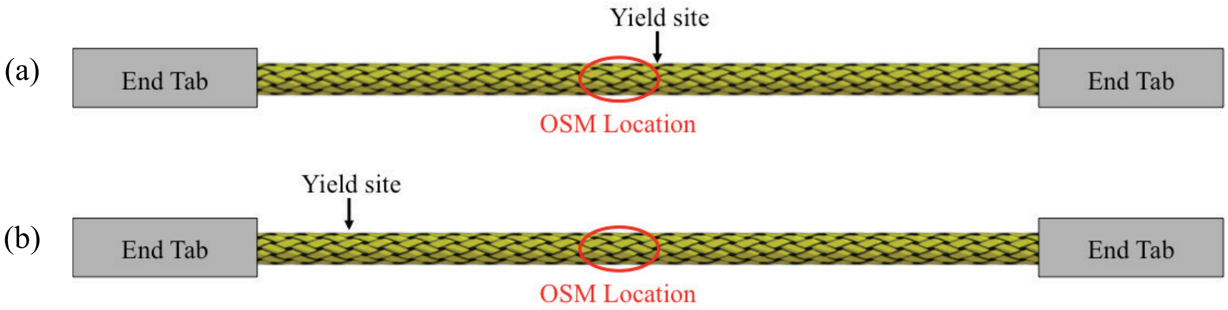

Figure 5.17: Schematic of yield site relative to OSM location for specimens: (a) OSM-1 and (b) OSM-2

5.5.4 Evaluation of Failure Mechanism

The OSM measurements revealed that after yielding of the bar, the strain is no longer uniform across the rebar gage length. Instead, the local strain around the failure site increases instantaneously, while the local strains away from the failure site drop. This has a significant influence on the ultimate failure strain of the rebar that is not fully captured by the model presented in Section 5.3. A second model was, therefore, developed in an attempt to better represent the tensile behavior of the rebar. The model was implemented using code written in MATLAB®, which can be found in Appendix F.

In order to examine the local strains in different regions of the bar, the rebar can be modeled as a series of springs. Before yielding, the rebar is viewed as a single spring with uniform stiffness, as shown in Figure 5.18. The stiffness of this spring is defined by its spring constant, k, and can be expressed in terms of elastic modulus, E, cross-sectional area, A, and length, L, as shown in Equation 5.16 [20]. In this model, L corresponds to the gage length of the rebar. When the rebar is loaded, the force, F, in the spring can be related to its displacement, x, in terms of k, using Equation 5.17 [20].

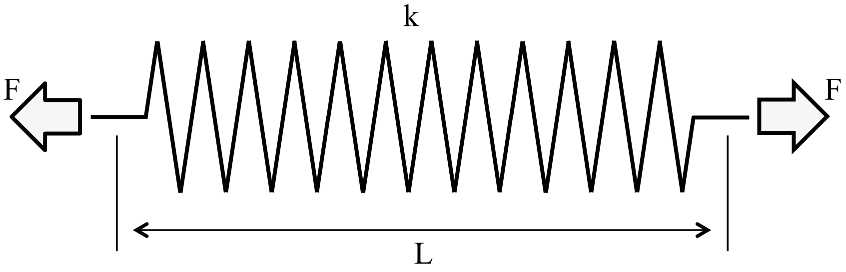

Figure 5.18: Schematic of single spring approximating of rebar prior to yielding

$$k = \frac{EA}{L} \qquad [5.16]$$

$$F = kx \qquad [5.17]$$

When yielding occurs, the rebar core fails locally in a single location along the rebar gage length. When this happens, the rebar may be modeled as three springs of varying stiffness, as shown in Figure 5.19, where the middle spring (spring 2) represents the failure location. Springs 1 and 3 are assumed to maintain the same elastic modulus as the original rebar, since the core is still intact in these regions. The elastic modulus in spring 2 will be lower, as in this region, the failed core is assumed to no longer contribute to the composite structure. When the three springs are arranged in series, the global spring constant, k_{tot}, can be found by combining k_1, k_2, and k_3 as shown in Equation 5.18 [20]. When the series of springs is loaded, each spring will experience the same force, *F*, and the total elongation of the series is equal to the sum of the elongation in each spring [20], resulting in Equation 5.19. In this equation, A_1 is the total cross-sectional area of the core and braid combined, and A_2 is the cross-sectional area of the braid only. The areas are as calculated by Equation 5.2.

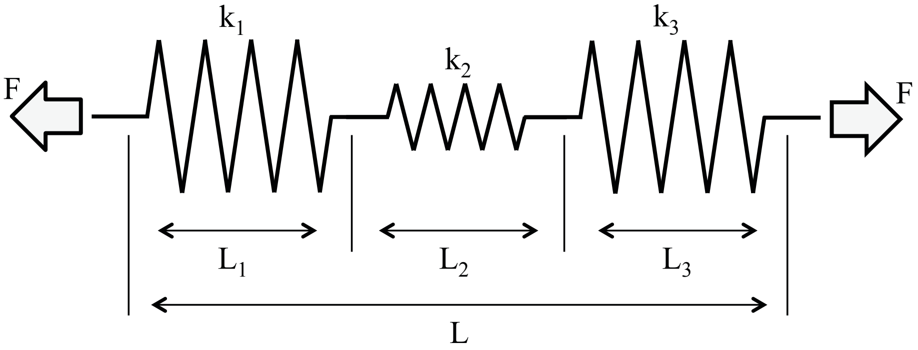

Figure 5.19: Schematic of three-spring approximation of rebar post yielding

$$k_{tot} = \frac{1}{\frac{1}{k_1} + \frac{1}{k_2} + \frac{1}{k_3}} \qquad [5.18]$$

$$x_{tot} = x_1 + x_2 + x_3 = \frac{F}{k_{tot}} = F\left(\frac{1}{k_1} + \frac{1}{k_2} + \frac{1}{k_3}\right) = F\left(\frac{L_1}{E_1A_1} + \frac{L_2}{E_2A_2} + \frac{L_3}{E_1A_1}\right) \qquad [5.19]$$

Equations 5.16, 5.17, 5.18, and 5.19 can be manipulated to predict the loads, displacement, stresses, and strains in the rebar before, during, and after yielding. The load to cause yielding can be calculated using Equation 5.20, Where $E_{x,1}$ is the same as was calculated by the volume average stiffness method in section 5.3 for the fully intact rebar, and ε_y is the rebar yield strain, which corresponds to the failure strain of the carbon fibers (same as in the previous model).

$$F = \frac{E_{x,1}A_1x}{L} \quad , \qquad F_y = E_{x,1}A_1\varepsilon_y \qquad [5.20]$$

After yielding, however, the three-spring model comes into play. Equation 5.21 relates the various spring lengths and the overall gage length of the rebar, *L*. Substituting Equation 5.21 into

Equation 5.19, and rearranging, yields Equation 5.22 to find the length of the soft spring, L_2, which corresponds to the damaged portion of the rebar after yielding. In this equation, $x_{tot,y}$ is the total displacement in the bar at yielding, and F_d is the dropped load in the rebar after yielding. Assuming the failure occurs in the center of the gage length, L_1 and L_3 are assumed to be equal, and are found by Equation 5.23.

$$L_1 + L_3 = L - L_2 \tag{5.21}$$

$$L_2 = \frac{\frac{x_{tot,y}}{F_d} - \frac{L}{E_1 A_1}}{\left(\frac{1}{E_{x,2} A_2} - \frac{1}{E_{x,1} A_1}\right)} \tag{5.22}$$

$$L_1 = L_3 = \frac{L - L_2}{2} \tag{5.23}$$

Once L_1, L_2, and L_3 are known, the local displacement in each spring can be calculated, as shown in Equation 5.24. The strains in each spring can then be calculated by dividing the local displacement by the spring length (Equation 5.25). The average global strain in the rebar remains the total displacement divided by the total gage length, as shown in Equation 5.26.

$$x_{1,d} = \frac{F_d L_1}{E_{x,1} A_1}, \qquad x_{2,d} = \frac{F_d L_2}{E_{x,2} A_2}, \qquad x_{3,d} = \frac{F_d L_3}{E_{x,1} A_1} \tag{5.24}$$

$$\varepsilon_{1,d} = \frac{x_{1,d}}{L_1}, \qquad \varepsilon_{2,d} = \frac{x_{2,d}}{L_2}, \qquad \varepsilon_{3,d} = \frac{x_{3,d}}{L_3} \tag{5.25}$$

$$\varepsilon_{avg,d} = \frac{x_{1,d} + x_{2,d} + x_{3,d}}{L} \tag{5.26}$$

As in the previous model, it is assumed that the ultimate failure strain of the rebar, $\varepsilon_{2,ult}$, is dictated by the ultimate strain of the braid fibers, $\varepsilon_{b,f}$, as described in Equation 5.27.

$$\varepsilon_{2,ult} = \varepsilon_{b,f} \qquad [5.27]$$

The displacement in spring 2 at ultimate failure can then be calculated by Equation 5.28, and the ultimate failure load, F_{ult}, can be predicted based on $x_{2,ult}$ and the stiffness of the spring, using Equation 5.29.

$$x_{2,ult} = \varepsilon_{2,ult} L_2 \qquad [5.28]$$

$$F_{ult} = \frac{E_{x,2} A_2 x_{2,ult}}{L_2} \qquad [5.29]$$

Once F_{ult} has been established, the displacements in springs 1 and 3 can be found using Equation 5.3, and their corresponding strains can be found from Equation 5.31. Finally, the average global strain at failure, $\varepsilon_{tot,ult}$ is calculated based on the total displacement and gage length, as shown in Equation 5.32.

$$x_{1,ult} = \frac{F_{ult} L_1}{E_{x,1} A_1} \ , \qquad x_{3,ult} = \frac{F_{ult} L_3}{E_{x,1} A_1} \qquad [5.30]$$

$$\varepsilon_{1,ult} = \frac{x_{1,ult}}{L_1} \ , \qquad \varepsilon_{3,ult} = \frac{x_{3,ult}}{L_3} \qquad [5.31]$$

$$\varepsilon_{tot,ult} = \frac{x_{1,ult} + x_{2,ult} + x_{3,ult}}{L} \qquad [5.32]$$

To express the model in terms of stress and strain, the load values are converted into stresses simply by dividing them by the initial cross-sectional area of the rebar, as shown in Equation 5.33. Expressing the tensile behavior in terms of stress and strain allows the model to be more easily compared to the previous model and experimental results.

$$\sigma_y = \frac{F_y}{A_1} \ , \qquad \sigma_d = \frac{F_d}{A_1} \ , \qquad \sigma_{ult} = \frac{F_{ult}}{A_1} \qquad [5.33]$$

In this model, the choice of the spring lengths, L_1, L_2, and L_3 has a major effect on the predicted tensile response of the rebar, as they affect both the stiffness and ultimate elongation of the bar. Figure 5.20 shows the effect of changing L_2 on the tensile properties of the rebar. In this plot, the global rebar strain is used. The upper limit corresponds to the case where the braid reaches its failure strain as soon as yielding occurs. This represents the smallest possible value of L_2. The lower limit represents the case where L_2 takes up the entire gage length of the rebar, resulting in the maximum possible strain in the rebar. This lower limit results in the same curve as the original model in Section 5.3, as both methods are essentially fully discounting the carbon core after yielding. Between these limits, decreasing L_2 leads to increasing stiffness and decreasing ultimate strain of the rebar, as well as less of a load drop at yielding. A similar trend was observed in the experimental data where lower load drops led to higher rebar stiffness and lower ultimate strain.

The main limitation of this model is that, as shown by Equation 5.22, the choice of L_2 is dependent on the dropped load in the rebar after yielding, F_d. This load, however, is dependent on the stiffness of the rebar after yielding, which cannot be determined until spring lengths L_1, L_2, and L_3 are known. Therefore, either F_d or L_2 needs to be chosen based on experimental data before the model can be used.

Figure 5.21 shows an updated stress-strain plot comparing the experimental results to the original model and updated spring model. The strain shown in this plot is global strain in the rebar. In order to select F_d, a load drop at yielding of 50% was chosen for the spring model, as this was the average load drop observed in the experiments. For this case, the spring model predicts a global failure strain of 0.0175 mm/mm, which is in good agreement with the average experimental failure strain of 0.0164 ± 0.0027 mm/mm. This is an improvement over the original model, which assumed a failure strain of 0.024 mm/mm, corresponding to the ultimate strain in the aramid fibers. The elastic modulus after yielding predicted by the spring model was 46.7 GPa, which is slightly higher than that of the experimental results. The initial elastic modulus, and yield stress and strain are identical to the original model.

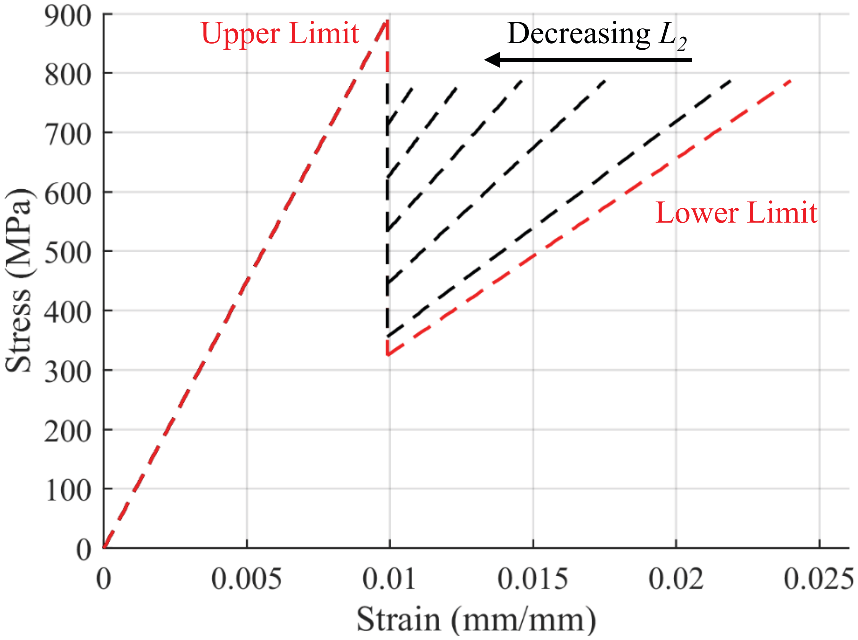

Figure 5.20: Effect of changing L_2 on the predicted tensile response of the rebar

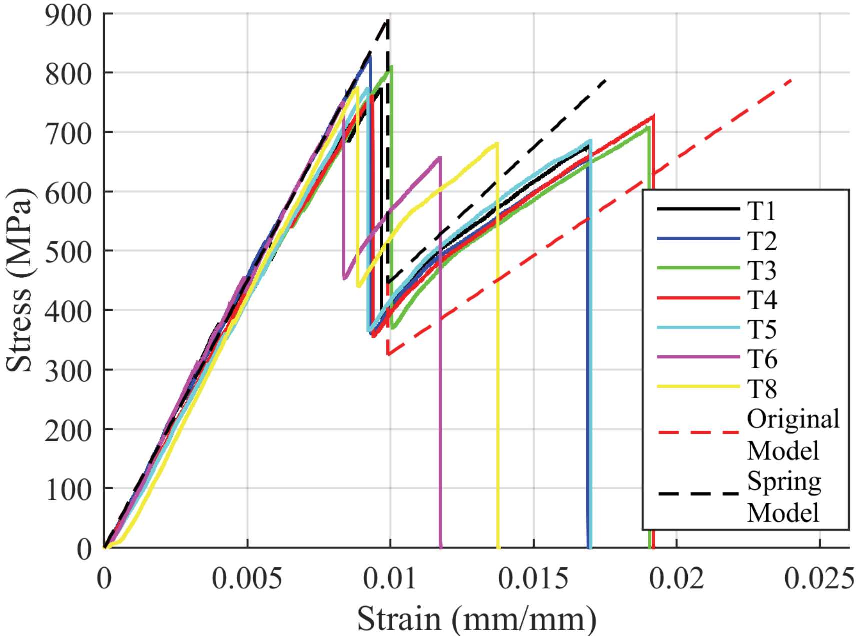

Figure 5.21: Stress-strain plot comparing experimental results, original model, and spring model

By taking into consideration the effects of varying local strains in the rebar after yielding has occurred, the tensile response predicted by the spring model can be fit to experimental data to result in a closer approximation of the ultimate failure strain of the rebar. When failure of the rebar is strain-limited, these local strains are important predict its failure behavior, since failure will occur at the first location along the bar to reach its ultimate strain. This represents an important improvement over previous studies that assumed uniform strain along the entire length of the rebar [3-5]. The model also allows for the tensile response to be predicted as a function of the magnitude of the load drop at yielding, which will be useful for tailoring the mechanical properties of future rebar.

The spring model could be improved in the future by taking into account the undulations of the braid yarns. In the current model, elastic modulus is calculated based on a flat laminate, which neglects undulations and curvature of the braid. These factors have been shown to affect the elastic properties of braided composites [21], and may help improve the accuracy of the elastic modulus predictions, particularly after yielding.

One of the limitations of this model is that the predicted rebar displacement depends on the choice of L. Due to the compliance of the test system, choosing the gage length of the rebar for L yields lower displacements than observed experimentally, making it difficult to compare experimental and predicted results without first converting to strain. The choice of L, does not affect the strain predictions, as the displacement will change proportionately with L, making it best to compare results in terms of load versus strain or stress versus strain.

5.6 CONCLUSIONS

The objectives of this chapter were to determine the mechanical properties of the rebar manufactured by dieless braidtrusion and to develop a model to accurately predict the tensile response of the rebar. A failure mechanism was proposed for the rebar involving a two stage failure, characteristic of hybrid FRP composites. Two models were developed; the first model considered the rebar as a laminate to calculate elastic properties, and assumed uniform strain over the entire gage length. After yielding, the core was fully discounted and the elastic properties were assumed to be dominated by the braid. The second model considered the rebar after yielding as a series of springs of varying stiffness, and local elongations and stiffness of each spring were used to determine the overall rebar properties. In both models, ultimate failure was limited by the failure strain of the braid fibers.

Tensile tests were conducted on the rebar specimens and showed good repeatability and exhibited a pseudoductile failure mode with an initial elastic modulus of 84.2 ± 7.5 GPa and yield strength of 782 ± 27 MPa at a strain of 0.0093 ± 0.0005 mm/mm. The results were compared to the analytical models; the first model did a good job of predicting the tensile response up to the yield point, but over-predicted the ultimate strain of the rebar. OSM results revealed that local strains were not consistent across the rebar gage length after yielding. These local strain variations were taken into account in the spring model, leading to a closer approximation of the rebar failure strain. By fitting the results of the spring model to the experimental data using the magnitude of the load drop after yielding, the spring model predicted a failure strain of 0.175 mm/min, which was in good agreement with the average experimental value of 0.0164 ± 0.0027 mm/min.

These findings help to provide a better understanding of the failure mechanism in this type of hybrid FRP rebar, which will allow for improved rebar design, as the local strain variations have an important effect on pseudoductility. The final model presented in this chapter can be used as a tool to help facilitate the development of future FRP rebar using different materials, core to braid proportions, and geometric parameters.

5.7 REFERENCES

[1] Aveston, J., and Kelly, A., 1980, "Tensile First Cracking Strain and Strength of Hybrid Composites and Laminates," Physical Sciences, **294**(1411) pp. 519-534.

[2] Bunsell, A. R., and Harris, B., 1974, "Hybrid Carbon and Glass Fibre Composites," Composites, pp. 157-164.

[3] Hampton, F., 2004, "Cyclic Behavior, Development, and Characteristics of a Ductile Hybrid Fiber Reinforced Polymer (DHFRP) for Reinforced Concrete Members," Drexel University. United States.

[4] Somboonsong, W., Ko, F. K., and Harris, H. G., 1998, "Ductile Hybrid Fiber Reinforced Plastic Reinforcing Bar for Composite Structures: Design Methodology," ACI Materials Journal, **95**(6) pp. 655-666.

[5] Pastore, C., Armstrong-Carroll, E., and Ko, F., 2012, "Effect of Yarn Size on the Performance of Hybrid Braided Composite Rebar," The Masterbuilder, pp. 234-244.

[6] Harris, H. G., Somboonsong, W., and Ko, F. K., 1998, "New Ductile Hybrid FRP Reinforcing Bar for Concrete Structures," Journal of Composites for Construction, **2**pp. 28-37.

[7] Ko, F., Head, A., and Pastore, C., 1989, "Handbook of Industrial Braiding," Atkins and Pearce, Covington, Kentucky.

[8] Du, G., and Popper, P., 1994, "Analysis of a Circular Braiding Process for Complex Shapes," The Journal of the Textile Institute, **85**(3) pp. 316-337.

[9] Agarwal, B.D., and Broutman, L.J., 1990, "Analysis and Performance of Fiber Composites, Second Edition," John Wiley & Sons, New York, NY.

[10] Byun, J., 2000, "The Analytical Characterization of 2-D Braided Textile Composites," Composites Science and Technology, **60**pp. 705-716.

[11] Kaw, A.K., 2006, "Mechanics of Composite Materials, Second Edition," Taylor & Francis Group, Boca Raton, FL.

[12] Quek, S. C., Waas, A. M., Shahwan, K. W., 2003, "Analysis of 2D Triaxial Flat Braided Textile Composites," International Journal of Mechanical Sciences, **45**pp. 1077-1096.

[13] ASTM International, 2011, "ASTM D7205/D7205M-06 Standard Test Method for Tensile Properties of Fiber Reinforced Polymer Matrix Composite Bars," pp.1-13.

[14] ACI Committee Report, "ACI 440.3R-04 Guide Test Methods for Fiber-Reinforced Polymers (FRPs) for Reinforcing Or Strengthening Concrete Structures," pp.1-40.

[15] Elzafraney, M., and Soroushian, P., 2006, "Testing Techniques and Tools to Determine Properties of Fiber-Reinforced Rods," Journal of Testing and Evaluation, **34**(2) pp. 1-8.

[16] Sika Canada, 2012, "Product Data Sheet: Sikadur 35 Hi-Mod LV".

[17] Frank, S., and Spolenak, R., "Optical Strain Measurement by Digital Image Analysis," Http://Www.Mathworks.Com/Matlabcentral/Fx_files/20438/1/Content/Documentation.Htm.

[18] Czel, G., and Wisnom, M., 2013, "Demonstration of Pseudo-Ductility in High Performance Glass/Epoxy Composites by Hybridisation with Thin-Ply Carbon Prepreg," Composites: Part A, **52**pp. 23-30.

[19] Bakis, C. E., Nanni, A., Terosky, J. A., 2001, "Self-Monitoring, Pseudo-Ductile, Hybrid FRP Reinforcement Rods for Concrete Applications," Composites Science and Technology, **61**pp. 815-823.

[20] Weggel, D. C., Boyajian, D. M., and Chen, S., 2007, "Modelling Structures as Systems of Springs," World Transactions on Engineering and Technology Education, **6**(1) pp. 169-172.

[21] Ayranci, C., and Carey, J. P., 2010, "Predicting the Longitudinal Elastic Modulus of Braided Tubular Composites using a Curved Unit-Cell Geometry," Composites: Part B, **41**pp. 229-235.

6 DISCONTINUOUS REBAR FOR ENHANCED PSEUDODUCTILITY

6.1 INTRODUCTION

As seen in the previous chapters, FRP rebar has been successfully developed that behaves in a pseudoductile manner under tensile loading. However, as is the case with other hybrid composites [1-3], the ultimate failure strain of the rebar remains relatively low and is limited by the failure strain of the more ductile fiber component. In this chapter, an alternative approach to pseudoductility, utilizing the interfacial properties of multiple composite layers, is implemented in an attempt to add to the ductility of the rebar developed in this thesis.

In his past work, Ewen [4] proposed the idea of using frictional shear forces between interfaces in a composite rod in order to obtain large deformations under tensile loading. Unidirectional FRP rods were encased in a thin braided sheath. The sheath served as an interface against which the rod would slide during tensile loading, and was cut at regular intervals along the rebar, making it discontinuous. The discontinuities is the braid were intended to result in sliding between the rod and sheath interface, based on the concept of short fiber pullout, producing the pseudoductile behavior. The concept showed promise as a method for achieving large displacements in FRP reinforced concrete; however, test results were mixed due to difficulties in controlling the interfacial properties of the composite. A similar mechanism was studied by Czel [5] for laminated composites. A combination of continuous and discontinuous composite layers was used to achieve a stable pullout rather than unstable delamination in a hybrid composite.

By incorporating a pullout type mechanism into the current FRP rebar design, it may be possible to further extend the ductility of the existing rebar and reduce the severity of ultimate failure. In this chapter, an updated rebar design is presented that relies on interfacial sliding between composite layers as a means of enhancing pseudoductility after yielding. The design concept is presented, along with the proposed failure mechanism. Specimens are manufactured and preliminary experiments are conducted to observe the tensile behavior of the rebar and assess the viability of proposed failure mechanism.

6.2 SHORT FIBER COMPOSITES

In FRP composite materials, the length of the reinforcing fibers can have an important influence on the mechanical properties. There exists a critical length, L_c, at which the frictional forces at the fiber-matrix interface are balanced with the tensile force in the fiber when loaded to its maximum tensile stress [4]. If the fiber is longer than L_c, failure will be by fiber fracture, as the interfacial strength exceeds the tensile strength of the fiber. If the fiber is shorter than L_c, the interface will fail before the tensile strength of the fiber is reached, and the fiber will pull out of the matrix. Equation 6.1 [6] can be used to determine the critical length of a fiber, where τ is the frictional shear stress at the interface (assumed to be constant), P is the load in the fiber, and D is the fiber diameter.

$$L_c = \frac{P}{\pi D \tau} \qquad [6.1]$$

When the fiber length is smaller than L_c, Equation 6.1 can be manipulated to predict the load in a fiber based on the embedded length of the fiber, L_e, as it is being pulled out of the matrix, resulting in Equation 6.2. This concept can be applied to tailor the rebar structure, such that pullout is induced before ultimate failure as a way of improving pseudoductility.

$$P = \pi D \tau L_e \qquad [6.2]$$

6.3 DESIGN CONCEPT

Rebar was designed to take advantage of interfacial sliding between composite layers in order to achieve large displacements during tensile loading. The rebar materials and composite architecture are the same as the previous rebar design, however, here, discontinuities were introduced into the braid structure, as shown schematically in Figure 6.1. The purpose of the discontinuities was to allow pullout to occur between the core and braid portions of the rebar. By changing the length between discontinuities, the pullout properties of the rebar can be tailored.

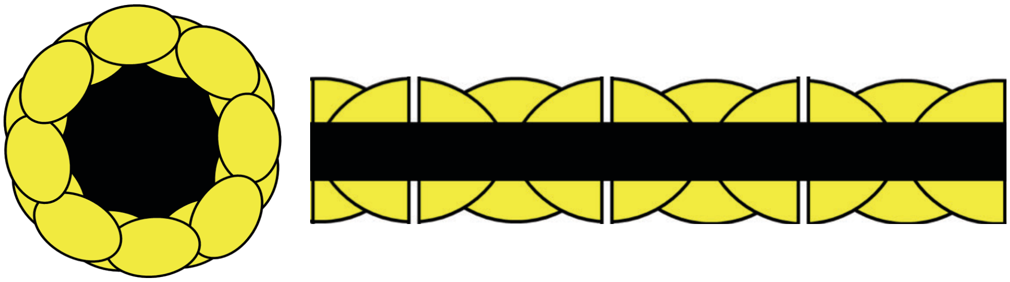
(a) (b)

Figure 6.1: Schematic of updated rebar design. (a) Cross sectional appearance, (b) longitudinal section showing discontinuous braid with continuous core

A schematic of the proposed failure mechanism is presented in Figure 6.2, and the corresponding idealized load-displacement behavior is shown in Figure 6.3. Consider a situation where the discontinuous rebar is embedded in concrete under tension. As the structure is loaded (region A), a crack will form in the concrete at low strain, creating a stress concentration and exposing the rebar. As loading continues, the rebar yields at the crack location when the failure strain of the core fibers is reached (point B), resulting in a load drop characteristic of hybrid composites. When the core fractures during yielding, the embedded length of the core inside the discontinuous braid (shown in Figure 6.2(b)) drops below L_c, making it possible for pullout to occur. The intact braid picks up the load in region C, and load continues to increase until the load required to cause pullout between the core/braid and braid/concrete interfaces is reached (point D). The rebar then pulls out at point E, causing load to decrease as displacement increases (based on Equation 6.2) until the rebar is completely pulled out. Pullout occurs at both the core/braid interface, and the braid/concrete interface.

It should be noted that the initial elastic modulus and yielding behavior is expected to remain the same as the rebar in Chapter 5, after which point the pullout mechanism can take place. The pullout behavior is based on the rebar being embedded in concrete, and final pullout occurs only near the crack location, leaving the rest of the rebar away from this location intact. In this design, stress and stain cannot be defined for the pullout portion of the curve, as the rebar is not being strained in this region. Since the elastic properties of the rebar up to yielding have already been characterized, this chapter uses load and displacement to express mechanical test results and focuses on the post-yielding behavior of the rebar.

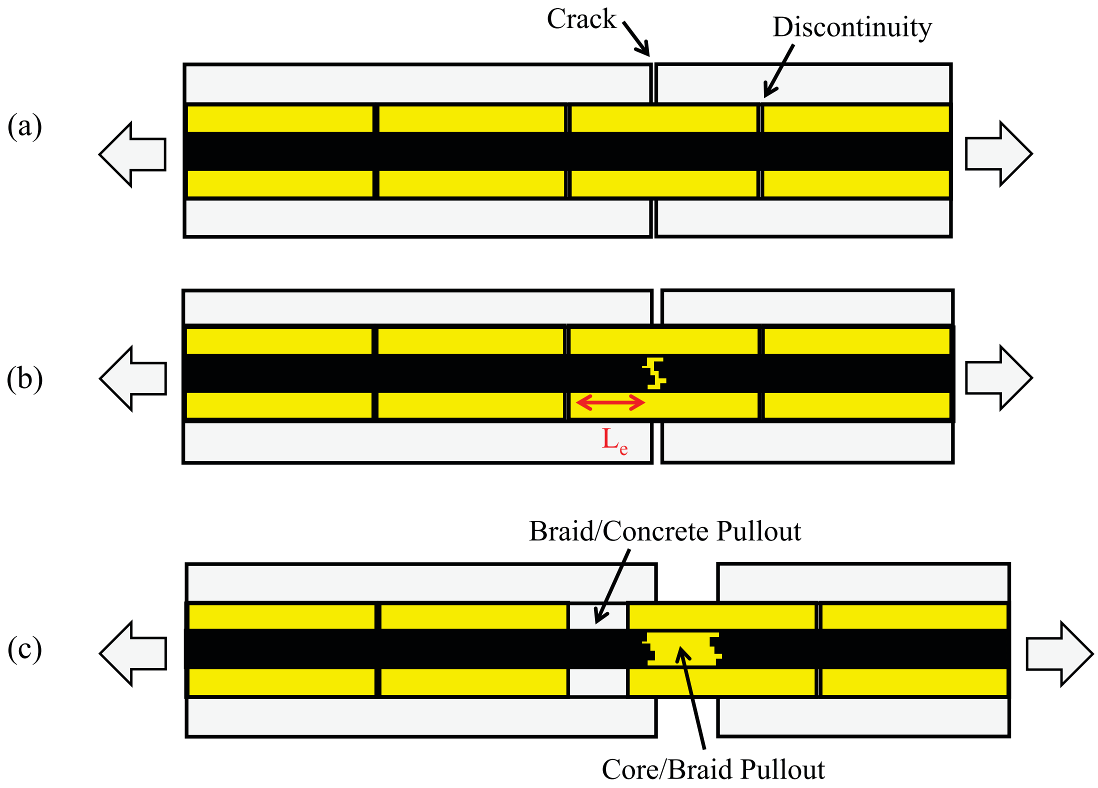

Figure 6.2: Schematic of proposed failure mechanism for discontinuous rebar design. (a) Crack formed in concrete between discontinuities in rebar, (b) yielding of rebar at crack location, (c) pullout of rebar after reloading

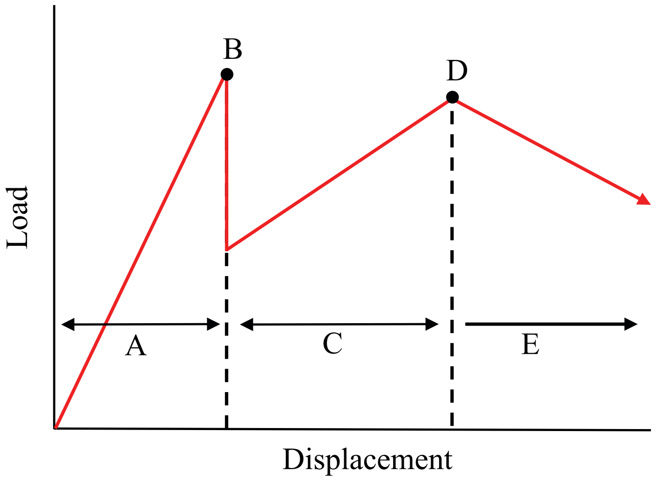

Figure 6.3: Schematic of load-displacement behavior duringg proposed failure mechanism. A: Initial loading, B: yield point, C: reloading of braid, D: initiation of pullout, E: decreasing load as pullout progresses

6.4 MATERIALS & METHODS

Rebar specimens were manufactured using the braidtrusion process described in Chapter 4. Specimens were prepared for pullout testing to first characterize the interfacial properties, then tensile test specimens were prepared to evaluate the viability of the proposed failure mechanism.

6.4.1 Pullout Testing

Pullout testing was performed to find the interfacial shear strength at the core/braid interface and the braid/potting interface. The pullout characteristics at these two interfaces are important to the selection of the length between discontinuities in the final rebar. Specimens were mounted in end tabs to facilitate pullout testing. The end tabs were similar to those described in Chapter 5 for tensile testing of the rebar. The same mounting techniques were applied, and the same potting resin (Sikadur 35 Hi-Mod LV) was used. Care was taken to ensure that samples were well aligned and straight.

The pullout test setup for the core/braid interface tests is shown schematically in Figure 6.4(a). Rebar specimens were anchored at a depth of 100 mm on one end and were potted to a depth of 50 mm on the other. The potting resin was allowed 7 days to cure at room temperature prior to testing to ensure consistency across all tests. The braided overwrap was cut to create a discontinuity in the middle of the gage length, approximately 70 mm from the potted end. This 70 mm portion of the rebar core was pulled out of the braid using a uniaxial mechanical testing system (Instron, USA), equipped with a 44.4 kN (10000lbf) load cell. A constant displacement rate of 1.27 mm/min (0.05 in/min) was used for all tests. Load and crosshead displacement data was recorded at a rate of 10 samples per second.

The pullout test setup for the braid/potting interface tests is shown schematically in Figure 6.4(b). The rebar was anchored 100 mm on one end, and potted 50 mm on the other end. In this case, no discontinuities were made in the braided overwrap, and the short end of the rebar was simply pulled out of the potting resin. Otherwise, test conditions were the same as for the core/braid pullout test.

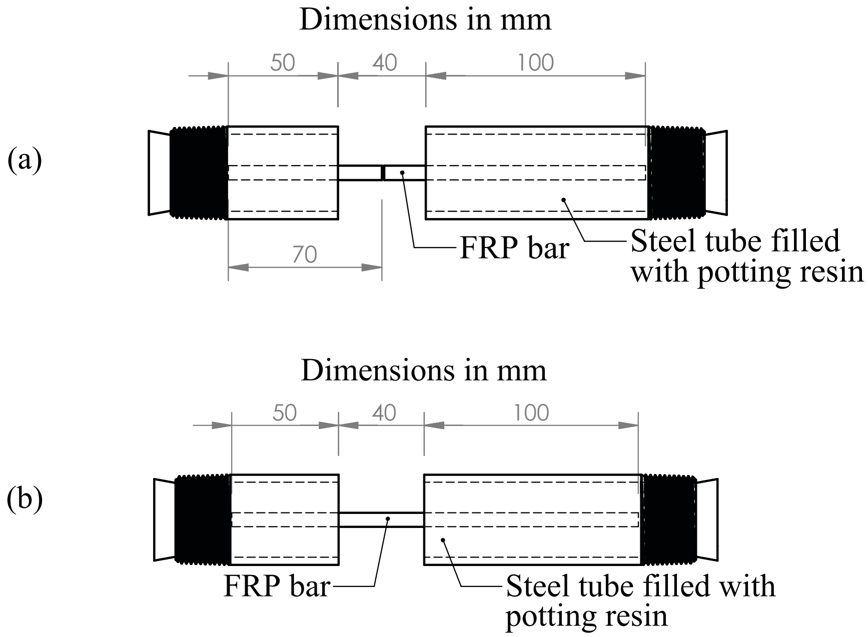

Figure 6.4: Schematic of pullout test specimens for (a) core/braid and (b) braid/potting interfaces (dimensions in mm)

6.4.2 Tensile Testing

Tensile tests were designed to simulate failure by the mechanism described in Section 6.3. Figure 6.5 shows a schematic of the tensile test setup. Rebar specimens were cut to lengths of 390 mm and were anchored at a depth of 175 mm at one end. This end was intended to remain fixed during testing, and not experience any pullout, therefore, no discontinuities were made in this portion of the rebar. The other side was also potted to a depth of 175 mm, however on this side, a single discontinuity was made in the braid to provide an initiation point for pullout to occur. The location of the discontinuity is specified in Figure 6.5 by L_d, and will be referred to as the "discontinuity length". The same potting resin (Sikadur® 35 Hi-Mod LV, Sika, Canada) was used in the tensile tests, rather than concrete, due to availability and relatively rapid curing of the resin when compared to concrete. While using concrete would result in different pullout loads, the general pseudoductile mechanism should be unaffected by the potting medium. A gage length of 40 mm was left between the two end tabs to represent a crack in the concrete. In these tests, it was intended for the core of the rebar to yield somewhere in the gage length, leading to pullout from the end tab containing the discontinuity in the braid. Tests were conducted using the same uniaxial tensile test system (Instron, USA) and 44.4 kM (10000lbf) load cell as for the pullout tests, and a constant displacement rate of 1.27 mm/mm (0.05 in/min). Load and displacement data was recorded, at a rate of 10 samples per second.

The results of the pullout tests were used to guide the choice of L_d for tensile testing. Tensile test specimens were produced with L_d values of 30 mm, 50 mm, and 70 mm. Ten samples were manufactured with an L_d of 30 mm, three with L_d of 50 mm, and one with L_d of 70 mm.

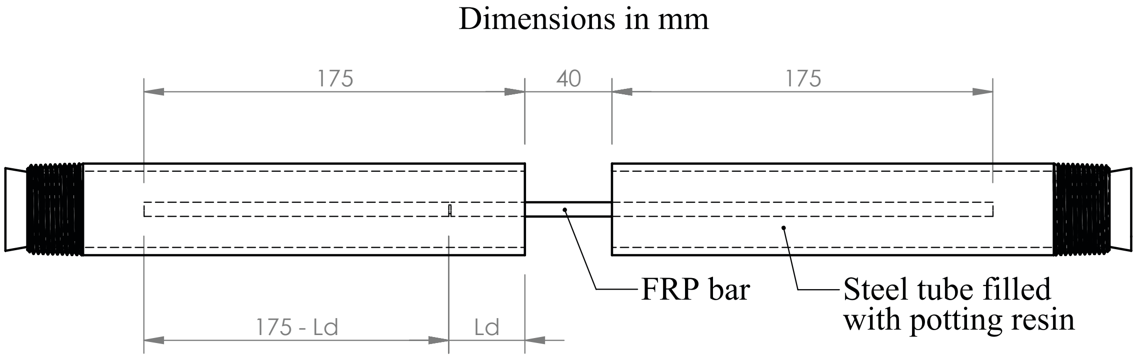

Figure 6.5: Schematic of tensile test specimen for discontinuous rebar (dimensions in mm)

6.4.3 Creation of Braid Discontinuities

Discontinuities needed to produce the pullout effect in both the pullout and tensile tests were cut into the braided overwrap at specified locations, as shown in Figure 6.6. A handheld rotary grinding tool (Dremel® 100 series, Dremel, USA) was used to cut into the braid all the way around the rebar, and grinding was stopped just before reaching the carbon core. A scalpel was used to finish cutting through any remaining braid material, and care was taken to avoid cutting into the core. The cuts were filled with silicon caulking to prevent the potting resin from adhering to the exposed core and ensure that the pullout behavior was not affected by the potting resin bonding to the core.

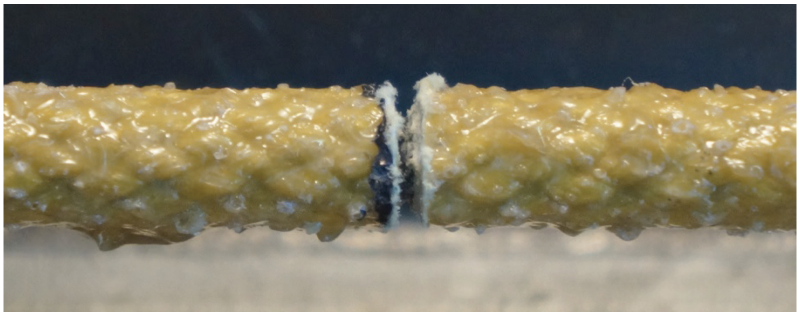

Figure 6.6: Example of discontinuity cut into braided overwrap

6.5 RESULTS AND DISCUSSION

6.5.1 Pullout Results and Interfacial Properties

Representative plots of load of the pullout test results for both the core/braid and braid/potting interfaces are shown in Figure 6.7. Both curves increased linearly following similar slopes up to a maximum load at which a sudden load drop was observed, followed by a steady decrease in load as pullout progressed. The load drop can be attributed to debonding of the interface [4] and is a common occurrence in these types of tests. Images showing examples of the pulled-out specimens are shown in Figure 6.8.

The core/braid interface tests showed an average maximum load of 12.1 ± 1.8 kN, which then dropped by approximately 83% during debonding. The following pullout curve was smooth and decreased in an approximately linear fashion until pullout was complete.

The braid/potting interface tests resulted in a higher average maximum load of 15.0 ± 0.8 kN, and a less severe load drop of only 52%. The following pullout behavior, however, resulted in a wavy curve, with a fluctuating load of decreasing amplitude until pullout was complete. This type of curve resembles stick-slip behavior [7], and was due to the undulating surface of the braid causing mechanical keying with the surrounding potting resin.

Table 6.1 summarizes the test results for the core/braid and braid/potting interface tests. Average and standard deviation of the outer diameter, maximum load to initiate pullout, and corresponding shear strength to initiate pullout in each interface are provided. Shear strengths were calculated based on Equation 6.2 by taking P as the maximum load, L_e as the original embedded length, and D as the outer diameter of the core or the braid (depending on the interface). These values will help to determine the required length between discontinuities to optimize the pseudoductile pullout behavior in the FRP rebar.

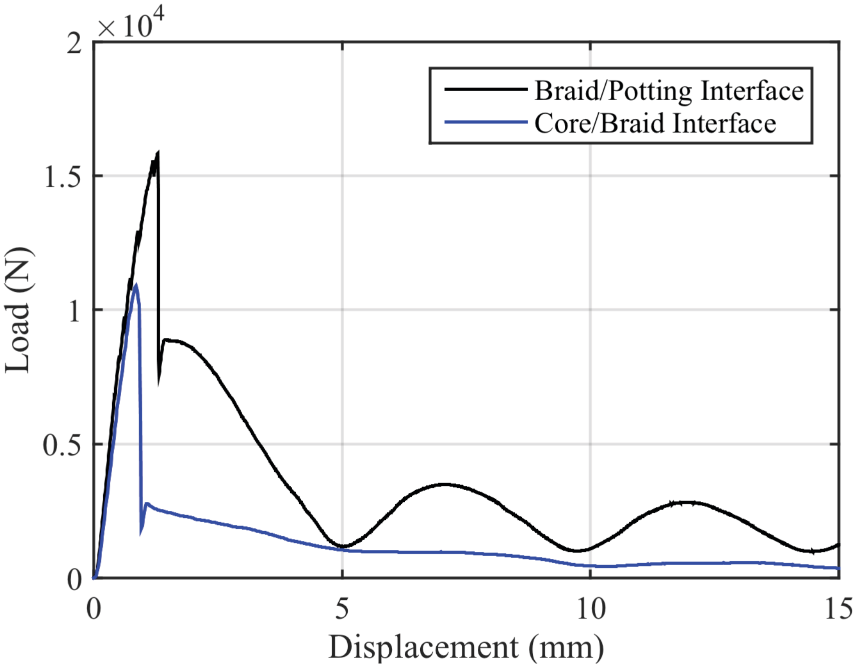

Figure 6.7: Characteristic pullout behavior for core/braid and braid/potting interface tests

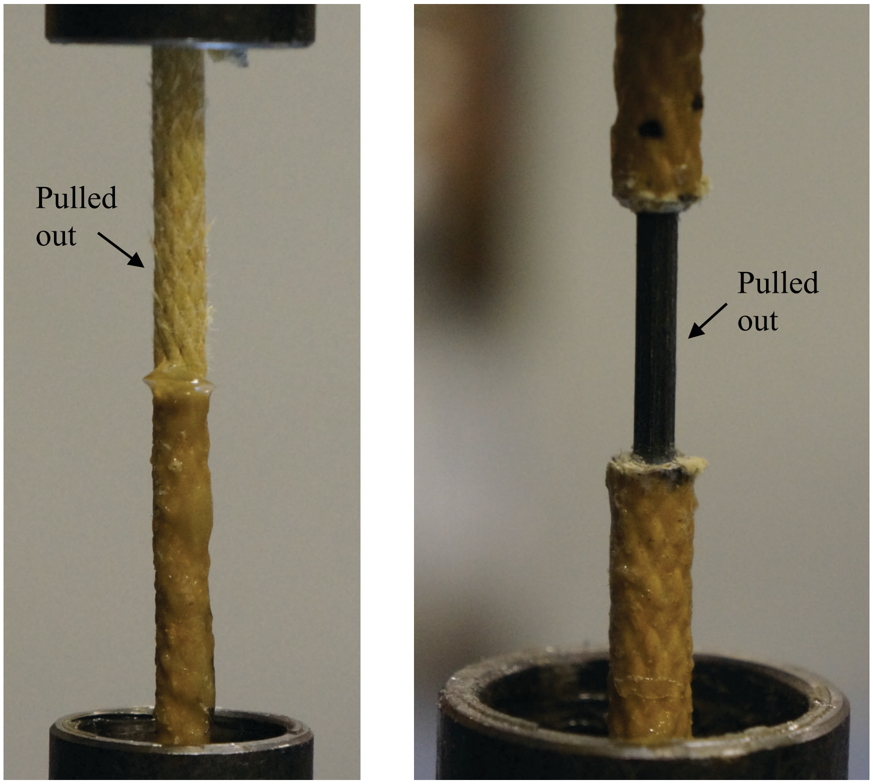

(a) (b)

Figure 6.8: Example of pulled-out specimens; (a) braid/potting interface, (b) core/braid interface

Table 6.1: Summary of pullout test results

Interface	Outer Diameter (mm)	Max Load (kN)	Shear Strength (MPa)
Core/Braid	3.78 ± 0.06	12.1 ±1.8	15.9 ± 2.3
Braid/Potting	6.47 ± 0.13	15.0 ± 0.80	15.6 ± 1.2

6.5.2 Selection of Discontinuity Length

The pullout data was used to guide the selection of the discontinuity length, L_d, which was used to induce pullout in the tensile test specimens. Discontinuity lengths of 30 mm, 50 mm, and 70 mm were considered. The pullout loads for both the core/braid and braid/potting interfaces were calculated following Equation 6.2 at each of the L_d values. The predictions are summarized in Table 6.2. It was assumed that yielding would occur somewhere inside the 40 mm gage length, therefore a range of pullout loads are predicted for the core/braid interface, depending on the location of yielding within the gage length.

Based on the tensile test results from Chapter 5, ultimate failure of the rebar was observed to occur at a load of 17.8 ± 0.7 kN. By comparing this failure load to the total pullout load, the failure mechanism can be predicted. For L_d values of 50 and 70 mm, the total pullout load is greater than the ultimate load, and tensile failure of the rebar is expected. For an L_d of 30 mm, either pullout or tensile failure was expected, depending on the location of yielding along the gage length. When yielding occurs close to the end tab containing the discontinuity, the total pullout load is below the ultimate tensile load, and pullout is expected to occur. When yielding is far from this end tab, the pullout load exceeds the ultimate tensile load, which is expected to lead to tensile failure.

Table 6.2: Summary of predicted pullout loads for discontinuous rebar post-yielding

L_d (mm)	Core/Braid Pullout Load (kN)	Braid/Potting Pullout Load (kN)	Total Pullout Load (kN)
30	5.7 – 13.2	9.5	15.2 – 22.7
50	9.4 – 17.0	15.9	25.3 – 32.8
70	13.2 – 20.8	22.2	35.4 – 43.0

6.5.3 Tensile Test Results

Tensile tests were conducted on fourteen specimens with L_d values of 30, 50, and 70 mm. Four different failure types were observed. Table 6.3 summarizes the failure type and L_d value for each specimen tested. Ten specimens with L_d of 30 mm were tested, as well as three specimens with L_d of 50 mm, and one with an L_d of 70 mm.

Table 6.3: Failure types for tensile test specimens of different discontinuity lengths

Sample	Failure Type	L_d (mm)
P1	1	50
P2	2	30
P3	2	50
P4	2	50
P5	3	30
P6	1	70
P7	2	30
P8	1	30
P9	3	30
P10	1	30
P11	4	30
P12	2	30
P13	3	30
P14	1	30

Type 1 failure corresponded to tensile failure of the rebar with no pullout observed, similar to the specimens tested in Chapter 5 that contained no discontinuities. Five specimens failed in this manner. Figure 6.9 shows a representative image of the ultimate failure appearance, and load versus displacement results are plotted in Figure 6.10. After yielding, the Type 1 specimens reloaded, but rather than pulling out, ultimate failure of the braid occurred when the failure load of the rebar was reached. Specimens exhibiting Type 1 failure were observed for all three L_d values tested (30, 50, and 70 mm). For the specimens with an L_d of 50, the observed failure mode was consistent with the predictions made in Section 6.5.2. The three 30 mm specimens that failed in this manner all exhibited yielding away from the end tab containing the discontinuity, which explains why these specimens exhibited ultimate tensile failure, rather than pullout.

It should be noted that specimen P6 showed greater elongations than the rest of the specimens. This was simply because this specimen was manufactured with a longer gage length than the 40 mm used for the other tests. This specimen was the only one with an L_d of 70 mm, and experienced failure consistent with the predictions in Section 6.5.2.

Figure 6.9: Example of Type 1 failure appearance

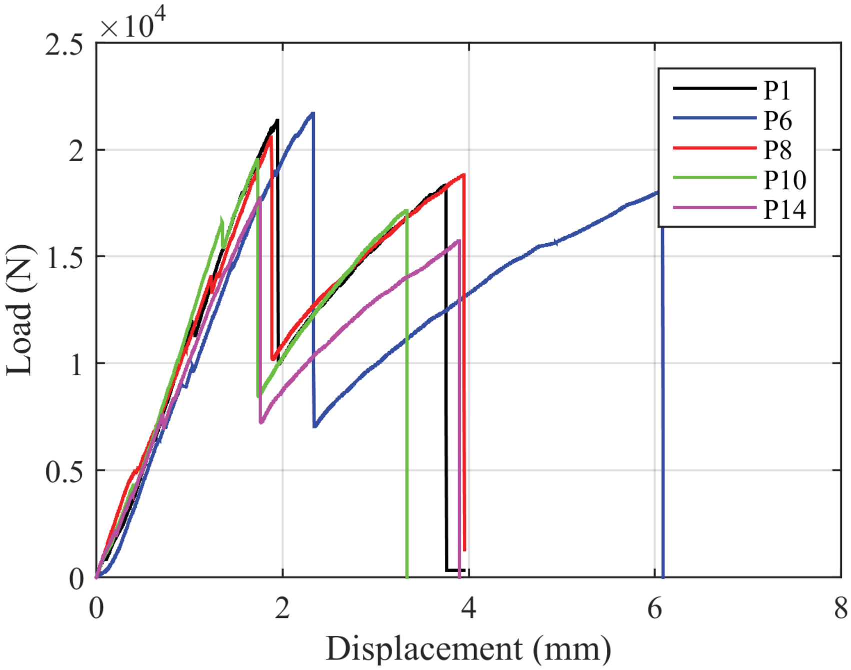

Figure 6.10: Tensile test results showing Type 1 failure

Type 2 failure occurred when the rebar failed catastrophically at the discontinuity location, inside the potted end. Figure 6.11 shows an example of one of these failures. Type 2 failure occurred in five specimens with L_d values of either 30 or 50 mm. Load versus displacement plots for these failures are shown in Figure 6.12. Because failure of the core occurred in a location where the braid had been cut, the rebar failed completely, with the load dropping to zero, rather than yielding and allowing the braid to reload. The reloading observed after this catastrophic failure was simply due to the potting resin re-anchoring itself inside the end tab, before eventually pulling out of the tube. The potting resin left bonded to the failed rebar can be seen in Figure 6.11. Type 2 failure likely occurred due to the presence of stress concentrations caused during the process of cutting the braid. Damage to the core would lead to failure initiation at this location, rather than in the rebar gage length.

Figure 6.11: Example of Type 2 failure appearance

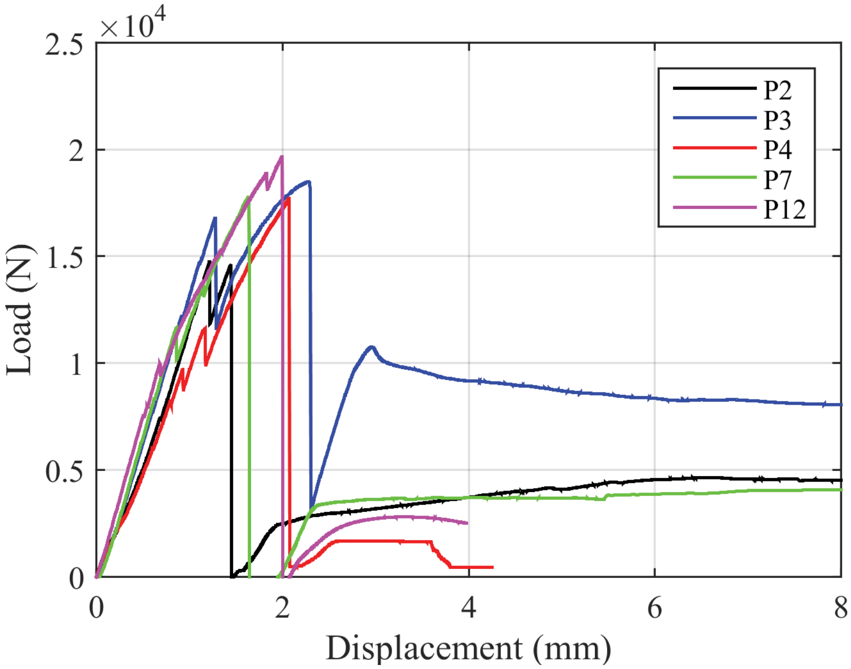

Figure 6.12: Tensile test results showing Type 2 failure

Type 3 failure represents the desired failure behavior of the rebar, and was similar to the mechanism proposed in Section 6.3. An image taken after the completion of pullout in specimen P5 is shown in Figure 6.13. In this figure, the pulled out braid and part of the pulled out core can be seen. Three specimens, all with L_d values of 30 mm failed in this manner; Figure 6.14 shows the load versus displacement plots for these specimens. Load increased linearly until yielding, causing a load drop. The rebar then began to reload before finally experiencing pullout, preventing catastrophic final failure.

Of the three specimens, sample P5 performed the best, showing a significant amount of reloading before pullout. Sample P9 showed very little reloading, and P13 showed almost no reloading before pulling out. Samples P9 and P13 also exhibited a larger load drop at yielding than other samples tested. Table 6.4 summarizes the loads observed during yielding and pullout of the three specimens.

The variations in results can be explained based on the yield locations in these rebar. In specimen P5, the yield point was near the center of the gage length, resulting in a longer embedded length of the core in the braid and therefore a relatively high pullout load. Specimen P9 yielded inside the potted portion of the bar, at a distance of only 20 mm from the braid discontinuity. This led to a decrease in the pullout load, as is reflected in the test results. Sample 13 yielded even closer to the discontinuity, (15 mm away) leading to pullout with virtually no reloading whatsoever. The experimental pullout loads were all smaller than the predicted values, which may be due to debonding of the core/braid interface during yielding, leading to a shorter effective embedded length of the core. Another factor may be fracture of the potting resin during pullout as shown in Figure 6.13. This was observed in all three specimens, and led to a smaller effective embedded length of the braid, further decreasing the pullout load.

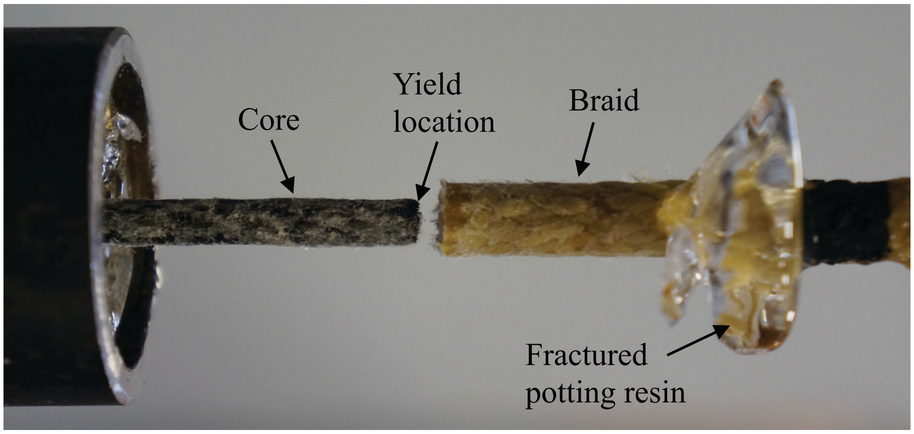

Figure 6.13: Example of Type 3 failure appearance

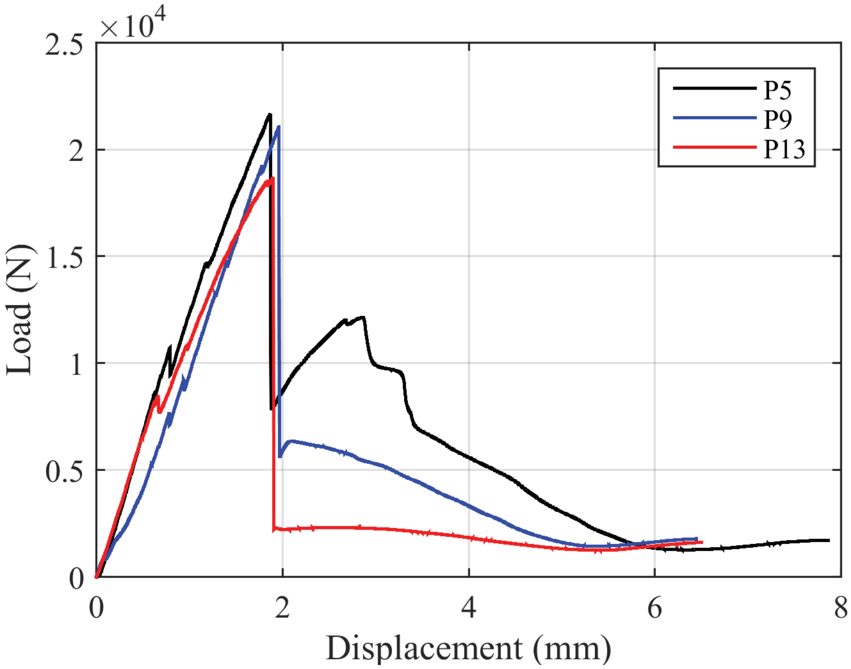

Figure 6.14: Tensile test results showing Type 3 failure

Table 6.4: Comparison of loading in Type 3 specimens

Sample	Yield Load (kN)	Dropped Load (kN)	Pullout Load (kN)
P5	21.6	10.4	12.1
P9	21.1	5.6	6.3
P13	18.7	2.2	2.3
Average	**20.5**	**6.1**	**6.9**
Std Dev	**1.6**	**4.1**	**4.9**

Type 4 failure occurred in a single specimen with an L_d value of 30 mm; the load-displacement plot is shown in Figure 6.16. In this failure type, yielding of the carbon core occurred in the gage length, and led to a large load drop to near 0 N followed by reloading with similar stiffness to the initial loading step. At a given point, the stiffness decreased, and loading continued up to a maximum value, at which point pullout began leading to decreasing load. However, the pullout in this specimen did not occur at the rebar interfaces, instead, pullout occurred at the interface between the potting resin and the steel tube, resulting in the entire potted end pulling out of the steel tube, as shown in Figure 6.15.

This result was unexpected, and the reasons behind this failure type cannot be fully explained at this stage. Poor bonding between the potting resin and the steel tube, as evident by the surface condition of the pulled-out resin, may have contributed to the initiation of the pullout. Despite this unexpected behavior, the general shape of the tensile plot during reloading and pullout resembles the tensile behavior of a ductile material such as steel. This may be due in part to much larger interfacial area involved in this pullout, which suggests that different rebar diameters may have a large effect on the pullout properties. If this type of failure mode can be fully understood and replicated within the rebar structure, this could lead to an ideal pseudoductile composite. Future work is required to try to replicate this type of failure and determine the mechanism behind it.

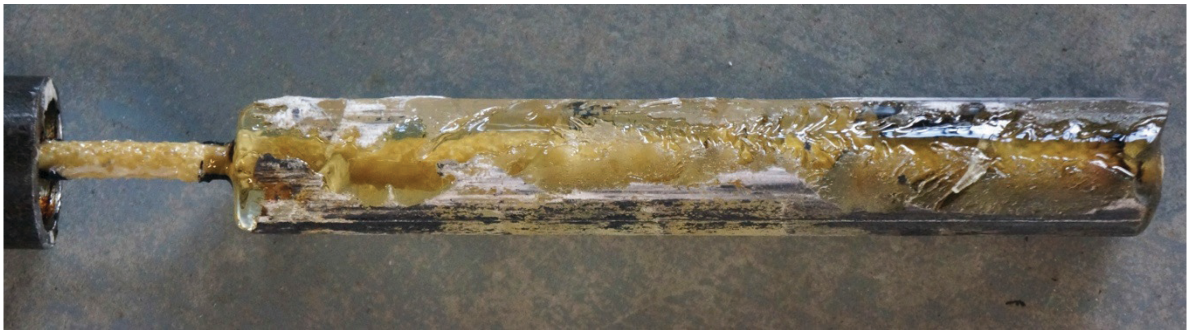

Figure 6.15: Type 4 failure appearance

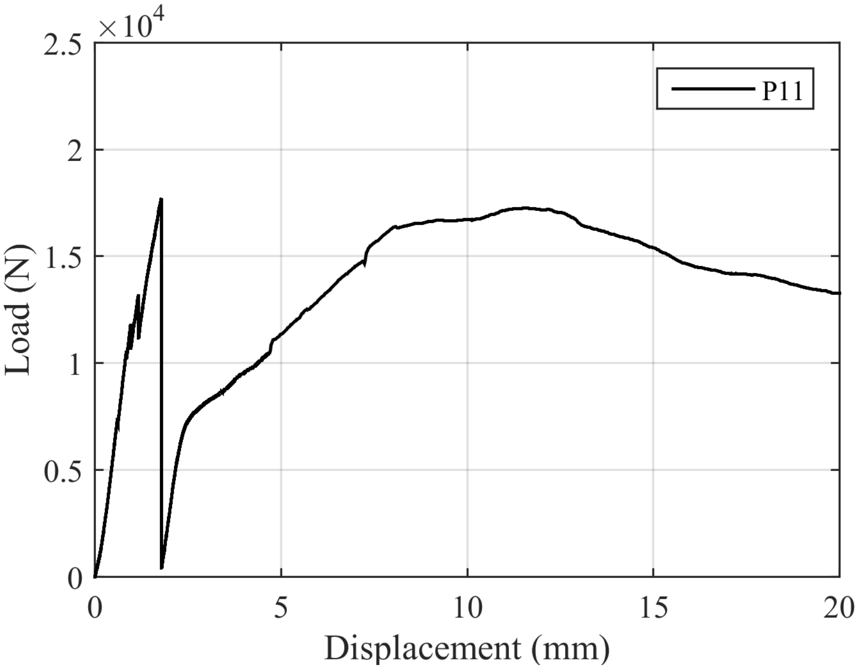

Figure 6.16: Tensile test results showing Type 4 failure

6.5.4 Evaluation of Discontinuous Rebar Design

The discontinuous rebar design showed promise as a method of enhancing pseudoductility in the hybrid FRP rebar developed for this thesis. While the proposed failure mechanism described in Section 6.3 was only seen in a small number of samples, these tests provided proof-of-concept for the pullout mechanism, and serve as a foundation on which to build towards the future. In samples that did experience pullout, failure was more gradual and better controlled than in previous work by Ewen dealing with a similar pullout mechanism [4].

Additional work is required to further refine the rebar design to improve the consistency and predictability of the failure mechanism. In its current state, the main limitation of the rebar design is that the location of the yield point in the rebar cannot be accurately controlled. The current design relies on the location of crack formation to initiate failure, and in a real-world scenario, cracks may not be formed at the correct locations to produce optimal pullout behavior. In addition, yielding was observed to not only occur in the exposed gage length of the rebar, but also inside the potted lengths, leading to unpredictable failure behaviors. To remedy this problem, future rebar designs may incorporate a method to initiate yielding at a specified location relative to the discontinuities, resulting in improved consistency in mechanical performance. Improvements can also be made to the interfacial properties between the core and braid in the rebar structure, as this interface is crucial to the magnitude and consistency of pullout loads. Further study is necessary to better understand the effect of yielding on the quality of this interface, and how it affects the pullout properties of the rebar.

Further pullout and tensile testing of the rebar should also be conducted using concrete as a potting medium. While the current setup using epoxy in the end tabs allows for the general failure mechanism to be more easily tested, the pullout performance of the rebar embedded in concrete should also be quantified, as differences in the bonding properties will have an effect on the pullout mechanism.

6.6 CONCLUSIONS

In this chapter, a method was introduced to improve the pseudoductility of the hybrid FRP rebar by incorporating a pullout mechanism after yielding. The pullout mechanism presented in this chapter shows promise as a method of extending the pseudoductility of hybrid FRP composite rebar by introducing discontinuities in the braid structure. Under ideal conditions combining the hybrid effect with pullout prevented brittle ultimate failure of the rebar, allowing for a more ductile failure mode.

Pullout testing was conducted to determine the interfacial properties of the core/braid and braid/potting interfaces. Using the results of these tests, tensile tests were designed to assess the viability of the proposed failure mechanism of the discontinuous rebar. Specimens were manufactured with discontinuity lengths of 30, 50, and 70 mm, and were subjected to tensile testing. Four different types of failures were observed, with only three of the test specimens failing as described by the proposed mechanism.

Examination of the failed specimens revealed that the choice of length between discontinuities is crucial to the pullout behavior and helps to determine the ultimate failure mode of the composite. If this length is too long, the rebar will fracture rather than pullout, and if it is too short, the composite will not experience reloading after yielding. The location of yielding also had an important effect on the final pullout behavior, and in the current rebar configuration, this location was unable to be accurately controlled, leading to inconsistent failure behavior in samples with the same discontinuity length. By controlling the location of the yield point relative to the discontinuities, the pullout mechanism may be able to be refined such that it is predictable and repeatable.

6.7 REFERENCES

[1] Hampton, F., 2004, "Cyclic Behavior, Development, and Characteristics of a Ductile Hybrid Fiber Reinforced Polymer (DHFRP) for Reinforced Concrete Members," Drexel University. United States.

[2] Somboonsong, W., Ko, F. K., and Harris, H. G., 1998, "Ductile Hybrid Fiber Reinforced Plastic Reinforcing Bar for Composite Structures: Design Methodology," ACI Materials Journal, **95**(6) pp. 655-666.

[3] Pastore, C., Armstrong-Carroll, E., and Ko, F., 2012, "Effect of Yarn Size on the Performance of Hybrid Braided Composite Rebar," The Masterbuilder, pp. 234-244.

[4] Ewen, K., 2005, "Ductility in FRP Rods for Concrete Reinforcement by Interfacial Shearing," University of Ottawa. Canada.

[5] Czel, G., Jalalvand, M., and Wisnam, M. R., 2015, "Demonstration of Pseudo-Ductility in Unidirectional Hybrid Composites made of Discontinuous Carbon/Epoxy and Continuous Glass/Epoxy Plies," Composites: Part A, **72**pp. 75-84.

[6] Kelly, A., and Tyson, W.R., 1965, "High Strength Materials,"Wiley and Sons Inc., New York, NY, pp. 578.

[7] Blau, P.J., 1992, "ASM Handbook Volume 18: Friction, Lubrication, and Wear Technology," ASM International.

7 CONCLUSIONS & FUTURE WORK

7.1 CONCLUSIONS

The primary objective of this thesis was to develop fiber reinforced polymer rebar with a high elastic modulus and a pseudoductile failure mode. The research included design, manufacturing, characterization, mechanical testing, and analytical modeling of the rebar tensile response. Pseudoductile fiber reinforced polymer rebar consisting of a unidirectional carbon fiber core and braided aramid fiber overwrap was successfully developed. The rebar design combined material and structural hybridization to achieve the desired pseudoductile behavior.

A unique dieless braidtrusion process combining aspects of braiding and pultrusion was developed to manufacture the fiber reinforced polymer rebar. The process allowed for high quality rebar to be consistently produced in a continuous manner. The resulting rebar geometry, including braid angle, core area, and braid area, was characterized, and was successfully predicted using analytical equations based on manufacturing parameters. The rebar produced for this thesis had a nominal outer diameter of 6.5 mm and a braid angle of 20.7°, and exhibited a high degree of cure (>99%) as confirmed by differential scanning calorimetry. Optical microscopy revealed that the braid was in the jammed state, and the jamming diameter was greater than the diameter of the core, resulting in a resin-only interfacial region between the core and the braid. Good fiber wetting was achieved throughout the rebar structure, and average fiber volume fractions of 0.465 and 0.711 were measured by image analysis in the core and braid respectively. The information gained from structural characterization was essential to the prediction of rebar mechanical properties and failure mechanism.

Tensile testing of the rebar specimens showed the expected pseudoductile failure behavior consisting of linear elastic loading, followed by a load drop due to failure of the core yarns (yielding), then subsequent reloading of the rebar until ultimate failure of the braid yarns. The rebar exhibited an initial elastic modulus of 84.2 ± 7.5 GPa, and yield strength of 782 ± 27 MPa at a strain of 0.0093 ± 0.0005 mm/mm. Analysis by optical strain measurement revealed local strain variations in the rebar gage length after yielding, which were found to limit the pseudoductility of the rebar.

Two analytical models were developed to predict the tensile properties of the rebar based on manufacturing parameters and material properties. The first model considered the rebar as a laminate to calculate elastic properties, and assumed uniform strain over the entire rebar gage length. After yielding, it was assumed that rebar properties were dominated by the braid. The second model considered the rebar after yielding as a series of springs, with mechanical properties depending on the elongation and stiffness of each spring. By taking into account the local strain variations in the rebar, the spring model resulted in improved prediction of failure strain. Using the spring model, a predicted failure strain of 0.175 mm/min was obtained, which was in good agreement with the average experimental value of 0.0164 ± 0.0027 mm/min. Both models successfully predicted the elastic modulus and yield point of the rebar.

A method was proposed for enhancing the pseudoductility of the hybrid fiber reinforced polymer rebar by incorporating a pullout mechanism after yielding. Discontinuities were added to the braided overwrap to initiate progressive pullout behavior prior to ultimate failure of the rebar. Pullout testing was conducted to determine the interfacial properties of the core/braid and braid/potting interfaces; these properties were used to guide the selection of discontinuity length. Tensile tests were conducted and showed inconsistent results with only three of fourteen specimens exhibiting the desired pullout behavior. It was found that the yielding location and discontinuity length both had an important impact on pullout properties, and dictated the failure mode of the rebar. Because the yielding location could not be accurately controlled, tensile test results were inconsistent, however, when yielding occurred in favorable locations, the results showed promise as a viable method for enhancing pseudoductility of the rebar.

This research may have significant implications to the reinforced concrete industry. Improving the pseudoductile characteristics of FRP rebar may lead to increased adoption of FRP materials in the place of conventional steel rebar, resulting in greater longevity of reinforced concrete structures in environments that promote corrosion in conventional steel rebar. The steps taken in this thesis towards the design, manufacturing, modeling, and characterization of pseudoductile FRP rebar provide important information that can serve as a foundation upon which to base future studies.

7.2 FUTURE WORK

This work provides an important foundation upon which to build future studies. Further research is required to improve the mechanisms for pseudoductility shown in this thesis, and to generalize the findings for different variations of the rebar design. Recommendations for the direction of future work are presented in this section.

In this thesis, research was focused on a single rebar architecture. Further study should be conducted on rebar produced using different fiber and matrix combinations, rebar diameters, braid angles, and different proportions of core and braid structures. This will help to further validate the analytical models and determine the effects of various material and geometrical parameters on the mechanical properties of the rebar. In particular, changing rebar diameter is expected to influence the yield and ultimate strength of the rebar, due to shear lag in the rebar cross-section.

Improvements can be made to the dieless braidtrusion process by fully automating the system for better control and consistency of the rebar architecture, reducing the possibility for variations between production runs due to operator error. Modifications to the impregnation and curing processes may also help to reduce or eliminate drips from the outer surface of the rebar, leading to a cleaner, more consistent rebar surface.

Analytical modeling of the rebar tensile properties could be further improved by incorporating undulations and curvature of the braid into the elastic modulus predictions. For the spring model, additional work is needed to predict the effective spring lengths in the rebar after yielding. The current model uses experimental data to approximate these lengths; ideally this could be done based on material properties and geometric parameters of the rebar.

Additional work can also be done to minimize the load drop during yielding, leading to a smooth stress-strain curve to failure. This may be achieved by inducing multiple fractures in the core, as opposed to the core yielding at a single location. This concept has been successfully applied to laminated hybrid composites, and may also be applicable to the fiber reinforced polymer rebar.

To improve the consistency and predictability of the pullout mechanism for enhanced pseudoductility, more work is required to accurately control the yielding location in the rebar. A better method is also needed for adding discontinuities to the braided overwrap without inducing stress concentrations. Further study and replication of the unexpected failure observed in specimen P11 should also be done to determine whether this mechanism can be used for future improvements in pseudoductility. In this test, the entire potted test specimen pulled out of the end tab, resulting in load-displacement behavior similar to that of a ductile material.

Finally, in addition to tensile testing of the rebar specimens themselves, more work is needed in order to understand how the mechanical properties of the rebar translate to a reinforced concrete structure. To do this, pullout tests of the rebar in concrete should be conducted in order to assess the bond strength and determine the development length of the rebar. Future mechanical testing of concrete members reinforced with the pseudoductile fiber reinforced polymer rebar can also be done to examine how the properties of the rebar translate to the reinforced structure as a whole. Results should be compared to those for members reinforced with steel and conventional fiber reinforced polymer rebar.

BIBLIOGRAPHY

ACI Committee Report, "ACI 440.1R-06, Guide for the Design and Construction of Structural Concrete Reinforced with FRP Bars," pp. 1-44.

ACI Committee Report, "ACI 440.3R-04 Guide Test Methods for Fiber-Reinforced Polymers (FRPs) for Reinforcing Or Strengthening Concrete Structures," pp.1-40.

ACI Educational Bulletin, "E2-00 Reinforcement for Concrete - Materials and Applications," pp. 1-16.

Agarwal, B.D., and Broutman, L.J., 1990, "Analysis and Performance of Fiber Composites, Second Edition," John Wiley & Sons, New York, NY.

Ahmadi, M. S., Johari, M. S., Sadighi, M., 2009, "An Experimental Study on Mechanical Properties of GFRP Braid-Pultruded Composite Rods," Express Polymer Letters, **3**(9) pp. 560-568.

Alpyildiz, T., 2012, "3D Geometrical Modeling of Tubular Braids," Textile Research Journal, **82**(5) pp. 443-453.

ASTM International, 2013, "ASTM C1557 - 03 Standard Test Method for Tensile Strength and Young's Modulus of Fibers," pp.1-10.

ASTM International, 2011, "ASTM D7205/D7205M-06 Standard Test Method for Tensile Properties of Fiber Reinforced Polymer Matrix Composite Bars," pp.1-13.

ASTM International, 2011, "ASTM D3171 - 11 Standard Test Method for Constituent Content of Composite Materials," pp. 1-11.

Aveston, J., and Kelly, A., 1980, "Tensile First Cracking Strain and Strength of Hybrid Composites and Laminates," Physical Sciences, **294**(1411) pp. 519-534.

Ayranci, C., and Carey, J., 2008, "2D Braided Composites: A Review for Stiffness Critical Applications," Composite Structures, **85**pp. 43-58.

Ayranci, C., and Carey, J. P., 2010, "Predicting the Longitudinal Elastic Modulus of Braided Tubular Composites using a Curved Unit-Cell Geometry," Composites: Part B, **41**pp. 229-235.

Bakis, C. E., Nanni, A., Terosky, J. A., 2001, "Self-Monitoring, Pseudo-Ductile, Hybrid FRP Reinforcement Rods for Concrete Applications," Composites Science and Technology, **61**pp. 815-823.

Bank, L., 2013, "Progressive Failure and Ductility of FRP Composites for Construction: Review," Journal of Composites for Construction, **17**pp. 406-419.

Blau, P.J., 1992, "ASM Handbook Volume 18: Friction, Lubrication, and Wear Technology," ASM International.

Bunsell, A. R., and Harris, B., 1974, "Hybrid Carbon and Glass Fibre Composites," Composites, pp. 157-164.

Busel, J. P., 2012, "Fiber Reinforced Polymer (FRP) Composite Rebar," American Composites Manufacturers Association (ACMA), .

Byun, J., 2000, "The Analytical Characterization of 2-D Braided Textile Composites," Composites Science and Technology, **60**pp. 705-716.

Czel, G., Jalalvand, M., and Wisnam, M. R., 2015, "Demonstration of Pseudo-Ductility in Unidirectional Hybrid Composites made of Discontinuous carbon/epoxy and Continuous glass/epoxy Plies," Composites: Part A,**72**pp. 75-84.

Czel, G., and Wisnom, M., 2013, "Demonstration of Pseudo-Ductility in High Performance glass/epoxy Composites by Hybridisation with Thin-Ply Carbon Prepreg," Composites: Part A, **52**pp. 23-30.

Du, G., and Popper, P., 1994, "Analysis of a Circular Braiding Process for Complex Shapes," The Journal of the Textile Institute, **85**(3) pp. 316-337.

DuPont, "Technical Guide: Kevlar Aramid Fiber".

El-Tahan, M., Galal, K., and Hoa, V. S., 2013, "New Thermoplastic CFRP Bendable Rebars for Reinforcing Strutural Concrete Elements," Composites: Part B, **45**pp. 1207-1215.

Elzafraney, M., and Soroushian, P., 2006, "Testing Techniques and Tools to Determine Properties of Fiber-Reinforced Rods," Journal of Testing and Evaluation, **34**(2) pp. 1-8.

Ewen, K., 2005, "Ductility in FRP Rods for Concrete Reinforcement by Interfacial Shearing," University of Ottawa. Canada.

Fangueiro, R., Sousa, G., Soutinho, F., 2006, "Application of Braided Fibre Reinforced Composite Rods in Concrete Reinforcement," Materials Science Forum, **514-516**pp. 1556-1560.

Frank, S., and Spolenak, R., "Optical Strain Measurement by Digital Image Analysis," Http://www.Mathworks.com/matlabcentral/fx_files/20438/1/content/Documentation.Htm.

Hajihosseini, A., 2013, "Numerical Simulation of the Curing Process of Fiber Reinforced Polymer Composites," Blekinge Institute of Technology.

Hajihosseini, A., Ayranci, C., and Carey, J. P. R., 2014, "Simulation of the rapid curing process for braid reinforced FRP rebar in braidtrusion process using a finite element analysis," SAMPE Conference Proceedings, Anonymous Seattle, WA.

Hamada, H., Kameo, K., Sakaguchi, M., 2000, "Energy-Absorption Properties of Braided Composite Rods," Composites Science and Technology, **60**pp. 723-729.

Hampton, F., 2004, "Cyclic Behavior, Development, and Characteristics of a Ductile Hybrid Fiber Reinforced Polymer (DHFRP) for Reinforced Concrete Members," Drexel University. United States.

Hampton, F. P., Ko, F. K., Doyle, C., 2009, "Development of ductile-hybrid composites (DHC) by the braidtrusion process," 17th International Conference on Composite Materials, Anonymous Edinburgh, UK.

Harris, H. G., Somboonsong, W., and Ko, F. K., 1998, "New Ductile Hybrid FRP Reinforcing Bar for Concrete Structures," Journal of Composites for Construction, **2**pp. 28-37.

Hoa, S.V., 2009, "Principles of the Manufacturing of Composite Materials,"DEStech Publications, pp. 233-245, Chap. 6.

Hoa, S.V., 2009, "Principles of the Manufacturing of Composite Materials,"DEStech Publications, pp. 45-98, Chap. 2.

ISIS Canada, 2006, "ISIS Educational Module 3: An Introduction to FRP-Reinforced Concrete" pp.1-34.

ISIS Canada, 2006, "ISIS Educational Module 2: An Introduction to FRP Composites for Construction" pp.1-25.

Kaw, A.K., 2006, "Mechanics of Composite Materials, Second Edition," Taylor & Francis Group, Boca Raton, FL, .

Kelly, A., and Tyson, W.R., 1965, "High Strength Materials,"Wiley and Sons Inc., New York, NY, pp. 578.

Ko, F., Head, A., and Pastore, C., 1989, "Handbook of Industrial Braiding," Atkins and Pearce, Covington, Kentucky.

Ko, F.K., 2001, "ASM Handbook, Volume 21: Composites,"ASM International, pp. 70-77, Chap. Braiding.

Lebel, L. L., and Nakai, A., 2012, "Design and Manufacturing of an L-Shaped Thermoplastic Composite Beam by Braid-Trusion," Composites: Part A, **43**pp. 1717-1729.

Leung, C. K., Melenka, G. W., Nobes, D. S., 2013, "The Effect on Elastic Modulus of Rigid-Matrix Tubular Composite Braid Radius and Braid Angle Change Under Tensile Loading," Composite Structures, **100**pp. 135-143.

Lindau Chemicals Inc., 2002, "Technical Data Sheet, Epoxy Resin System for Pultrusion: LS-81K Anhydride Curing Agent," pp. 1-6.

Michaeli, W., and Jurss, D., 1996, "Thermoplastic Pull-Braiding: Pultrusion of Profiles with Braided Fibre Lay-Up and Thermoplastic Matrix System (PP)," Composites: Part A, **27A**pp. 3-7.

Milwich, M., 2009, "Thermoplastic braid pultrusion," Proceedings of ICCM 17, Anonymous Edinburgh, UK.

Momentive, 2005, "Technical Data Sheet: EPON Resin 826," pp. 1-3.

Mutlur, S., 2004, "Advanced Topics in Characterization of Composites,"Trafford Publishing, pp. 11-33.

Pastore, C., Armstrong-Carroll, E., and Ko, F., 2012, "Effect of Yarn Size on the Performance of Hybrid Braided Composite Rebar," The Masterbuilder, pp. 234-244.

Pastore, C.M., and Ko, F.K., 1999, "Braided Hybrid Composites for Bridge Repair," National Textile Annual Report, F98-P01, .

Poisson, E., 2009, "Automation of Continuous Composite 2D Braiding Process," University of Ottawa. Canada.

Poisson, E., Fahim, A., and Munro, M., 2008, "Automated pilot plant production of continuous fiber composite rods," Canadian Society for Mechanical Engineering Forum.

Potyrala, P. B., 2011, "Use of Fibre Reinforced Polymer Composites in Bridge Construction. State of the Art in Hybrid and all-Composite Structures,".

Quek, S. C., Waas, A. M., Shahwan, K. W., 2003, "Analysis of 2D Triaxial Flat Braided Textile Composites," International Journal of Mechanical Sciences, **45**pp. 1077-1096.

Sandess, J., Fahim, A., and Munro, M., 2008, "Rapid curing of 25 mm diameter continuous fibre composite rods," Canadian Society for Mechanical Engineering Forum.

Sandness, J., 2008, "The Optimization of the Curing of Carbon Composite Rebar using Heat Transfer FEA Model," University of Ottawa. Canada.

Sichina, W.J., 2000, "Characterization of epoxy resins using DSC," PerkinElmer Instruments.

Sika Canada, 2012, "Product Data Sheet: Sikadur 35 Hi-Mod LV,".

Somboonsong, W., Ko, F. K., and Harris, H. G., 1998, "Ductile Hybrid Fiber Reinforced Plastic Reinforcing Bar for Composite Structures: Design Methodology," ACI Materials Journal, **95**(6) pp. 655-666.

Strong, B.A., 2008, "Fundamentals of Composites Manufacturing - Materials, Methods, and Applications (2nd Edition),"Society of Manufacturing Engineers (SME), pp. 453-461, Chap. 18.

Subramanian, N., 2013, "Design of Reinforced Concrete Structures,"Oxford University Press, pp. 142-213, Chap. 5.

Subramanian, N., 2013, "Design of Reinforced Concrete Structures,"Oxford University Press, pp. 1-44, Chap. 1.

TA Instruments, "Characterization of the degree of cure of thermosetting resins by DSC," TA Instruments.

Toho Tenax America, I., 2014, "Safety Data Sheet SDS no. 0503 Rev L".

Toho Tenax America, I., 2009, "Tenax Carbon Fibers".

Weggel, D. C., Boyajian, D. M., and Chen, S., 2007, "Modelling Structures as Systems of Springs," World Transactions on Engineering and Technology Education, **6**(1) pp. 169-172.

Xiong, G., 2006, "Local Adaptive Thresholding".

You, Y., Kim, J., Kim, S., 2015, "Methods to Enhance the Guaranteed Tensile Strength of GFRP Rebar to 900 MPa with General Fiber Volume Fraction," Construction and Building Materials, **75**pp. 54-62.

You, Y., Park, K., Seo, D., 2015, "Tensile Strength of GFRP Reinforcing Bars with Hollow Section," Advances in Materials Science and Engineering, pp. 1-8.

You, Y., Park, Y., Park, J., 2007, "Development of FRP rebar for concrete structures in Korea," FRPRCS-8, pp.1-8.

APPENDIX A: SINGLE FIBER TENSILE TESTING

A.1 INTRODUCTION

The carbon fibers used in this study were acquired second hand, and were labeled as Toho Tenax G50-500. While the properties of the matrix material and aramid fibers used in this study were well documented, official material property data for the carbon fibers was unavailable, therefore, tensile testing was performed on the fibers to determine their mechanical properties.

A.2 SINGLE FIBER EXTRACTION

Single carbon fibers were extracted from the available yarns. To separate individual fibers, yarns were first immersed in methanol for five minutes, then removed and allowed to air dry. This process promoted separation between the fibers, and allowed individual fibers to be more easily extracted. To extract the fibers, a piece of adhesive tape was used. By lightly touching the tape to the end of the treated yarn, and slowly pulling away, several carbon fibers could be extracted from the yarn. These fibers were further separated using the same technique until single fibers were obtained.

A.3 DIAMETER MEASUREMENT

Diameters of the single fibers were measured to allow for the cross-sectional areas of the fibers to be calculated. The area calculations were necessary to determine stress in the fibers during tensile testing and were based on a circular fiber cross section. Single fibers were imaged using an optical microscope (Olympus® BX61, Olympus, USA) at a magnification of 500x, as shown for example in Figure A.1. The images were imported into image analysis software (ImageJ), and fiber diameters were measured at five locations along the length of each fiber. Twelve different fibers were measured, resulting in a total of 60 measurements. The average measured fiber diameter was 7.5 ± 0.4 µm.

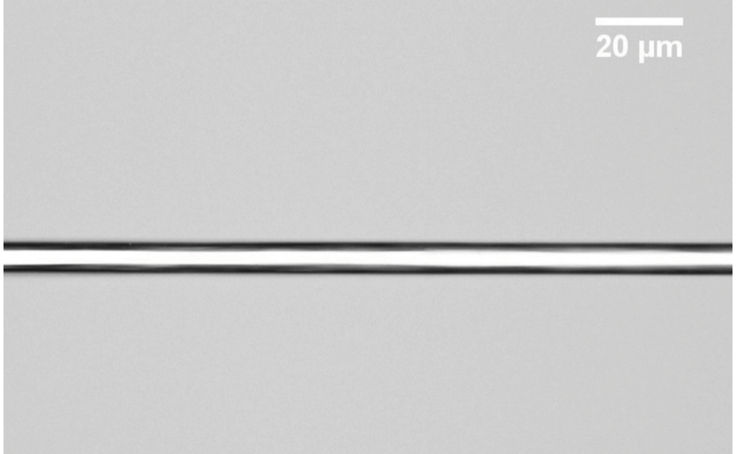

Figure A.1: Optical microscope image of a single carbon fiber for diameter measurement

A.4 TENSILE TESTING

Tensile testing was performed on single carbon fibers following ASTM 3822 [1] in order to confirm the tensile properties of the fibers. Single fibers were mounted onto paper templates, as shown in Figure A.2. An epoxy adhesive (KwikWeld, JB Weld, USA) was used to fix the fibers to the template, with a gage length of 1 inch (25.4 mm), and was allowed to cure for 24 hours before testing. The templates with mounted carbon fibers were then fixed into a tensile testing system (Electroforce® 3200, Bose, USA), equipped with a 500 g load cell. Before beginning to test, the template was cut on either side of the central hole to expose the fiber for testing. The fibers were pulled to failure, and load versus displacement data was recorded. Load was converted to stress by dividing by the fiber cross-sectional area. Strain was calculated by dividing the crosshead displacement by the original gage length of the fiber specimen. Compliance of the machine was assumed to be negligible as the applied loads were low (on the order of 20 g) and the cross-section of the grips was large relative to the fiber diameter. Plots of stress versus strain showed linear elastic behavior to failure, allowed for ultimate strength, ultimate strain, and elastic modulus to be found. Eighteen fibers were tested, with twelve fibers yielding successful results. The average mechanical properties (± standard deviation) of the fibers are summarized in Table A.1. The average properties reported here are used in this thesis for predicting mechanical properties of the manufactured FRP rebar.

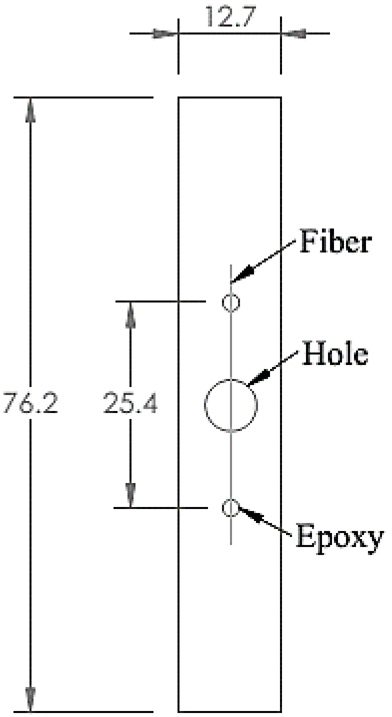

Figure A.2: Single fiber tensile test mounting template

Table A.1: Summary of average measured tensile properties for single carbon fibers

Ultimate Strength (MPa)	Ultimate Strain (mm/mm)	Elastic Modulus (GPa)
2780 ± 600	0.0099 ± 0.0018	28.4 ± 2.1

A.5 REFERENCES

[1] ASTM International, 2013, "ASTM C1557 - 03 Standard Test Method for Tensile Strength and Young's Modulus of Fibers," pp.1-10.

APPENDIX B: BRAIDLINE CALIBRATION

B.1 INTRODUCTION

During the braidtrusion process for FRP rebar production, it was important to accurately control the braid angle and production rate. In the current manufacturing process, this was done by independently setting the braiding and pulling speeds, by choosing an applied voltage. Both the braider and puller were equipped with encoders that allowed for the braiding and pulling speeds to be measured. These values were correlated with the applied voltages to create calibration curves relating the applied voltage to the braider rotational speed and pulling rate. The calibration tests were conducted when the system was fully loaded with core and braid yarns to ensure that speeds were recorded under true operating conditions.

B.2 BRAIDER CALIBRATION

Applied voltage to the braider was varied from 0.6 to 5.0 V and speeds were measured by the encoder in revolutions per minute (RPM). The measurements are summarized in Table B.1. A linear regression was performed on the data to find an equation to relate braiding speed in RPM to applied voltage, which was used to set braiding speed during production. The regression curve and equation is shown in Figure B.1. The curve fit the data well, with an R^2 value of 0.999.

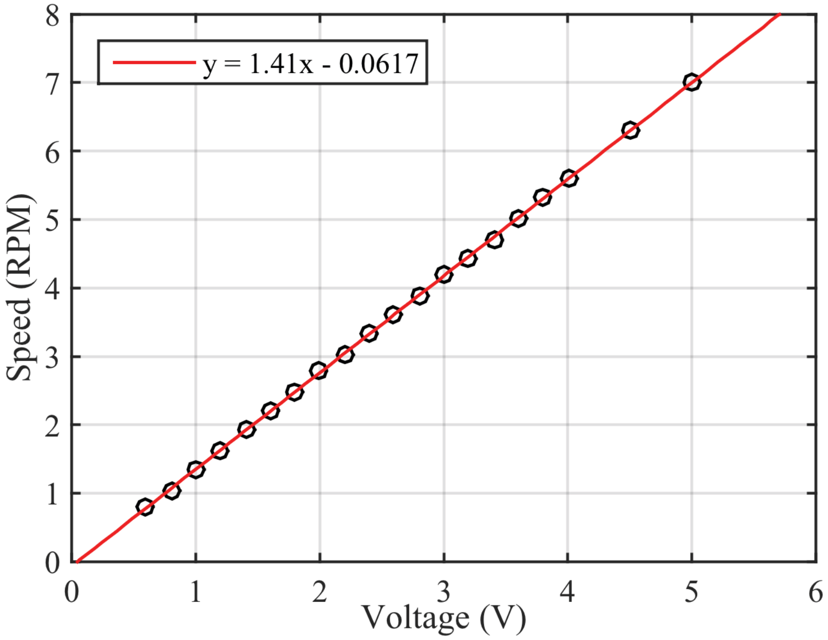

Figure B.1: Braider calibration curve

Table B.1: Braider calibration table

Voltage (V)	Speed (RPM)
0.6	0.80
0.8	1.05
1.0	1.35
1.2	1.63
1.4	1.93
1.6	2.20
1.8	2.48
2.0	2.78
2.2	3.03
2.4	3.35
2.6	3.60
2.8	3.89
3.0	4.18
3.2	4.43
3.4	4.72
3.6	5.03
3.8	5.31
4.0	5.59
4.5	6.30
5.0	7.01

B.3 PULLER CALIBRATION

Applied voltage to the puller was varied from 0.5 to 5.0 V in 0.5 V increments; speeds were measured by the encoder in mm/min. The resulting measurements are summarized in Table B.2. A linear regression was performed on the data as shown in Figure B.2, to generate an equation relating pulling speed to applied voltage. The resulting equation fit the data well, with an R^2 value of 0.996, and was used during production to set the rebar pulling speed.

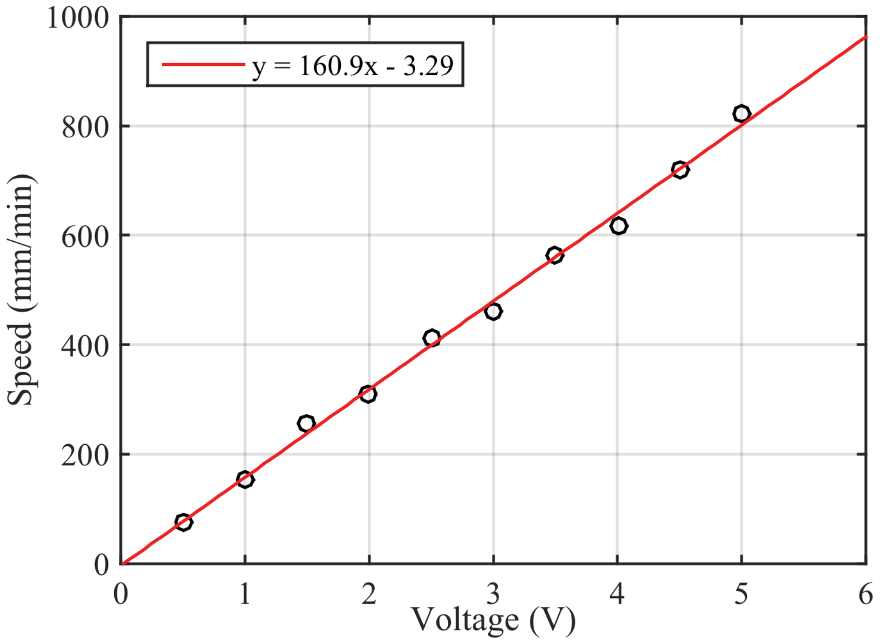

Figure B.2: Puller calibration curve

Table B.2: Puller calibration table

Voltage (V)	Speed (mm/min)
0.5	77.07
1.0	154.2
1.5	256.8
2.0	308.4
2.5	411.0
3.0	462.6
3.5	565.2
4.0	616.2
4.5	718.8
5.0	822.0

APPENDIX C: DEVELOPMENT OF IMPREGNATION PROCESS

C.1 INTRODUCTION

During the development of the braidtrusion process used in this study, two different impregnation configurations were attempted. This section details the two methods and presents the analytical methods used to assess the effectiveness of each method. Rebar produced by each method were compared using optical microscopy, SEM, burn-off testing, and pullout testing. Descriptions of the methods used for each of these tests can be found in throughout this thesis.

C.2 SINGLE IMPREGNATION METHOD

The initial configuration of the braidtrusion process used only a single impregnation step prior to braiding. The core yarns were pulled through an impregnation bath shown in Figure 4.2(a). A schematic of the impregnation bath is shown in Figure 4.2(b) for clarity. In this method, the core yarns are dipped into the pre-mixed resin and hardener via a series of rollers. The bath is heated to 40˚C in order to maximize pot life and lower the viscosity of the resin to promote good fiber wetting. This impregnation method relied on the assumption that during braiding, the braid yarns would apply pressure to the core, forcing any excess resin to be squeezed out of the core and into the dry braid yarns, thus impregnating the entire rebar structure.

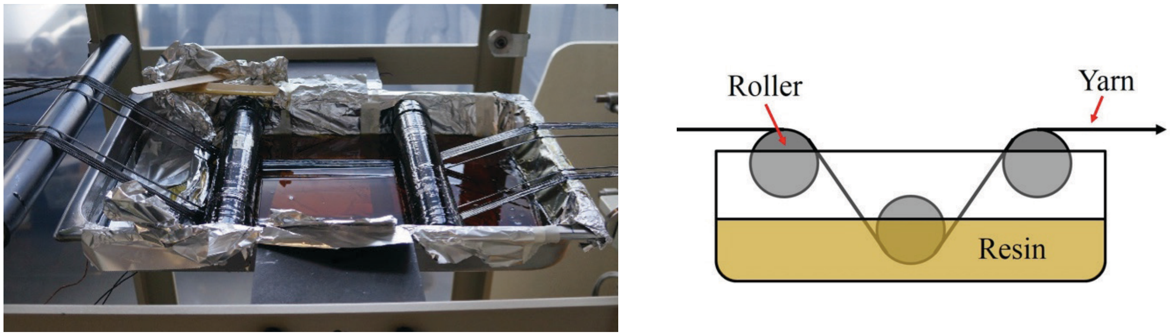

(a) (b)

Figure C.1: (a) Core yarns passing through impregnation bath, (b) schematic of impregnation bath

C.3 DUAL IMPREGNATION METHOD

The braidtrusion process was later modified to include two impregnation steps, resulting in the dual impregnation method. This configuration combined a resin bath and an impregnation ring in an attempt to improve impregnation quality of the final rebar structure. The first impregnation step remained the same as described for the single impregnation method, using a resin bath to impregnate the core yarns. The second impregnation step consisted of an impregnation ring, which wets the braid yarns before they converge on to the core, followed by rollers that wipe away excess resin and apply pressure to the outer surface of the braid. An overview of this impregnation step is shown in Figure 4.4.

In this process, the impregnation ring takes the place of the braid forming ring, and serves both purposes of impregnating the braid yarns and setting the convergence point of the braid. The impregnation ring consists of a steel ring with an internal cavity and holes evenly spaced around the inside circumference. Resin is pumped into an inlet, filling the cavity, and flows out of the holes into a circumferential groove on the inside of the ring. This causes the inner circumference of the ring to be saturated with resin. As the braiding process progresses, the braid yarns slide across the inner surface of the ring and are impregnated with resin. The braiding motion causes the braid yarns to rub back and forth against the ring, effectively massaging the resin into the yarns. Similar to the primary impregnation step, the resin is pre-mixed and heated to 40˚C before it is pumped into the ring by a peristaltic pump.

As shown in Figure C.3(a), impregnation by the ring leads to a large quantity of excess resin on the outer surface of the braid. To address this, the braid passes through a series of rollers, which apply pressure to the external surface of the braid and wipe away excess resin. Figure C.3(b) shows the rebar surface after having passed through the rollers. Excess resin from the impregnation process is captured, reheated, and recirculated to the impregnation ring.

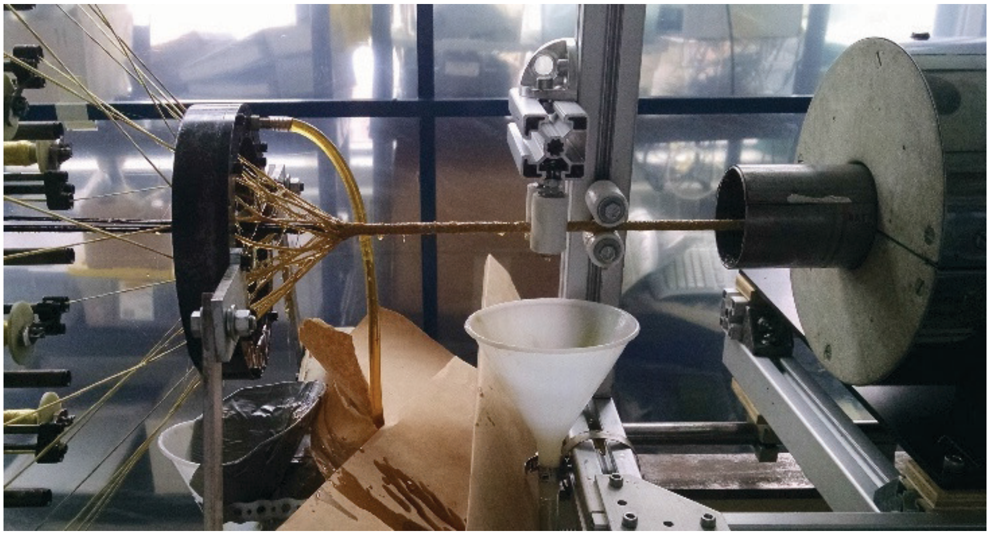

Figure C.2: Overview of dual impregnation step

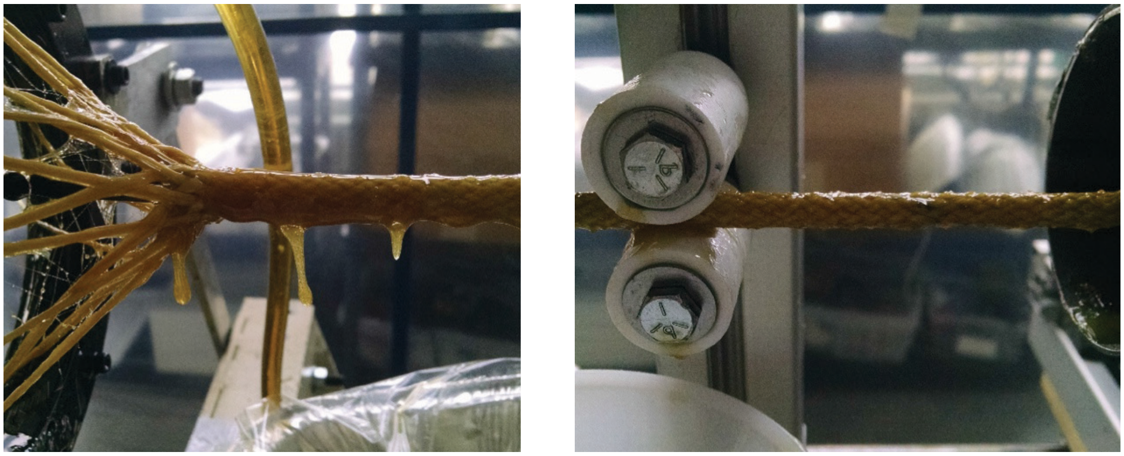

(a) (b)

Figure C.3: (a) Excess resin coating rebar surface after dual impregnation, (b) surface of rebar after passing through rollers, showing majority of excess resin removed

C.4 COMPARISON BETWEEN IMPREGNATION METHODS

Rebar manufactured by both the single and dual impregnation methods were compared to see if impregnation was improved from the addition of the secondary impregnation step. Macro and microstructural features were analyzed by optical microscopy, SEM, burn-off testing, and pullout testing.

C.4.1 Optical Microscopy

Figure C.4 shows a representative cross-sectional image of a rebar manufactured by single impregnation. The core is generally well consolidated and reasonably circular in shape. The shape of the braid is also circular, as expected. The interface between the core and braid, however, is not well consolidated, with large amounts of empty space between the two regions. This can be attributed to the jammed state of the braid, which limits its the minimum inner diameter [1]. With the current braid and core proportions, the minimum inner diameter of the braid is larger than the core diameter, causing a space at the core/braid interface. Closer examination of this interface reveals the presence of small resin-only "bridges" connecting the core and braid in select locations, as shown in Figure C.5(a). These bridges make up a relatively small part of the interface, with the majority consisting of large voids, as shown in Figure C.5(b).

A thin resin-only "shell" was also observed on the outside surface of the braid. This shell is thicker at locations where the braid undulations create valleys on the surface. Voids are also present in this shell, which are a result of the dieless curing process, and the fact that there is no pressure forcing the resin to fill these areas during curing. The presence of this shell implies that there was resin on the surface of the braid during curing, and that some of the resin that had impregnated the core yarns was passed to the braid yarns during the braiding process. However, micrographs (Figure C.6) reveal poor fiber wetting of the braid yarns, with individual fibers packed tightly together, with little to no resin between them. This means that the resin from the core is simply coating the braid yarns, rather than properly impregnating the yarns and wetting the individual fibers.

There are several factors that could be causing the poor impregnation of the braid yarns. Because the braid is in a jammed state, fibers in each individual yarn are tightly packed together [2], making it difficult for the resin to infiltrate between individual fibers. Also, since the inner diameter of the jammed braid was greater than the core diameter, tightening of the braid did not result in significant pressure on the core, thus excess resin could not be adequately forced into the braid yarns.

The microstructure of the core is shown in Figure C.7. Overall, the core was well impregnated and free of large voids, with excellent fiber wetting. The fiber distribution is good overall, however, some resin-rich regions were present. This may be due to the lack of pressure exerted on the core, due to the limitations on the inner diameter of the jammed braid.

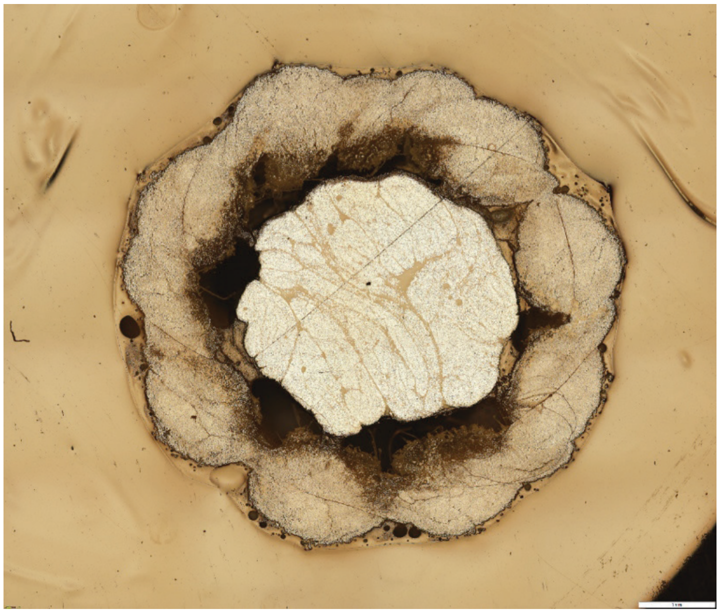

Figure C.4: Representative cross-section of rebar produced by single impregnation

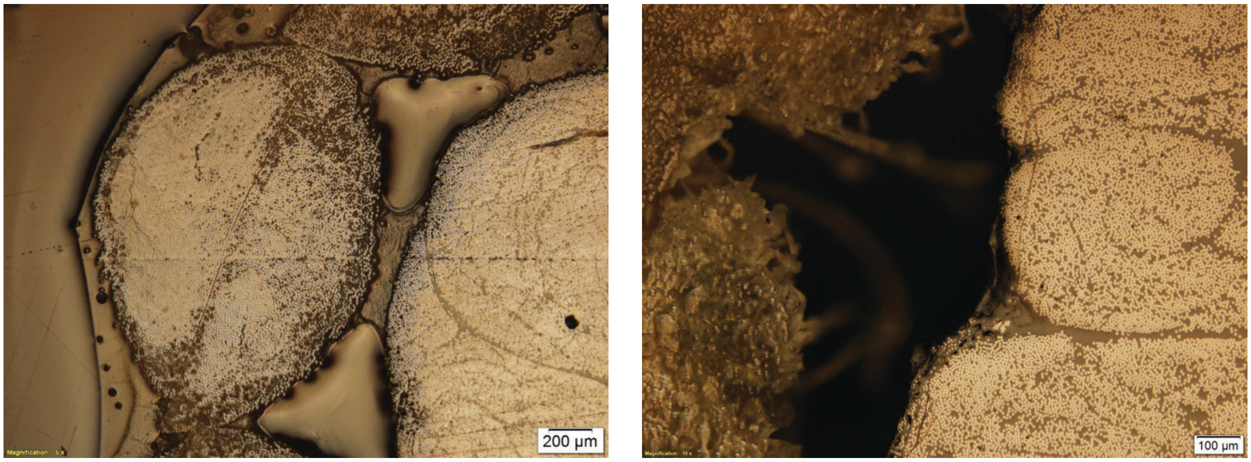

(a) (b)

Figure C.5: Closeup on core-braid interface, showing (a) small resin bridge connecting core and braid over interface, (b) large void separating core and braid

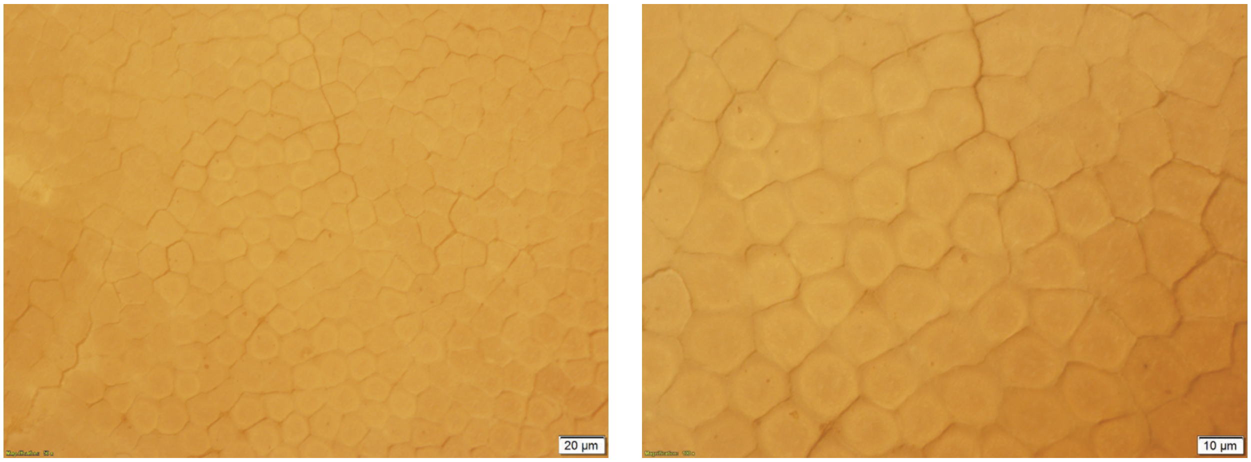

(a) (b)

Figure C.6: Representative microstructure of braid, showing dense fiber packing with little to no matrix present in between fibers

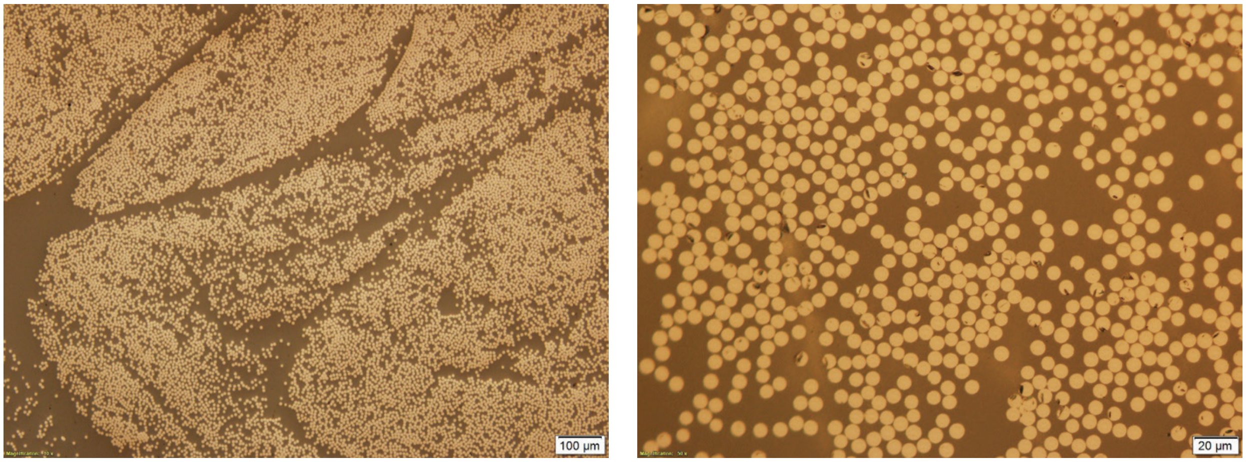

(a) (b)

Figure C.7: Representative images of core microstructure showing (a) resin rich regions present in the core, (b) good fiber wetting of individual carbon fibers in the core

Figure C.8 shows a representative micrograph of a rebar cross-section produced by dual impregnation. In this case, the majority of the braid/core interface is filled with matrix material, resulting in a better bond between the core and braid structures, which may lead to improved load transfer and make the rebar less susceptible to delamination. The shape of the core and braid remained relatively circular, however, at certain locations, the core was deformed to the shape of the inner surface of the braid as a likely result of external pressure applied by the rollers to help improve consolidation of the structure. The resin-only shell remained present in these specimens, and appeared to be larger than for the single impregnation specimens. This is likely due to the increased amount of resin used in the dual impregnation method.

Figure C.9 shows a close-up of the braid-core interface, which highlights the improved interface consisting mainly of matrix, with some small voids present. Figure C.10 shows the typical microstructure within the braid yarns, and reveals that the dual impregnation method succeeded in impregnating the braid, showing significant improvement over the single impregnation method. While the braid fibers remained fairly tightly packed when compared to the core, the majority of the braid fibers are surrounded by matrix, indicating generally good fiber wetting. The microstructure of the core remained relatively consistent between rebar produced by both impregnation methods. The core yarns were fully impregnated, with very good wetting of the carbon fibers and resin-rich pockets scattered throughout.

Figure C.8: Representative cross-section of rebar produced by dual impregnation

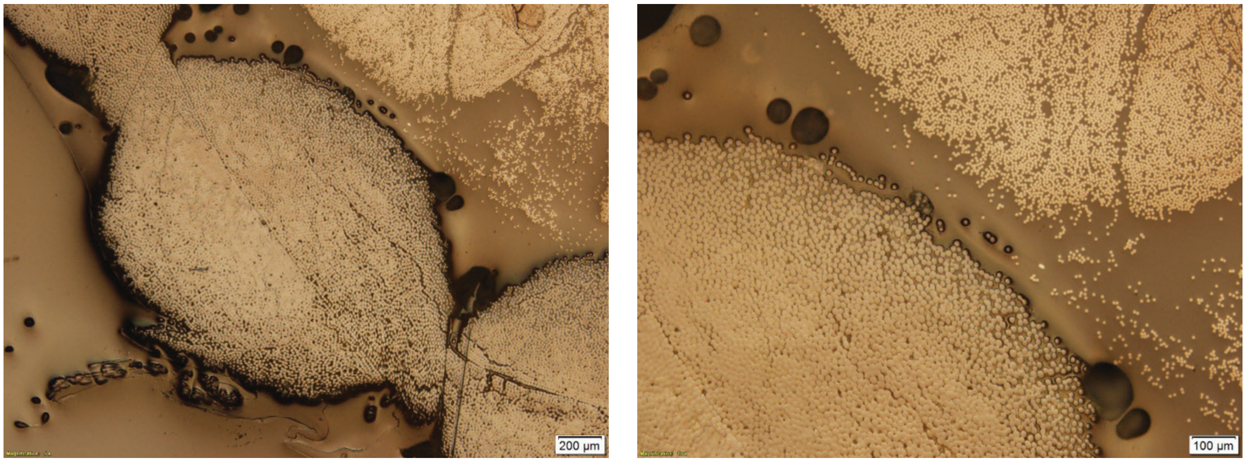

(a) (b)

Figure C.9: Closeup of improved core-braid interface showing resin making up the majority of the interface, with some relatively small voids still present in the structure

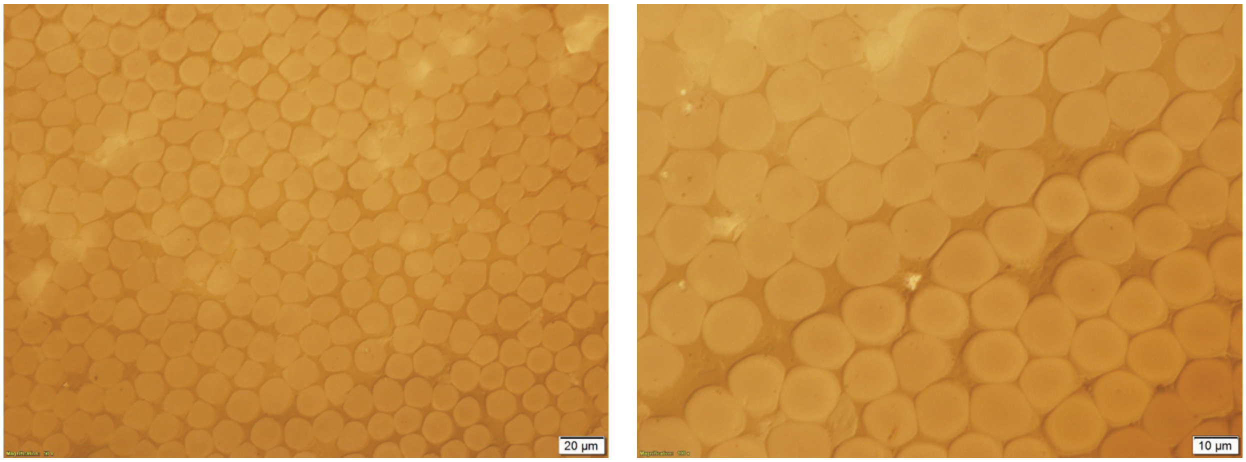

(a) (b)

Figure C.10: Representative microstructure of braid showing less dense fiber packing and improved impregnation with more complete fiber wetting

C.4.2 SEM analysis

SEM analysis was conducted on the rebar to further examine the microstructure of the braid. Figure C.11 compares the packing and fiber wetting inside the braid. Figure C.11(a) shows the braid produced by single impregnation. The structure shows tight fiber packing, causing deformation of the fibers, with no matrix material present between fibers. Figure C.11(b) shows the braid produced by dual impregnation. Here, matrix material is present between the majority of the fibers, and less fiber deformation is observed. While fibers are still tightly packed, the impregnation quality is much improved over the single impregnation method. These results are consistent with the optical microscopy observations.

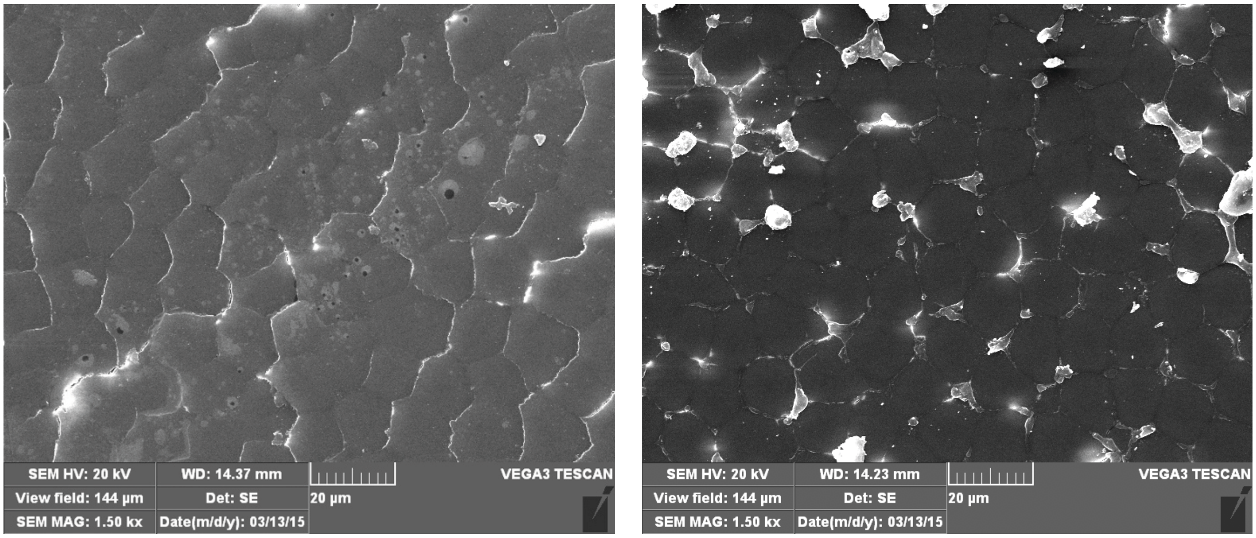

(a) (b)

Figure C.11: SEM images taken at 1500x magnification showing (a) tight packing of fibers in braid made using primary impregnation, (b) improved fiber wetting in braid made using dual impregnation

C.4.3 Burn-off Testing

Burn-off tests were conducted based on ASTM D3171 [3] on rebar specimens produced by single and dual impregnation methods. Five specimens of each type were tested to compare the change in fiber, matrix, and void volume fractions due to the change in impregnation methods. The average volume fractions and their standard deviations are summarized in Table C.1. It was found that the dual impregnation method resulted in a 22% increase in the matrix volume fraction, V_m, and a 42% decrease in the void volume fraction, V_v, while leaving the volume fraction of fibers, V_f, relatively constant. These results reflect the observations of the microstructural analysis showing that the dual impregnation method improved impregnation of the braid, and decreased the proportion of voids at the interface in favor of matrix material, while leaving the core microstructure the same.

Table C.1: Summary of burn-off test results

	V_f	V_m	V_v
Single Impregnation	0.425 ± 0.014	0.404 ± 0.013	0.171 ± 0.004
Dual Impregnation	0.408 ± 0.016	0.493 ± 0.024	0.099 ± 0.010

C.4.4 Pullout Testing

Pullout tests were conducted to determine interfacial shear strength between the core and braid structures. Five specimens produced by single impregnation, and six specimens produced by dual impregnation were tested. The average interfacial shear strengths (± standard deviations) are summarized in Table C.2. Dual impregnation increased the interfacial shear strength by over three times, indicating an improved bond between the core and braid structures. Figure C.12 shows representative images of the surface of the carbon core after pullout for both types of specimens. In these images, the light colored areas correspond to matrix material left on the surface after pullout. The rebar produced by dual impregnation had a significantly greater amount of matrix present on the surface of the core, indicating that more matrix material was present at the core/braid interface. This is consistent with the optical microscopy and burn-off test results.

Table C.2: Comparison of average interfacial shear strength at the core/braid interface for rebar produced using single and dual impregnation methods

	Single Impregnation	Dual Impregnation
Interfacial Shear Strength (MPa)	4.6 ± 2.0	14.6 ± 3.8

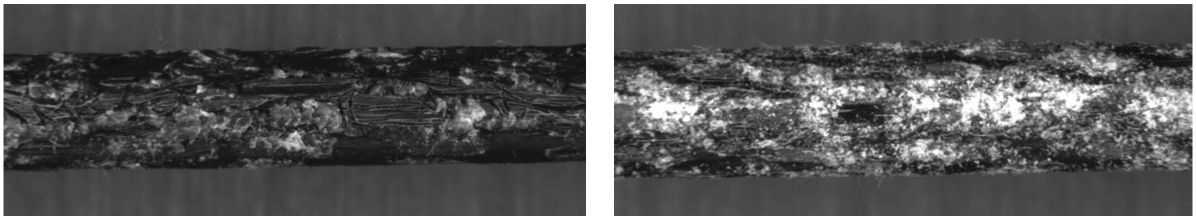

(a) (b)

Figure C.12: Comparison of core surface condition after pullout: (a) single impregnation, (b) dual impregnation

C.5 CONCLUSIONS

Single and dual impregnation methods were compared in a braidtrusion process for the production of FRP rebar. The dual impregnation method resulted in improved impregnation of the braid yarns while also filling the majority of the interfacial region with matrix, reducing the volume of voids in the structure and increasing the matrix volume fraction. Dual impregnation led to no significant changes in the core impregnation quality, and both single and dual impregnation methods produced a well-impregnated core. The improved interface of the dual impregnated samples led to higher interfacial shear strengths during pullout testing, and may be beneficial to the mechanical performance of the rebar by improving load transfer and reducing the possibility for delamination. Dual impregnation was clearly the more effective of the two processes and was therefore chosen for the dieless braidtrusion process used in this thesis.

C.6 REFERENCES

[1] Du, G., and Popper, P., 1994, "Analysis of a Circular Braiding Process for Complex Shapes," The Journal of the Textile Institute, **85**(3) pp. 316-337.

[2] Ko, F., Head, A., and Pastore, C., 1989, "Handbook of Industrial Braiding," Atkins and Pearce, Covington, Kentucky.

[3] ASTM International, 2011, "ASTM D3171 - 11 Standard Test Method for Constituent Content of Composite Materials," pp. 1-11.

APPENDIX D: PRELIMINARY SELECTION OF CURE SCHEDULE

D.1 INTRODUCTION

Preliminary characterization was conducted on the epoxy resin/hardener system used in this thesis in order to approximate a suitable cure schedule for the FRP rebar. Samples of the resin system were cured at various times and temperatures, and cure fractions were analyzed by differential scanning calorimetry (DSC) to determine degree of cure. Based on manufacturer data for a similar resin system [1], temperatures between 150 ˚C and 175 ˚C were recommended for a high degree of cure, however, the time required for curing is highly dependent on the geometry of the part. Hardness testing was conducted on the cured resin samples and was compared to the hardness of the rebar specimens produced using the selected cure schedule.

D.2 METHODS

D.2.1 Cured Epoxy Specimen Preparation

Nine epoxy samples were cured under different conditions, as outlined in Table D.1. These different cure schedules were used to determine a suitable curing schedule for the FRP rebar to allow for continuous production with a high degree of cure. Curing temperatures of 100 ˚C, 140 ˚C, and 180 ˚C were considered at times ranging from 6 to 40 minutes. Epoxy samples were cured in molds consisting of 3/8 inch diameter by 1 inch tall copper tubes with one side blocked by an aluminum plate and sealed with silicone caulking, as shown in Figure D.1(a). The molds were sprayed with silicone mold release agent, then filled with epoxy and placed in a preheated oven (Lindberg Blue M™ VO1218, Thermo Fisher Scientific, USA) for curing. An example of a resulting cured epoxy sample is shown in Figure D.1(b).

Table D.1: Curing parameters for epoxy test specimens

Temperature (˚C)	Time (min)
100	15
100	20
100	40
140	10
140	15
140	20
180	6
180	11
180	20

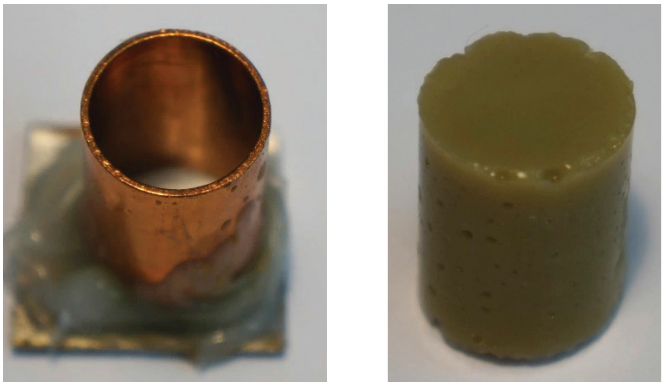

(a) (b)

Figure D.1: (a) Mold for curing resin specimen, (b) example of a cured resin specimen

D.2.2 DSC Testing

Samples were extracted from the cured epoxy specimens for DSC testing. To produce these samples, the cured resin specimens were drilled out in multiple locations using a drill bit cleaned with methanol. The shavings were collected and ground using a mortar and pestle to produce samples of approximately 100 mg. DSC tests for degree of cure, as described in Chapter 4, were conducted on the epoxy samples.

D.2.3 Microhardness testing

Vickers microhardness tests were conducted on the cured epoxy samples. Hardness of epoxy resins has been shown to change with degree of cure, and therefore, it can be used as a simple quality control measure to compare the cure of the FRP rebar to that of the cured epoxy specimens [2].

To prepare samples for hardness testing, the cured specimens were mounted in epoxy (ColdCure, Industrial Formulators Inc., USA) and ground and polished to produce a smooth, flat surface for analysis. Coarse grinding used 320 grit and 600 grit sandpaper, and polishing was performed using a 9 µm diamond suspension, followed by a 3 µm diamond suspension, and finally a 0.05 µm alumina slurry. An example of the resulting samples is shown in Figure D.2(a). A Vickers microhardness testing instrument (Wilson® VH3100, Buehler, USA) was used to measure hardness at 5 locations on each specimen using the test pattern shown schematically in Figure D.2(b). Indents were made using an applied load of 500 g and a dwell time of 14 seconds. Five rebar specimens were also tested for hardness. Specimens were cut from random locations along the rebar length and were mounted and polished as previously described. One hardness indent was measured for each specimen. Hardness indents were taken within the core of the rebar, in a resin-rich region of the microstructure, as shown in Figure D.3. Care was taken to ensure that only matrix material was indented and fibers were avoided.

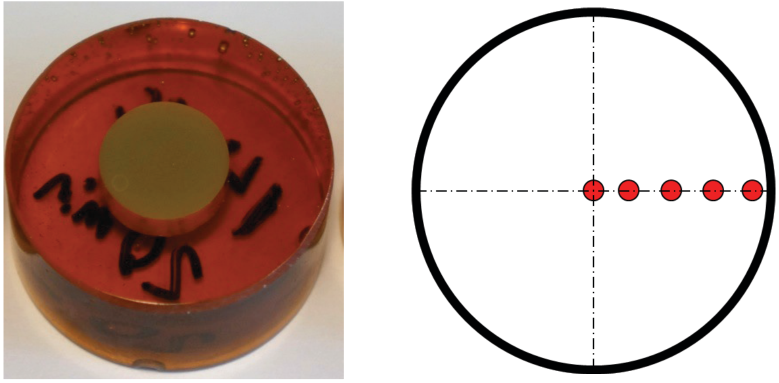

(a) (b)

Figure D.2: (a) Polished sample of cured resin specimen, (b) schematic of hardness test pattern, where red dots represent hardness measurement locations

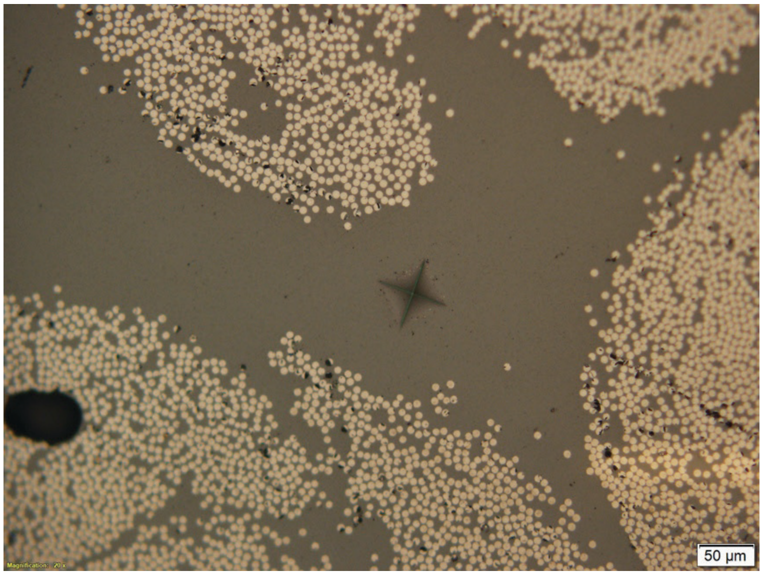

Figure D.3: Micrograph showing hardness indent in cured rebar specimen, taken in resin-rich region of core

D.3 RESULTS & DISCUSSION

D.3.1 Degree of Cure by DSC Testing

Figure D.4 shows a plot of degree of cure versus curing time for all three curing temperatures examined. DSC testing revealed that for all cure times tested, the specimens cured at 140 and 180 ˚C all showed very high degree of cure, between 98 and 100%. The 100 ˚C specimens revealed much lower degree of cure, and only achieved a maximum of 90% cure after 40 minutes in the oven. This showed that a cure temperature between 140 and 180˚C should be suitable for curing the FRP rebar, and that a high degree of cure can be achieved in less than 15 minutes at these temperatures. This was in relatively good agreement with the datasheet, which suggested a cure temperature between 150 and 175 ˚C for a high degree of cure.

Based on the results of these preliminary tests, a cure schedule of 160 ˚C for 16.2 minutes was used for the dieless braidtrusion process.

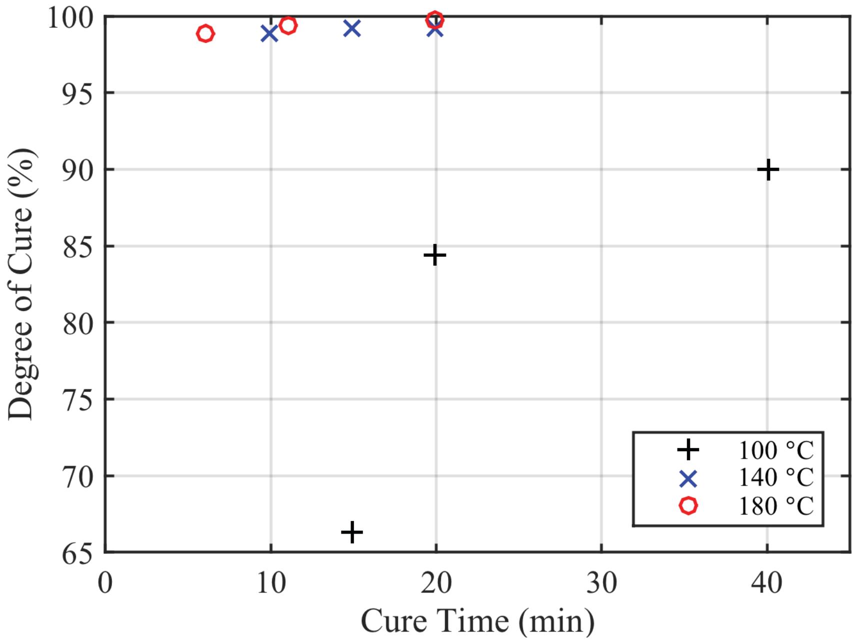

Figure D.4: Degree of cure measured by DSC for different cure schedules

D.3.2 Microhadness Testing

Microhardness tests were conducted on the cured epoxy specimens with high degrees of cure (>98%), and results are summarized in Table D.2. The highly cured specimens showed relatively consistent hardness values, with average hardness ranging from 18.0 to 18.7 HV 500gF. Standard deviations were low, indicating that the degree of cure was consistent from the inside to the outside of each sample cross-section.

Table D.3 shows the results of microhardness testing on the rebar samples, and revealed an average hardness of 18.3 ± 0.6 HV 500gF. This is consistent with the hardness values for the highly cured resin, which suggests that the curing schedule used for the FRP rebar was successful. Due to the nature of the curing process during dieless braidtrusion, the rebar was cured from the outside-in, and therefore, the center of the rebar was more likely to be under-cured than the outer regions. Since the hardness indents were all taken from the core of the rebar, this suggests that the entire cross section of the rebar was well cured, an the selected cure schedule of 160 ˚C for 16.2 minutes was suitable for producing highly cured FRP rebar.

Table D.2: Summary of hardness test results for highly cured resin specimens

Cure Temperature (˚C)	Cure Time (min)	Degree of Cure (%)	Vickers Hardness (HV 500 gF)
140	10	98.9%	18.5 ± 0.4
140	15	99.2%	18.0 ± 0.1
140	20	99.3%	18.4 ± 0.1
180	6	98.8%	18.7 ± 0.1
180	11	99.3%	18.5 ± 0.1
180	20	99.7%	18.4 ± 0.2

Table D.3: Summary of hardness test results for cured rebar specimens

Test Number	Vickers Hardness (HV 500 gF)
1	18.3
2	18.5
3	18.0
4	17.6
5	19.3
Average	**18.3**
Std Dev	**0.6**

D.4 CONCLUSIONS

The resin system used in this thesis was characterized by DSC and hardness testing to estimate an appropriate curing schedule for the production of FRP rebar by dieless braidtrusion. Results suggest that curing the rebar between 140 ˚C and 180 ˚C for at least 15 minutes should result in a high degree of cure, greater than 98%. Rebar was manufactured using a cure schedule of 160 ˚C for 16.2 minutes, and hardness testing was conducted for comparison to the results of the highly cured epoxy. The hardness of the matrix material in the core of the rebar was consistent with that of the highly cured epoxy, which suggests that the cure schedule used for dieless braidtrusion was successful in producing FRP rebar with a high degree of cure. This cure schedule was used for all rebar produced in this thesis.

D.5 REFERENCES

[1] Lindau Chemicals Inc., 2002, "Technical Data Sheet, Epoxy Resin System for Pultrusion: LS-81K Anhydride Curing Agent," pp. 1-6.

[2] Hoa, S.V., 2009, "Principles of the Manufacturing of Composite Materials,"DEStech Publications, pp. 45-98, Chap. 2.

APPENDIX E: IMAGE ANALYSIS CODE

E.1 INTRODUCTION

In this section, the MATLAB® code used for image analysis is provided, including measurement of fiber and matrix volume fractions in the rebar core and braid structures, as well as measurement of core, braid, interface, and shell area fractions of the rebar cross-section. When considering the area fractions, it should be noted that the image masks that are imported were pre-processed as described in Chapter 4. The directories used in the code to retrieve images and save data files and images are unique to these examples. The adaptive thresholding function [1] used in the segmentation of the braid constituents is also provided.

E.2 MATLAB CODE

E.2.1 Constituent volume fractions (core)

```
%% Initial setup, ask for image name and save file name
prompt = {'Enter filename for data'};
dlg_title = 'Setup';
num_lines = 1;
def = {'coreData.txt'};
answer = inputdlg(prompt,dlg_title,num_lines,def);
dataFile = char(answer(1));
%% Create .txt file and header based on input
cd Data
fileID = fopen(dataFile,'w');
t = (datetime('now'));
DateString = datestr(t);
fprintf(fileID,'%s\n','Marcus Ivey');
fprintf(fileID,'%s\n','Carbon');
fprintf(fileID,'%s\n',DateString);
fprintf(fileID,'%s\t%s\t%s\t%s\n','filename','Af','Am','At');
fclose(fileID);
cd ../
%% Make image save folder in Output folder
cd Output;
timestamp = datestr(t,'dd-mmm-yyyy HH;MM;SS');
foldername = sprintf('core %s',timestamp);
mkdir(foldername)
```

```
cd ../
%% Locate image folder and get image filenames
cd Core;
cd NR
imageName = dir('*.png');
cd ../
cd ../
%% Initial image import
% import image stack based on filename (eg. name01.jpg)
for i = 1:length(imageName)
    % import RGB image
    cd Core
    cd NR
    filename = imageName(i).name;
    RGB = imread(filename);
    cd ../
    cd ../
    %% image processing to segment fibers and matrix
    %crop image to get rid of scale bar, convert to grayscale, enhance
    %contrast, adaptive thresholding, clean up image
    % convert image to grayscale
    I = rgb2gray(RGB);
    rect = [0 0 1600 1100];
    I = imcrop(I,rect);
    I = imadjust(I);
    level = graythresh(I);
    bw = im2bw(I,level);
    bw = imcomplement(bw);
    bw = bwareaopen(bw,20);
    bw = imcomplement(bw);
    se = strel('disk',2);
    bw = imopen(bw,se);
    %% Calculate volume fractions
    fiber = bw;
    matrix = ~bw;
    Area.fiber = bwarea(fiber);
    Area.matrix = bwarea(matrix);
    Area.total = Area.fiber + Area.matrix;
```

```
    A.t = Area.total / Area.total;
    A.f = Area.fiber / Area.total;
    A.m = Area.matrix / Area.total;
    A = [A.f, A.m, A.t];
    %% Display fiber and matrix regions
    figure
    % show grayscale image
    imshow(I)
    red = cat(3, ones(size(I)),zeros(size(I)),zeros(size(I)));
    green = cat(3, zeros(size(I)),ones(size(I)),zeros(size(I)));
    hold on
    % add highlighted areas on top of grayscale image
    highlight1 = imshow(red);
    highlight2 = imshow(green);
    hold off
    % set the effective area for each highlighted region
    set(highlight1, 'AlphaData', matrix);
    set(highlight2, 'AlphaData', fiber);
    %% Save figure to image file
    % set image filename
    name = sprintf('%s','highlight all',filename);
    cd Output
    cd (foldername)
    % save as image or matlab figure
    saveas(gcf,name,'png')
    cd ../
    cd ../
    % close current figure
    close
    %% Save data to .txt file
    % opens data file created at the start and appends area fractions
    cd Data
    fileID = fopen(dataFile,'a');
    fprintf(fileID,'%s\t',name);
    fprintf(fileID,'%1.4f\t%1.4f\t%1.4f\n',A);
    fclose(fileID);
    cd ../
end
```

E.2.2 Constituent volume fractions (braid)

```
%% Initial setup, ask for image name and save file name
prompt = {'Enter filename for data'};
dlg_title = 'Setup';
num_lines = 1;
def = {'braidData.txt'};
answer = inputdlg(prompt,dlg_title,num_lines,def);
dataFile = char(answer(1));
%% Create .txt file and header based on input
cd Data
fileID = fopen(dataFile,'w');
t = (datetime('now'));
DateString = datestr(t);
fprintf(fileID,'%s\n','Marcus Ivey');
fprintf(fileID,'%s\n','Braid');
fprintf(fileID,'%s\n',DateString);
fprintf(fileID,'%s\t%s\t%s\t%s\n','filename','Af','Am','At');
fclose(fileID);
cd ../
%% Make image save folder in Output folder
cd Output;
timestamp = datestr(t,'dd-mmm-yyyy HH;MM;SS');
foldername = sprintf('braid %s',timestamp);
mkdir(foldername)
cd ../

cd May12Images
cd Braid
cd Originals
imageName = dir('*.png');
cd ../
cd ../
cd ../
for i = 1:length(imageName)
    % import RGB image
    cd May12Images
    cd Braid
    cd Originals
    filename = imageName(i).name;
```

```
I = imread(filename);
cd ../
cd ../
cd ../
%% image processing to segment fibers and matrix
%crop image to get rid of scale bar, convert to grayscale, enhance
%contrast, adaptive thresholding, clean up image
rect = [0 0 1600 1100];
I = imcrop(I,rect);
I = rgb2gray(I);
I = imadjust(I);
bw = adaptivethreshold(I,500,0.001,0);
bw = imcomplement(bw);
bw = bwareaopen(bw,10);
%% Calculate volume fractions
fiber = ~bw;
matrix = bw;

Area.fiber = bwarea(fiber);
Area.matrix = bwarea(matrix);
Area.total = Area.fiber + Area.matrix;

A.t = Area.total / Area.total;
A.f = Area.fiber / Area.total;
A.m = Area.matrix / Area.total;

A = [A.f, A.m, A.t];
%%
figure
% show grayscale image
imshow(I)
red = cat(3, ones(size(I)),zeros(size(I)),zeros(size(I)));
green = cat(3, zeros(size(I)),ones(size(I)),zeros(size(I)));
hold on
% add highlighted areas on top of grayscale image
highlight1 = imshow(red);
highlight2 = imshow(green);
hold off
```

```
    % set the effective area for each highlighted region
    set(highlight1, 'AlphaData', matrix);
    set(highlight2, 'AlphaData', fiber);
    %% Save figure to image file
    % set image filename
    name = sprintf('%s','highlight all',filename);
    cd Output
    cd (foldername)
    % save as image or matlab figure
    saveas(gcf,name,'png')
    cd ../
    cd ../
    % close current figure
    close
    %% Save data to .txt file
    % opens data file created at the start and appends area fractions
    cd Data
    fileID = fopen(dataFile,'a');
    fprintf(fileID,'%s\t',name);
    fprintf(fileID,'%1.4f\t%1.4f\t%1.4f\n',A);
    fclose(fileID);
    cd ../
end
```

E.2.3 Rebar area fractions

```
%% Initial setup, ask for image name and save file name
prompt = {'Enter filename for data'};
dlg_title = 'Setup';
num_lines = 1;
def = {'areaFractionData.txt'};
answer = inputdlg(prompt,dlg_title,num_lines,def);
dataFile = char(answer(1));
%% Create .txt file and header based on input
cd Data
fileID = fopen(dataFile,'w');
t = (datetime('now'));
DateString = datestr(t);
fprintf(fileID,'%s\n','Marcus Ivey');
fprintf(fileID,'%s\n','Rebar');
```

```
fprintf(fileID,'%s\n',DateString);
fprintf(fileID,'%s\t%s\t%s\t%s\t%s\t%s\t', ...
    'filename','Ab','Ac','Ai','As','At');
fprintf(fileID,'%s\t%s\t%s\t%s\t%s\n', ...
    'Braid Area','Core Area','Interface Area','Shell Area','Total Area');
fclose(fileID);
cd ../
%% Make image save folder in Output folder
cd Output;
timestamp = datestr(t,'dd-mmm-yyyy HH;MM;SS');
foldername = sprintf('rebar %s',timestamp);
mkdir(foldername)
cd ../
%% Locate image folder and get image filenames
cd Rebar;
cd NRImpregArea;
cd Originals;
imageName = dir('*.jpg');
cd ../
cd ../
cd ../
%% Process image stack
% import image stack based on filename (eg. name01.jpg)
for i = 1:length(imageName)
   %% Read in original image and convert to grayscale
    cd Rebar
    cd NRImpregArea
    cd Originals
    filename = imageName(i).name;
    I.tot = imread(filename);
    I.tot = rgb2gray(I.tot);
    cd ../
    cd ../
    cd ../
    %% Import braid mask & determine pixel area
    cd Rebar
    cd NRImpregArea
    cd BraidMasks2
    I.braid = imread(filename);
```

```
cd ../
cd ../
cd ../
I.braid = im2bw(I.braid,.9999);
I.braid = bwareaopen(I.braid,1000);
fill.braid = ~I.braid;
fill.total = imfill(fill.braid,'holes');
%% Import core mask & determine pixel area
cd Rebar
cd NRImpregArea
cd CoreMasks2
I.core = imread(filename);
cd ../
cd ../
cd ../
I.core = im2bw(I.core,0);
fill.core = ~I.core;
%% Import shell mask & determine pixel area
cd Rebar
cd NRImpregArea
cd ShellMasks
I.shell = imread(filename);
cd ../
cd ../
cd ../
I.shell = im2bw(I.shell,0);
fill.outer = ~I.shell;
%% Calculate interface, and shell areas
fill.interface = fill.total - fill.core - fill.braid;
fill.shell = fill.outer - fill.total;
%% Highlight core, braid, and interface areas
figure; imshow(I.tot); hold on
braid = cat(3,ones(size(I.tot)),ones(size(I.tot)),zeros(size(I.tot)));
core = cat(3,zeros(size(I.tot)),ones(size(I.tot)),zeros(size(I.tot)));
int = cat(3,ones(size(I.tot)),zeros(size(I.tot)),zeros(size(I.tot)));
shell = cat(3,ones(size(I.tot)),zeros(size(I.tot)),zeros(size(I.tot)));
Br = imshow(braid);
Co = imshow(core);
Int = imshow(int);
```

```
Sh = imshow(shell);
set(Br, 'AlphaData', fill.braid);
set(Co, 'AlphaData', fill.core);
set(Int, 'AlphaData', fill.interface);
set(Sh, 'AlphaData', fill.shell);
B = bwboundaries(fill.braid);
C = bwboundaries(fill.core);
S = bwboundaries(fill.outer);
for k = 1 : length(B)
    b = B{k};
    plot(b(:,2),b(:,1),'k','linewidth',2);
end
for k = 1 : length(C)
    c = C{k};
    plot(c(:,2),c(:,1),'k','linewidth',2);
end
for k = 1 : length(S)
    s = S{k};
    plot(s(:,2),s(:,1),'k','linewidth',2);
end

%% Save figure to image file
% set image filename
name = sprintf('%s','highlights',filename);
cd Output
cd (foldername)
% save as image or matlab figure
saveas(gcf,name,'png')
cd ../
cd ../
% close current figure
close
%% Calculate area and area fractions for each region
% pixel area of each region
A.total = bwarea(fill.outer);
A.braid = bwarea(fill.braid);
A.core = bwarea(fill.core);
A.interface = bwarea(fill.interface);
A.shell = bwarea(fill.shell);
```

```
    pxArea = [A.braid, A.core, A.interface, A.shell, A.total];
    % convert to area in microns
    calibrationFactor = 568;
    umArea = pxArea / calibrationFactor^2;
    % calculate area fractions
    A.b = A.braid / A.total;
    A.c = A.core / A.total;
    A.i = A.interface / A.total;
    A.s = A.shell / A.total;
    A.t = A.b + A.c + A.s + A.i;
    AreaFrac = [A.b, A.c, A.i, A.s, A.t];
  %% Save data to .txt file
    % opens data file created at the start and appends area fractions
    cd Data
    fileID = fopen(dataFile,'a');
    fprintf(fileID,'%s\t',filename);
    fprintf(fileID,'%1.4f\t%1.4f\t%1.4f\t%1.4f\t%1.4f\t',AreaFrac);
    fprintf(fileID,'%1.4f\t%1.4f\t%1.4f\t%1.4f\t%1.4f\n',umArea);
    fclose(fileID);
    cd ../

end
```

E.2.4 Adaptive thresholding function

```
function bw=adaptivethreshold(IM,ws,C,tm)
%ADAPTIVETHRESHOLD An adaptive thresholding algorithm that seperates the
%foreground from the background with nonuniform illumination.
%  bw=adaptivethreshold(IM,ws,C) outputs a binary image bw with the local
%   threshold mean-C or median-C to the image IM.
%  ws is the local window size.
%  tm is 0 or 1, a switch between mean and median. tm=0 mean(default); tm=1
median.
%
%  Contributed by Guanglei Xiong (xgl99@mails.tsinghua.edu.cn)
%  at Tsinghua University, Beijing, China.
%
%  For more information, please see
%  http://homepages.inf.ed.ac.uk/rbf/HIPR2/adpthrsh.htm
```

```
if (nargin<3)
    error('You must provide the image IM, the window size ws, and C.');
elseif (nargin==3)
    tm=0;
elseif (tm~=0 && tm~=1)
    error('tm must be 0 or 1.');
end

IM=mat2gray(IM);

if tm==0
    mIM=imfilter(IM,fspecial('average',ws),'replicate');
else
    mIM=medfilt2(IM,[ws ws]);
end
sIM=mIM-IM-C;
bw=im2bw(sIM,0);
bw=imcomplement(bw);
```

E.3 REFERENCES

[1] Xiong, G., 2006, "Local Adaptive Thresholding".

APPENDIX F: FRP REBAR ANALYTICAL MODEL

F.1 INTRODUCTION

In this section, the MATLAB® code used for analytical model calculations is presented. The main script containing both the original and spring models detailed in Chapter 5 are shown, along with the custom functions used. The code includes definition of material and geometric properties, model calculations, and plotting of the final stress-strain results.

F.2 MATLAB CODE

F.2.1 Original model and spring model calculations (script)

```
%% Modeling of pseudoductile FRP rebar tensile properties
%Units: modulus(MPa), stress(MPa), strain(mm/mm), area(mm2), load(N)
%% Measured braid angles
angle.braidpos = 20.7;
angle.braidneg = -angle.braidpos;
angle.core = 0;
%% Material properties
% Carbon fiber properties
core.Ef = 281400;
core.vf = 0.36;
core.Gf = core.Ef/(2*(1+core.vf));
core.df = 8;
core.Vf = 0.465;
core.Sf = 2780;
core.ef = 0.0099;
% Kevlar fiber properties
braid.Ef = 112400;
braid.vf = 0.36;
braid.Gf = braid.Ef/(2*(1+braid.vf));
braid.df = 15;
braid.Vf = 0.711;
braid.Sf = 3000;
braid.ef = 0.024;
% Matrix properties
matrix.Em = 2730;
matrix.vm = 0.35;
matrix.Gm = matrix.Em/(2*(1+matrix.vm));
```

```
matrix.Sm = 73.8;
matrix.em = 0.05;
%% Rebar Geometrical Sizing
% Input Parameters
braid.Nc = 18;
core.Nc = 12;
braid.denier = 7100;
core.denier = 6930;
braid.density = 1.44;
core.density = 1.78;

%% Calculate total core, braid, total area and area fractions
[ A.c, A.b, Area.c, Area.b, Area.tot ] = rebarAreaFractions( braid.Nc,...
    core.Nc,angle.braidpos,angle.core,core.Vf,braid.Vf,core.denier,...
    braid.denier, core.density, braid.density );
%% Calculate lamina properties using Halpin-Tsai micromechanics equations
[core.E1,core.E2,core.G12,core.G23,core.v12,core.v21,core.v23] = ...
    HalpinTsai(core.Ef,core.vf,core.Gf,core.df,matrix.Em,matrix.vm,...
    matrix.Gm,core.Vf);
[braid.E1,braid.E2,braid.G12,braid.G23,braid.v12,braid.v21,braid.v23] = ...
    HalpinTsai(braid.Ef,braid.vf,braid.Gf,braid.df,matrix.Em,matrix.vm,...
    matrix.Gm,braid.Vf);
%% Calculate C matrix for core and braid
C.c = globalStiffness( core.E1,core.E2,core.G12,core.G23,core.v12,...
    core.v21,core.v23,angle.core);
C.bpos = globalStiffness( braid.E1,braid.E2,braid.G12,braid.G23,...
    braid.v12,braid.v21,braid.v23,angle.braidpos);
C.bneg = globalStiffness( braid.E1,braid.E2,braid.G12,braid.G23,...
    braid.v12,braid.v21,braid.v23,angle.braidneg);
%% Calculate C matrix, S matrix, and longitudinal elastic modulus
[ Ex.comp1, Ex.comp2, Ex.comp3 ] = ...
    rebarModulusPrediction( A.c, A.b, C.c, C.bpos, C.bneg );
%% Original Model
% Calculate yield, drop, and ultimate stress, strain, and load
epsilon.y = core.ef;
epsilon.u = braid.ef;
sigma.y = Ex.comp1*epsilon.y;
sigma.d = Ex.comp2*epsilon.y;
sigma.u = Ex.comp2*epsilon.u;
```

```
load.y = sigma.y*Area.tot;
load.d = sigma.d*Area.tot;
load.ult = sigma.u*Area.tot;
%% Spring Model
% Calculate yield, drop, and ultimate stress, strain, and load
epsilon2.y = core.ef;
gageLength = 250;
disp2.y = epsilon2.y*gageLength;
load2.y = Ex.comp1*(Area.tot)*epsilon2.y;

load2.d = 0.5*load2.y;

L.b = (disp2.y/load2.d - gageLength/(Ex.comp1*(Area.tot)))/...
    (1/(Ex.comp3*Area.b)-1/(Ex.comp1*(Area.tot)));
L.c = gageLength-L.b;

disp2.byield = load2.d*L.b/(Ex.comp3*Area.b);
disp2.cyield = load2.d*L.c/(Ex.comp1*(Area.tot));
epsilon2.byield = disp2.byield/L.b;
epsilon2.cyield = disp2.cyield/L.c;

epsilon2.bult = braid.ef;
disp2.bult = epsilon2.bult*L.b;
load2.ult = disp2.bult*Ex.comp3*Area.b/L.b;
disp2.cult = load2.ult*L.c/(Ex.comp1*(Area.tot));
epsilon2.cult = disp2.cult/L.c;
disp2.ult = disp2.bult+disp2.cult;
epsilon2.ult = disp2.ult/gageLength;

sigma2.y = load2.y/(Area.tot);
sigma2.d = load2.d/(Area.tot);
sigma2.u = load2.ult/(Area.tot);

%% Plotting Results
% initialize plot
width = 5;
height = 3.5;
x = 0;
```

```
y = 0;
linewidth1 = 1.2;
linewidth2 = 1.2;
figure('units','inches','position',[x y width height])
hold on

%% Original Model Plot
stress.load = linspace(0,sigma.y,100);
strain.load = linspace(0,epsilon.y,100);
stress.yield = linspace(sigma.y,sigma.d,100);
strain.yield = linspace(epsilon.y,epsilon.y,100);
stress.reload = linspace(sigma.d,sigma.u,100);
strain.reload = linspace(epsilon.y,epsilon.u,100);

Model = plot(strain.load,stress.load,'--r',strain.yield,...
    stress.yield,'--r',strain.reload,stress.reload,'--r');
Model(1).LineWidth = linewidth2;
Model(2).LineWidth = linewidth2;
Model(3).LineWidth = linewidth2;
set(get(get(Model(2),'Annotation'),...
    'LegendInformation'),'IconDisplayStyle','off');
set(get(get(Model(3),'Annotation'),...
    'LegendInformation'),'IconDisplayStyle','off');

%% Spring Model Plot
stress2.load = linspace(0,sigma2.y,100);
strain2.load = linspace(0,epsilon2.y,100);
stress2.yield = linspace(sigma2.y,sigma2.d,100);
strain2.yield = linspace(epsilon2.y,epsilon2.y,100);
stress2.reload = linspace(sigma2.d,sigma2.u,100);
strain2.reload = linspace(epsilon2.y,epsilon2.ult,100);

Spring = plot(strain2.load,stress2.load,'--k',strain2.yield,...
    stress2.yield,'--k',strain2.reload,stress2.reload,'--k');
Spring(1).LineWidth = linewidth2;
Spring(2).LineWidth = linewidth2;
Spring(3).LineWidth = linewidth2;
set(get(get(Spring(2),'Annotation'),...
```

```
    'LegendInformation'),'IconDisplayStyle','off');
set(get(get(Spring(3),'Annotation'),...
    'LegendInformation'),'IconDisplayStyle','off');

%% Format Plot
legend(['Original' char(10) 'Model'],['Spring' char(10) 'Model'],...
    'Location','southeast');
xlabel('Strain (mm/mm)');
ylabel('Stress (MPa)');
xlim([0 0.026]);
ylim([0 900]);
grid on;
set(gca,'FontSize',12);
set(gca,'FontName','Times New Roman');
```

F.2.2 Core and braid area fractions (function)

```
function [ Ac, Ab, coreImpregArea, braidImpregArea, totalArea ] = ...
    rebarAreaFractions( braidNc,coreNc,braidAngleDeg,coreAngleDeg,...
    Vfc,Vfb,coreDenier,braidDenier,coreDensity,braidDensity )
% Using equations from Du & Popper to calculate geometry of braid
% Calculations based on assumption of fully jammed braid
% Inputs: number of yarns, angle, denier, density for core and braid
% Outputs: braid, core, and total areas and area fractions

% Define braid and core angles
braidAngle = degtorad(braidAngleDeg);
coreAngle = degtorad(coreAngleDeg);

% Adjust core denier to units of g/m
coreDenierReduced = coreDenier/9000;
braidDenierReduced = braidDenier/9000;

% Core area (fibers only and impregnated)
coreFiberArea = coreNc*coreDenierReduced/(coreDensity*cos(coreAngle));
coreImpregArea = coreFiberArea/Vfc;

% Braid area (fibers only and impregnated)
braidFiberArea = braidNc*braidDenierReduced/(braidDensity*cos(braidAngle));
```

```
braidImpregArea = braidFiberArea/Vfb;

% Calculate impregnated area fractions for core and braid
totalArea = coreImpregArea + braidImpregArea;
Ac = coreImpregArea / totalArea;
Ab = braidImpregArea / totalArea;

end
```

F.2.3 Halpin-Tsai calculations (function)

```
function [ E1,E2,G12,G23,v12,v21,v23 ] = ...
    HalpinTsai( Ef,vf,Gf,df,Em,vm,Gm,Vf )
% Halpin Tsai micromechanics calculations for composite elastic properties
% based on fiber and matrix properties
% Inputs: fiber and matrix material properties
% Outputs: composite elastic properties

% Define fiber length and matrix volume fraction
l = 1000000;
Vm = 1 - Vf;

% Halpin-Tsai equations
z1 = 2*l/df;
z2 = 2;
z12 = 1;

n1 = ((Ef/Em)-1)/((Ef/Em)+z1);
n2 = ((Ef/Em)-1)/((Ef/Em)+z2);
n12 = ((Gf/Gm)-1)/((Gf/Gm+z12));
n4 = (3-4*vm+Gm/Gf)/(4*(1-vm));

E1 = Em*(1+z1*n1*Vf)/(1-n1*Vf);
E2 = Em*(1+z2*n2*Vf)/(1-n2*Vf);
G12 = Gm*(1+z12*n12*Vf)/(1-n12*Vf);
v12 = vf*Vf+vm*Vm;
v21 = v12*E2/E1;
G23 = Gm*(Vf+n4*Vm)/(n4*Vm+Vf*Gm/Gf);
v23 = (E2/(2*G23))-1;
```

```
end
```

F.2.4 Global stiffness and compliance calculations (function)

```
function [ C ] = globalStiffness( E1,E2,G12,G23,v12,v21,v23,angleDeg )
% Calculations of stiffness and compliance matrices based on fiber angle
% Inputs: composite elastic properties, braid angle
% Outputs: global compliance matrix

% Braid angle
angle = degtorad(angleDeg);

% Local compliance matrix
S = [1/E1 -v12/E1 -v12/E1 0 0 0; ...
    -v21/E2 1/E2 -v23/E2 0 0 0; ...
    -v21/E2 -v23/E2 1/E2 0 0 0; ...
    0 0 0 1/G23 0 0; ...
    0 0 0 0 1/G12 0; ...
    0 0 0 0 0 1/G12];

% Transformation matrix
T = [cos(angle)^2 sin(angle)^2 0 0 0 2*cos(angle)*sin(angle); ...
    sin(angle)^2 cos(angle)^2 0 0 0 -2*cos(angle)*sin(angle); ...
    0 0 1 0 0 0; ...
    0 0 0 cos(angle) -sin(angle) 0;
    0 0 0 sin(angle) cos(angle) 0;
    -cos(angle)*sin(angle) cos(angle)*sin(angle) 0 0 0 ...
    cos(angle)^2-sin(angle)^2];

% Global compliance matrix
S = transpose(T)*S*T;

% Global stiffness matrix
C = inv(S);

end
```

F.2.5 Volume average stiffness and elastic modulus (function)

```
function [ Excomp1, Excomp2, Excomp3 ] = ...
    rebarModulusPrediction( Ac, Ab, Cc, Cbpos, Cbneg )
% Volume average stiffness method for composite stiffness and compliance
% Calculation of elastic modulus before and after yield
% Inputs: core and braid area fractions, stiffness matrices
% Outputs: longitudinal elastic modulus values

% Calculate stiffness matrix, compliance matrix, and longitudinal
%elastic modulus for composite rebar before yield
Ccomp1 = Ac*Cc + (Ab/2)*Cbpos + (Ab/2)*Cbneg;
Scomp1 = inv(Ccomp1);
Excomp1 = 1/Scomp1(1,1);

% Calculate stiffness matrix, compliance matrix, and longitudinal
%elastic modulus for composite rebar after yield
Ccomp2 = 0*Cc + (Ab/2)*Cbpos + (Ab/2)*Cbneg;
Scomp2 = inv(Ccomp2);
Excomp2 = 1/Scomp2(1,1);

% Calculate stiffness matrix, compliance matrix, and longitudinal
%elastic modulus for braid only (for spring model)
Ccomp3 = 0*Cc + (0.5)*Cbpos + (0.5)*Cbneg;
Scomp3 = inv(Ccomp3);
Excomp3 = 1/Scomp3(1,1);

end
```